

DOCTORAL THESIS

Developing Guided Wave Tomography for a Pipe Bend

Carlos Omar Rasgado Moreno

TALLINN UNIVERSITY OF TECHNOLOGY
DOCTORAL THESIS
18/2025

Developing Guided Wave Tomography for a Pipe Bend

CARLOS OMAR RASGADO MORENO



TALLINN UNIVERSITY OF TECHNOLOGY
School of Engineering
Department of Civil Engineering and Architecture

**The dissertation was accepted for the defence of the degree of Doctor of Philosophy
on 25 February 2025**

Supervisor: Dr. Madis Ratassepp,
Department of Civil Engineering and Architecture, School of Engineering,
Tallinn University of Technology
Tallinn, Estonia

Opponents: Dr. Bastien Chapuis,
Department of Digital Instrumentation,
Le Commissariat à l'énergie atomique et aux énergies alternatives
Gif-sur-Yvette, France

Dr. Renaldas Raisutis,
Ultrasound Research Institute,
University of Technology, Kaunas,
Kaunas, Lithuania

Defence of the thesis: 15 April 2025, Tallinn

Declaration:

Hereby I declare that this doctoral thesis, my original investigation and achievement, submitted for the doctoral degree at Tallinn University of Technology, has not been submitted for any academic degree elsewhere.

Carlos Omar Rasgado Moreno

signature

Copyright: Carlos Omar Rasgado Moreno, 2025
ISSN 2585-6898 (publication)
ISBN 978-9916-80-271-7 (publication)
ISSN 2585-6901 (PDF)
ISBN 978-9916-80-272-4 (PDF)
DOI <https://doi.org/10.23658/taltech.18/2025>
Printed by Koopia Niini & Rauam

Rasgado Moreno, C. O. (2025). *Developing Guided Wave Tomography for a Pipe Bend* [TalTech Press]. <https://doi.org/10.23658/taltech.18/2025>

TALLINNA TEHNIKAÜLIKOOL
DOKTORITÖÖ
18/2025

Ultrahelitomograafia toru põlvede kontrollimiseks

CARLOS OMAR RASGADO MORENO



Contents

Contents	5
List of publications	7
Authors Contribution to the Publications	8
Introduction	9
Scope and Objectives.....	9
Challenges	10
Hypothesis	11
Abbreviations.....	12
Symbols.....	13
1 Background	14
1.1 Motivation	14
1.2 Non-destructive testing for pipeline inspection	14
1.3 Guided wave tomography for pipeline inspection	14
1.4 Guided wave tomography for pipe bends.....	15
2 Theory	17
2.1 Acoustic forward model for guided wave propagation in a pipe bend	17
2.1.1 Orthogonal parametrization	17
2.1.2 Acoustic wave equation	18
2.1.3 Implementation for a pipe bend.....	20
2.2 Full-waveform inversion	20
3 Methods	22
3.1 Pipe Bend Specimen	22
3.2 Numerical Methods.....	22
3.2.1 FE Modeling	22
3.2.2 Acoustic Modeling.....	23
3.2.3 Hann-Shaped Defect	24
3.3 Data and Experimental Preconditioning	24
3.3.1 Chirp Excitation.....	24
3.3.2 Helical Path Separation.....	26
3.3.3 Shortest Path Using the Geodesic Equations.....	27
3.3.4 Autocalibration	28
3.4 Instrumentation	30
3.4.1 Measurements of Guided Waves.....	30
3.4.2 Impedance Measurements	30
4 Experiments and Results	33
4.1 Acoustic Forward Modeling for a Pipe Bend	33
4.1.1 Guided Wave Propagation	33
4.1.2 Helical Path Separation for a Pipe Bend.....	34
4.2 Guided Wave Tomography Based on Full Waveform Inversion for a Pipe Bend	36
4.2.1 Numerical Study.....	36

4.2.2	Experimental Validation	37
5	Discussion and Concluding Remarks	41
5.1	Summary of results	41
5.2	Key Conclusions Presented for Defense	42
5.3	Perspectives of Future Work.....	43
	List of Figures	45
	List of Tables	46
	References	47
	Acknowledgements	53
	Abstract.....	54
	Kokkuvõte	55
	Appendix 1	57
	Appendix 2	73
	Appendix 3	89
	Appendix 4	101
	Curriculum Vitae	111
	Elulookirjeldus.....	113

List of publications

Publications in Academic Journals

- I. Carlos-Omar Rasgado-Moreno, Marek Rist, Raul Land, and Madis Ratassepp. Acoustic Forward Model for Guided Wave Propagation and Scattering in a Pipe Bend. *Sensors*, 22(2):486, January 2022.
- II. Carlos-Omar Rasgado-Moreno and Madis Ratassepp. Geodesic equations for guided wave helical path separation for a pipe bend. *Mechanical Systems and Signal Processing*, 204:110820, December 2023.
- III. Carlos-Omar Rasgado-Moreno, Marek Rist, Raul Land, and Madis Ratassepp. Guided wave tomography of pipe bends based on full waveform inversion. *Ultrasonics*, 148:107560, April 2025.
- IV. Carlos-Omar Rasgado-Moreno, Panpan Xu, Marek Rist, and Madis Ratassepp. Optimising full waveform inversion with inhomogeneous transducers: Parameters and considerations for successful implementation. *NDT & E International*, 149:103265, January 2025.

Publications in Conference Proceedings

- V. Carlos Omar Rasgado Moreno and Madis Ratassepp. Quantitative Imaging of Elongated Thickness Defects in Pipelines Using Ultrasonic Guided Wave Tomography. *American Society of Mechanical Engineers Digital Collection*, February 2024.
- VI. Denys Iablonskyi, Carlos-Omar Rasgado-Moreno, Madis Ratassepp, Arto Klami, Edward Hæggström, and Ari Salmi. Unsupervised Fouling Reconstruction in the Pipe Bend. In *2023 IEEE International Ultrasonics Symposium (IUS)*, pages 1–3, September 2023. ISSN: 1948-5727 .

Authors Contribution to the Publications

The authors of this thesis contributed to all the listed publications by:

- I. conceptualizing the study in cooperation with all the co-authors; developing the acoustic forward modeling; processing the data; conducting numerical analysis and experimental validation of the results; drafting the manuscript.
- II. conceptualizing the study; developing the algorithm for the geodesic equations; processing the data; conducting numerical analysis and experimental validation of the results; drafting the manuscript.
- III. conceptualizing the study; developing the acoustic forward modeling for full wave-form inversion; processing the data; conducting numerical analysis and experimental validation of the results; manufacturing of the defect; drafting the manuscript.
- IV. conceptualizing the study in cooperation with the second co-author; developing the calibration method; processing the data; conducting numerical analysis and experimental validation of the results; manufacturing of the defect; drafting the manuscript in cooperation with the second co-author.
- V. conceptualizing the study; developing the algorithm for long defects; processing the data; conducting numerical analysis and experimental validation of the results; drafting the manuscript.
- VI. developing the algorithm for the geodesic equations; processing the data; conducting experimental validation of the results.

Introduction

Pipeline systems, particularly pipe bends, are subjected to a variety of stressors that can lead to significant damage over time. The unique challenges faced by pipe bends stem from the abrupt changes in fluid direction, which can induce stress and make these components vulnerable to fatigue, corrosion, and cracking [1].

Fatigue is a phenomenon that results from repeated stress cycles. This repetitive stress can lead to the formation of microscopic cracks within the pipe material. Over time, these cracks can grow, potentially leading to pipe failure. This is especially concerning for pipe bends, which are subjected to higher stress levels due to the changes in fluid direction [2].

Corrosion is another significant concern for pipe bends. This natural deterioration process occurs due to chemical reactions between the pipe material and the environment [3]. Corrosion can lead to thinning of the pipe walls, thereby reducing their capacity to withstand pressure. This is particularly problematic for pipe bends, as the increased stress levels can accelerate the corrosion process.

Cracking is a prevalent problem arising from factors like fatigue and corrosion [4]. These fractures often initiate in areas subjected to high stress, such as pipe bends, and can progressively worsen. If not promptly identified and managed, this deterioration can severely undermine the pipe's structural integrity, potentially causing catastrophic failures.

Addressing these issues necessitates the detection and surveillance of damage in pipeline elements, including bends. This is crucial for ensuring the pipeline's effectiveness, minimizing maintenance expenditures, prolonging its service life, and avoiding major failures [5]. Traditional surveillance methods typically involve targeted ultrasonic thickness measurements. Despite their effectiveness, these techniques can be labor-intensive and may not offer a holistic assessment of the pipe's condition.

Conversely, Guided Wave Tomography (GWT) utilizing Full Waveform Inversion (FWI) [6] is advantageous for detecting and evaluating damage within a specific region by analyzing waves emitted and received by an array of transducers. This technique enables a high-resolution reconstruction of the thickness of a steel pipe bend, offering a more comprehensive and efficient solution for monitoring.

Scope and Objectives

In this thesis, GWT based on FWI is implemented to reconstruct the remaining thickness of a pipe bend. Until now, the application of GWT based on FWI has been confined to simple structures such as plates and straight pipes, owing to their direct resemblance to the acoustic forward model required by the tomographic algorithm. The application of GWT to pipe bends presents a unique challenge due to the anisotropy of the acoustic wave field resulting from the bend curvature.

In **Publication I**, the elliptical anisotropy of the pipe bend is parameterized in terms of Thomsen parameters, providing a foundation for further analysis. Following this, **Publication II** delves into the signal processing required to enhance the resemblance between the measured data and the acoustically modeled data used by the inversion scheme. This work provides a robust methodology for data processing in the context of GWT. Subsequently, **Publication III** showcases a numerical analysis of FWI for a pipe bend and provides an experimental validation. The experimental validation was constrained by the inhomogeneous performance of the transducers, highlighting the need for improved transducer technology or methodologies to handle such inhomogeneities. Finally, **Publication IV** establishes guidelines to cope with the high inhomogeneity performance of the transducers

and demonstrates its successful integration with FWI. This work paves the way for more accurate and reliable thickness reconstruction in pipe bends using GWT based on FWI, potentially leading to significant improvements in pipeline monitoring and maintenance.

This thesis, therefore, represents a significant contribution to the field, extending the application of GWT based on FWI to more complex structures and addressing key challenges in the process. The findings and methodologies presented in this work have the potential to drive further research and development in this area, ultimately enhancing the safety and efficiency of pipeline systems.

The thesis encompasses the following objectives:

- To develop a two-dimensional (2-D) acoustic forward model to replace the complex three-dimensional (3-D) bend domain, using Thomsen parameters to model the elliptical anisotropy wavefield (**Publication I**).
- To remove the helical path trajectories from the 3-D bend domain based on the helical path separation algorithm and the geometric properties of the bend section (**Publication II**).
- To reduce experimental uncertainties and enhance data processing algorithms for the successful implementation of GWT (**Publications II and IV**).
- To implement GWT based on FWI to reconstruct the remaining wall thickness of a pipe bend (**Publication III**).
- To determine the advantages of GWT for pipe bends based on FWI over ray-tracing-based algorithms (**Publication III**).

Challenges

There are some challenges in the presented investigations that have been addressed:

1. The first significant step towards achieving full waveform inversion on a pipe bend involves the orthogonal parametrization of the pipe bend into a two-dimensional domain. This is primarily due to the preference for 2-D solvers over the computationally intensive 3-D solvers, owing to their simplicity.
2. Inherently, the wavefield on the pipe bend travels faster along the shortest bend's radius (intrados) as compared to the longest one (extrados). The equivalence with the bend domain is established through an artificial anisotropic formulation using Thomsen parameters.
3. The full-waveform inversion scheme implemented in this thesis resembles guided wave propagation on a plate with absorbing boundaries. Consequently, further helical paths in the pipe bend need to be extracted. Existing helical path separation algorithms require knowledge of the ray's traveled distance. As a result, the geodesic equations were implemented.
4. The guided wave-based instrumentation consisted of two rings of piezoelectric transducers, which exhibit inhomogeneous resonance frequencies. Therefore, a chirp function was utilized as the excitation signal to improve the signal-to-noise ratio, and a modified version of the auto-calibration method introduced by [7] was implemented to compensate for the transducer inhomogeneity.

Hypothesis

The application of GWT based on FWI can enable high-resolution reconstruction of the remaining thickness in pipe bends, overcoming the limitations of traditional ultrasonic thickness measurements. By parameterizing the elliptical anisotropy of the wavefield using Thomsen parameters and implementing advanced signal processing techniques, it is hypothesized that GWT based on FWI will provide a more accurate and comprehensive assessment of pipe bend integrity, ultimately improving damage detection, monitoring, and maintenance strategies for pipeline systems.

Abbreviations

2-D	Two-dimensional
3-D	Three-dimensional
FD	Finite difference
FE	Finite element
FFT	Fast Fourier Transform
FWI	Full waveform inversion
GW	Guided waves
GWT	Guided wave tomography
TOF	Time of flight
VTI	Vertical transverse isotropic

Symbols

α	Azimuth latitude
β	Azimuth longitude
θ	Group angle
ν	Poisson ratio
ε, δ	Thomsen parameters
ρ_e	Elliptically anisotropy parameter
ρ	Density
E_m	Young's modulus
$f(t)$	Particle plane position
H, H_0	Differential operators
Q	Calibration factor
R	Pipe bend radius
R_x	Receiver no.
R_c	Chirp response signal
R_d	Tone burst response signal
S	Geometric surface
S_c	Narrow band chirp source
S_d	Tone burst signal
T	Pipe's thickness
T_0	Pipe's nominal thickness
U	Three-dimensional wavefield
X, Y, Z	Three-dimensional coordinates
Ω	Two-dimensional space domain
ω	Angular frequency
$\bar{\theta}$	Angle of symmetry axis
ϕ	Phase angle
Σ	Three-dimensional space domain
k	Wave number
p	Pressure wavefield
q	Auxiliary wavefield
r	Central radius
t	Time
v	Phase velocity
v_v	Vertical velocity
x, y	Two-dimensional coordinates

1 Background in guided wave propagation in pipe bends and its integration with guided wave tomography

1.1 Motivation

Industrial pipelines serve an indispensable function in conveying volatile materials such as petrochemicals, steam, gas, and oil. Despite their critical importance, these pipelines are highly prone to deterioration caused by corrosion and erosion [2, 5]. Even minor operational flaws can precipitate catastrophic outcomes, as demonstrated by the explosion at the Pajaritos vinyl petrochemical facility in the Gulf of Mexico, which was instigated by a leak in a major pipeline [8]. Corrosion is often concentrated in areas like fittings, features, crossings, and particularly at bends, where abrupt changes in the fluid's direction and velocity lead to considerable thinning of the pipeline walls due to flow-accelerated corrosion [9, 10]. Erosion, on the other hand, occurs when particles within the flowing substance erode both the surface layers and the underlying metal. Hence, it is crucial to detect and evaluate damages in essential pipeline components to ensure their optimal functionality and avert catastrophic failures.

1.2 Non-destructive testing for pipeline inspection

Pipe bends are inspected using a variety of non-destructive testing methods, including in-pipe robots, radiography, and local thickness gauges. Local thickness gauges are portable ultrasound-based handheld devices that assess material thickness; nevertheless, they are slow to cover large areas [11]. Although radiography techniques, which use X-rays to penetrate structures, are sensitive, they also carry a danger of radiation exposure and need large equipment [12]. Although in-pipe robots provide effective curved pipeline inspection, they necessitate pipeline shutdowns for maintenance [13].

On the other hand, ultrasonic guided waves (GW) have been demonstrated to be useful for evaluating structural health [14–16]. These waves have great sensitivity for detecting corrosion and cracks in pipelines over long distances [17–19]. A single transducer array that is fixed to the pipe is usually used for pipeline screening. This arrangement enables continuous monitoring, damage detection, and estimation of the pipeline's remaining life [20–24]. Nevertheless, curvature poses difficulties for GW propagation in pipe elbows, a problem that has been well investigated by researchers [1, 25–29]. However, bend defect characterization remains a challenge for current screening techniques, impeding precise defect mapping and tracking of progression.

1.3 Guided wave tomography for pipeline inspection

One approach to address the limitations of conventional screening methods involves integrating them with tomographic techniques. In this method, instead of a single transducer ring, two transducer rings are fixed to the pipe, allowing for measurements from various angles, as illustrated in Figure 1(a). GWT operates by analyzing waveforms to construct a wall thickness map of a specific section. Any alterations in the waveforms are interpreted by tomographic algorithms as thickness reductions at particular locations [30].

The frequency-thickness product alters the phase and group velocities. This means that changing the thickness causes a predictable change in velocity while the frequency stays the same. Consequently, in the event that a reconstruction of velocity is generated, this can be transformed back into thickness. Based on the dispersion curves, any delay in the observed signals can then be associated with a thickness loss [30]. For an 8 mm thick steel plate, the dispersion curves of the fundamental Lamb wave modes are displayed

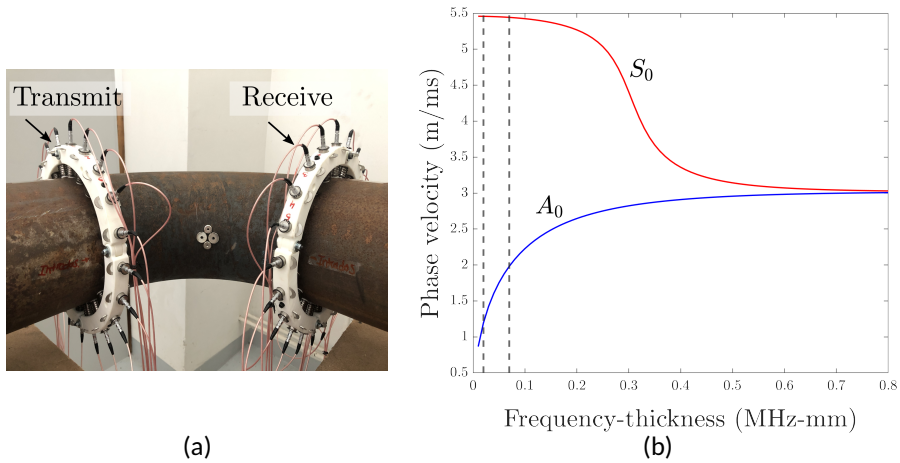


Figure 1: A guided wave tomography set-up (a), integrated by two rings of transducers, and dispersion curves of fundamental Lamb wave modes for an 8 mm steel plate (b) (from **Publication II**).

in Figure 1(b). The dashed lines in Figure 1(b) show a conventional frequency-thickness interval for GWT in the A_0 mode. In order to benefit from guided waves' dispersion characteristics, intervals with notable curve variations are often chosen for their heightened sensitivity to velocity changes.

To reconstruct flaws in GWT, one must solve an inverse problem by creating a synthetic dataset for a given structure and defect shape using a forward model. An accurate thickness reconstruction is obtained by iteratively refining the defect form by minimizing variances between synthetic and real data until convergence is reached. The GWT algorithm's flowchart, which highlights the importance of the forward model, is shown in Figure 2. As such, an accurate forward model that can describe guided wave propagation in the structure is critical to the correctness of the method [31].

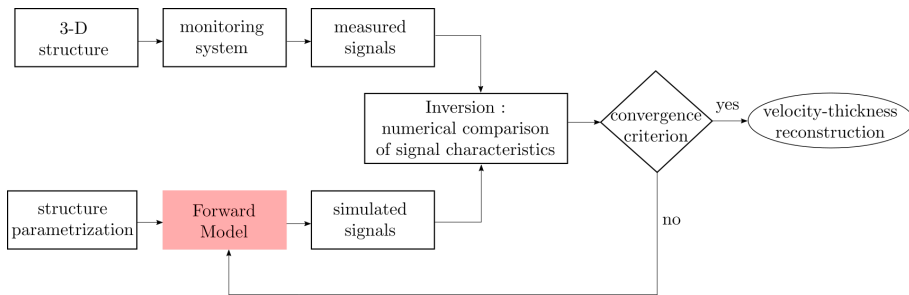


Figure 2: Flowchart of the GWT algorithm: real data (measured signals) and synthetic data (from forward model) are compared iteratively until a given residual criteria is reached. The role of the forward model is highlighted (from **Publication I**).

1.4 Guided wave tomography for pipe bends

The use of 2-D forward modeling over precise three-dimensional (3-D) elastic models has an extensive background in academia, triggered by benefits such as simplicity, lower computational load, congruity with algorithms founded on tomography, and the capacity to

evaluate the thickness of waveguides derived from velocity. GWT, has focused predominantly on basic geometric structures, like flat plates and straight pipes, as evidenced by considerable existing literature [6, 32–37]. Yet, the application of GWT to pipe bends is an area with limited research.

Contributions to this field include research by Volker and van Zon [38], where they developed a forward model exploiting recursive wavefield extrapolation on a deformed 2-D planar grid, aimed at travel-time tomography. Sanderson et al. [39] devised an analytical approach to model the guided wave propagation in bends, spotlighting the T(0,1) mode transmission in their study. Brath et al. [40] presented a 2-D rectangular forward model concentrating on GW propagation in bends, employing a method that preserves travel time via an orthogonal parametric bend representation. This model saw further expansion into curved ray tomography [41]. Wang and Li [42] introduced a sparse inversion technique with a similar GWT model to identify defects in bends.

Still, these methodologies are hampered by their reliance on time-of-flight (TOF) measurements to recreate the slowness distribution on a ray model. This approach overlooks diffraction effects and limits defect identification to those larger than the guided wave's wavelength. Particularly in pipe bends, rays tend to bypass the elbow bend due to a focusing effect [1, 25, 40], making the accuracy in defect detection highly contingent on the defect's circumferential position [43]. To mitigate this limitation, the idea of integrating additional transducers along the bend elbow was proposed [41], allowing for increased viewing angles, reducing the circumferential position dependency of the defect, albeit at the cost of additional transducers.

This thesis lays out a pioneering approach to surpass the drawbacks of travel-time tomography—full waveform inversion (FWI) tomography for corrosion mapping in pipe bends. FWI harnesses the complete wavefield data, cultivating more accurate inversion results over travel-time tomography [44]. This novel approach includes a specially designed acoustic forward model for pipe bends, making it FWI-compatible. The model is discretized by applying the finite difference (FD) method, with the bend domain's equivalence established through a fabricated anisotropic formulation using Thomsen parameters [45].

The introduction of this innovative acoustic forward model fitting for a pipe bend and compatible with FWI significantly increase the effectiveness of the method. Despite the complexities presented by the curvature of pipe bends, FWI exhibits promising potential in upholding the integrity and safety of industrial pipelines, which include bends.

2 Theory

2.1 Acoustic forward model for guided wave propagation in a pipe bend

Two-dimensional models are generally favored over their 3-D counterparts. This preference is largely due to their inherent simplicity and the ease with which they can be integrated with tomographic algorithms. However, accurately representing guided wave propagation in a pipe bend using a 2-D model presents a significant challenge: the wave propagation in a pipe bend becomes virtually anisotropic when observed in the 2-D domain.

This virtual anisotropy arises due to the geometry of the pipe bend. When a wave travels through the bend, the path it takes is not uniform. Compared to a plate or a straight pipe section, the ray paths in a pipe bend travel faster in the intrados (the inner curve) of the bend than in the extrados (the outer curve). This is because the azimuth length (the length along the curve of the bend) is shorter in the intrados compared to the extrados. To illustrate this concept, Figure 3 shows the contrast between the ray trajectories within a straight pipe section (a) and a pipe bend in a rectangular domain (b). Note that the ray trajectories in Figure 3(b) are bent due to the bend's curvature and, they are more dense at the edges of the domain. Therefore, even though the material properties do not change, the wave paths are affected by the geometry of the pipe bend, leading to a difference in wave speeds. This results in a virtual anisotropy in wave propagation.

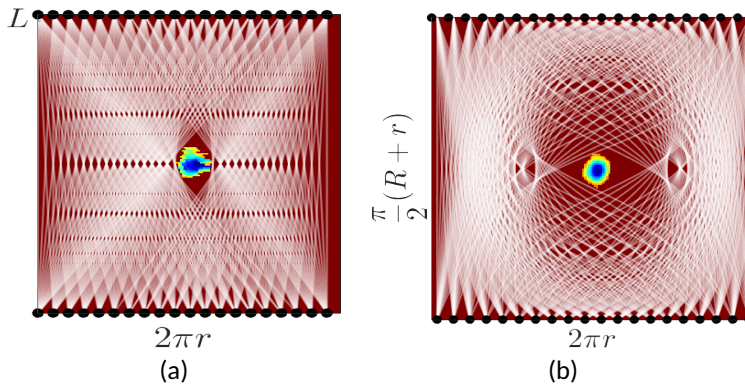


Figure 3: Ray paths traveling in a 2-D representation of a straight pipe (a) and a pipe bend (b) with an arbitrary defect (from **Publications III and IV**).

To address this issue, a 2-D acoustic forward model is introduced. This model takes into account the curvature of the bend and its consequential impact on the wavefield. The model simplifies the prediction of a synthetic wavefield for a pipe bend section. This synthetic wavefield is later integrated into the full waveform inversion algorithm. The integration facilitates the reconstruction of a detailed thickness map, thereby enhancing the overall accuracy and effectiveness of the process. Further details about the acoustic modeling and scattering analysis are given in **Publication I**.

2.1.1 Orthogonal parametrization

This thesis brings into focus a specific section of the torus, as depicted in Figure 4(a), existing within a 3-D space domain Σ . The torus is identified by its central radius r , the radius of its bend R , along with its latitudinal α and longitudinal β coordinates, relative to the Y -axis and the XY plane respectively. The objective is to model the anisotropic wave

propagation surrounding the torus. The section of this wave exists in a 2-D space domain Ω , showcased in Figure 4(b). To successfully model this, a shift of the torus section from the 3-D Σ to the 2-D Ω is mandatory.

The thesis employs the parameterization suggested by Brath et al. [40]. As per their methodology, the section of the torus is unfolded from the bend's longest radius path, situated at the extrados position $R + r$. Subsequently, the 2-D axes, both horizontal x and vertical y , are aligned with the torus's circumference $2\pi r$ and the bend's azimuth length $\beta(R + r)$ at the extrados respectively. This facilitates the expression of the 2-D Ω domain as $\Omega = [0, 2\pi r] \times [0, \beta(R + r)]$. Consequently, the extrados position is centrally located at the mid-circumference point $(\pi r, y)$. The opposing intrados position is bifurcated into two locations, one at the commencement of the circumference $(0, y)$, and the other at the conclusion $(2\pi r, y)$.

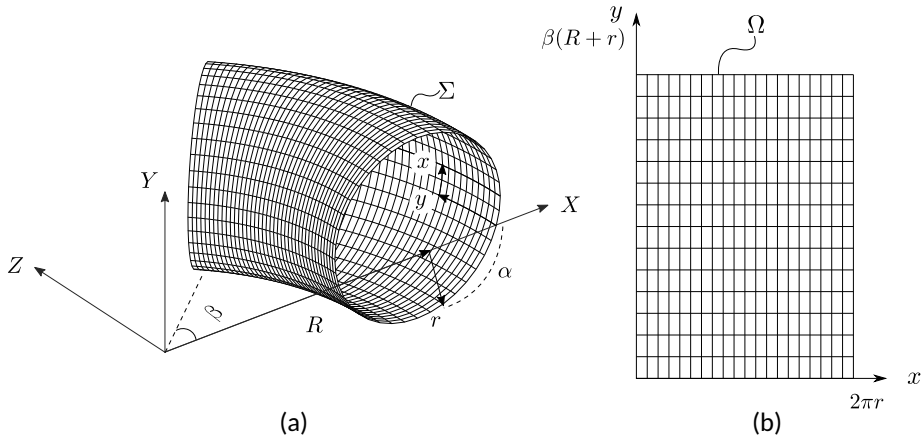


Figure 4: A torus section, representing the bend of the pipe, is translated from (a), the 3-D space domain Σ to (b), the 2-D space domain Ω (from **Publication I**).

Orthogonal parametrization of the torus is given by the set of equations:

$$\begin{aligned}
 X &= \left(R + r \cos \frac{x}{r}\right) \cos \frac{y}{R+r} \\
 Y &= r \sin \frac{x}{r} \\
 Z &= \left(R + r \cos \frac{x}{r}\right) \sin \frac{y}{R+r},
 \end{aligned} \tag{1}$$

where two-dimensional coordinates $\{x, y\}$ are used to express three-dimensional space coordinates $\{X, Y, Z\}$. In this way, 3-D space coordinates can be mapped directly into the 2-D domain, and vice versa.

2.1.2 Acoustic wave equation

The concept of the 2-D acoustic model is rooted in the theory that guided waves propagating along a bend wall of varying thickness will mirror the behavior of an acoustic wave journeying through a 2-D medium with differing velocity, as visually depicted in Figure 5.

This complex phenomenon can be simplified and effectively modeled using a linked system of second-order partial differential equations. This compelling transformation translates the acoustic wave into a portrayal of a vertical transversely isotropic (VTI) medium, a concept widely recognized and cited in the field [46, 47]. The mathematical model is represented as follows:

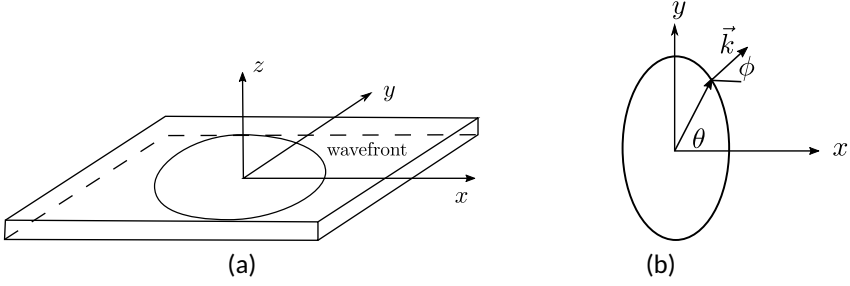


Figure 5: **(a)** Acoustic representation of GW propagation in a vertically transversely isotropic plate. **(b)** top perspective of the wave-field, tilt angle θ , wave number \vec{k} , and phase angle ϕ (from **Publication I**).

$$\begin{cases} \frac{1}{v^2} \frac{\partial^2 p}{\partial t^2} - (1 + 2\delta)Hp - H_0p = (1 + 2\delta)Hq, \\ \frac{1}{v^2} \frac{\partial^2 q}{\partial t^2} - 2(\varepsilon - \delta)Hq = 2(\varepsilon - \delta)Hp. \end{cases} \quad (2)$$

The defining differential operators H and H_0 within the model are mathematically represented as:

$$\begin{cases} H = \cos^2 \theta \frac{\partial^2}{\partial x^2} + \sin^2 \theta \frac{\partial^2}{\partial y^2} - \sin 2\theta \frac{\partial^2}{\partial x^2 \partial y^2}, \\ H_0 = \sin^2 \theta \frac{\partial^2}{\partial x^2} + \cos^2 \theta \frac{\partial^2}{\partial y^2} - \sin 2\theta \frac{\partial^2}{\partial x^2 \partial y^2}. \end{cases} \quad (3)$$

In the core context of Equation (2), p symbolizes the pressure field of the wave as it propagates, q signifies an auxiliary wave field, v denotes the pressure phase velocity, θ the angle of symmetry axis with respect to the x -axis, and the nondimensional parameters ε and δ are deployed to portray the anisotropy of the wave field, as supported by Thomsen's study [48] and **Publication I**. Furthermore, to define the Thomsen parameters ε and δ for a weak elastic anisotropy like the VTI, the phase velocity v at three exclusive angles is taken into consideration: horizontal v_0 , vertical v_v , and $v_{\frac{\pi}{4}}$. This is demonstrated through the following equations:

$$\begin{aligned} \varepsilon &= \frac{v_{\frac{\pi}{2}} - v_0}{v_0} \\ \delta &= 4 \left(\frac{v_{\frac{\pi}{4}}}{v_0} - 1 \right) - \varepsilon. \end{aligned} \quad (4)$$

Both ε and δ play crucial roles in the model, wherein ε illustrates the velocity discrepancy between the wave propagation along the vertical axis, and δ signifies the wave propagation across intermediate phase angles. Note that in Equation 4, ε and δ are calculated based on the phase velocities at three distinct angles, which can be directly measured in plates [49]. For the implementation in a pipe bend, one might initially consider measuring these velocities and substituting them directly into Equation (4). However, this raises the question: *How can v_0 , v_v , and $v_{\frac{\pi}{4}}$ be measured on a pipe bend?*

2.1.3 Implementation for a pipe bend

The study of wave propagation on curved pipe sections presents its unique set of challenges. A crucial part of this is pinning down the parameters ε and δ , which are necessary to illustrate the virtual anisotropy exhibited by the pipe bend in the 2-D domain. Brath et al., in their seminal work [40], shed light on this issue. They demonstrated that guided waves traveling within a torus display elliptical anisotropy. Expounding on this, they gave birth to the non-dimensional parameter ρ_e , which encapsulates the vertical velocity variation v_v , as a derivative of the phase velocity v as shown below:

$$v_v = \frac{v}{\rho}, \quad (5)$$

and,

$$\rho_e = \frac{R + r \cos(\alpha)}{(R + r)}. \quad (6)$$

The case of a VTI medium warrants further inspection. The relationship that exists between the phase velocity and the velocity along the symmetry x -axis is expressed as [47]:

$$\frac{\cos^2 \bar{\theta}}{v_v^2} = \frac{1}{v^2} - (1 + 2\delta) \frac{\frac{\sin^2 \bar{\theta}}{v_v^2} \frac{1}{v^2}}{\frac{1}{v^2} - 2(\varepsilon - \delta) \frac{\sin^2 \bar{\theta}}{v^2}}. \quad (7)$$

Here, $\bar{\theta}$ highlights the angle of the symmetry axis in reference to the x -axis. Crucially, for a VTI medium, $\bar{\theta} = \pi/2$, and with the elliptical anisotropy condition where $\varepsilon = \delta$ [46], substituting these values into Equation (7) gives us:

$$\varepsilon = \delta = \frac{1}{2} \left(\frac{1}{\rho_e^2} - 1 \right). \quad (8)$$

Working with ε and δ allows us to use Equation 2 to portray guided wave propagation in a pipe bend. It is critical to note, however, that the 2-D Finite Difference (FD) model presents a simplified interpretation of the more intricate 3-D wave propagation model. This approximation, while useful, may impose certain restrictions on the inversion process, especially when the data used for modeling present considerable divergence [31].

2.2 Full-waveform inversion

In Chapter 2.1, the forward problem was presented as an approach that efficiently computes wavefield data in a pipe bend. The resultant data, now denoted as $\mathbf{u}(\mathbf{m}(\omega))$, is a function of the angular frequency, ω . This process is enacted based on an explicit emission-transmission setup and a unique set of parameters, \mathbf{m} , that are determined at every point (x, y) on the 2-D grid showcased in Figure 4(b).

In the domain of guided wave tomography, the target is to distinguish a set of parameters, \mathbf{m} , which facilitate the creation of synthetic wavefields, $\mathbf{u}(\mathbf{m})$. The produced synthetic wavefields are intended to be as congruent as possible with the experimental measurements, $\mathbf{d}(\mathbf{m})$.

The residual error is defined as

$$\Delta \mathbf{d} = \mathbf{u}(\mathbf{m}) - \mathbf{d}(\mathbf{m}), \quad (9)$$

with an assumed dependency on ω . In this equation, $\mathbf{u}(\mathbf{m})$ is the wavefield computed by (2), while $\mathbf{d}(\mathbf{m})$ is the empirically observed wavefield. The essence of the inversion algorithm lies in discovering \mathbf{m} that minimizes $\Delta\mathbf{d}$. Therefore, the inverse problem is structured to minimize the summation of squared residuals:

$$\min_{\mathbf{m}} f(\mathbf{m}) = \frac{1}{2} \Delta\mathbf{d}^T \Delta\mathbf{d}, \quad (10)$$

where $\min_{\mathbf{m}} f(\mathbf{m})$ represents the l_2 norm misfit function, and $\Delta\mathbf{d}^T$ indicates the conjugate transpose of the residual error. Throughout this research, the non-linear waveform inversion problem is tackled using the Seiscope optimization tool [50]. Seiscope addresses the inversion problem by employing the gradient method: it commences with an initial model (observed data), and an initial forward-modeling step is conducted to compute the data residuals in Equation (9). Updated models are iteratively derived by modifying \mathbf{m} according to

$$\mathbf{m}_{k+1} = \mathbf{m}_k - a_k \Delta m_k, \quad (11)$$

where k represents the iteration number, a is the scalar magnitude of the model update, and Δm_k is the gradient of the misfit function relative to the model parameters. The model perturbations are computed by multiplying the gradient of the objective function by a step length a , which is recalculated at each iteration for accuracy. To represent the algorithm visually, a flow diagram is provided in Figure 6.

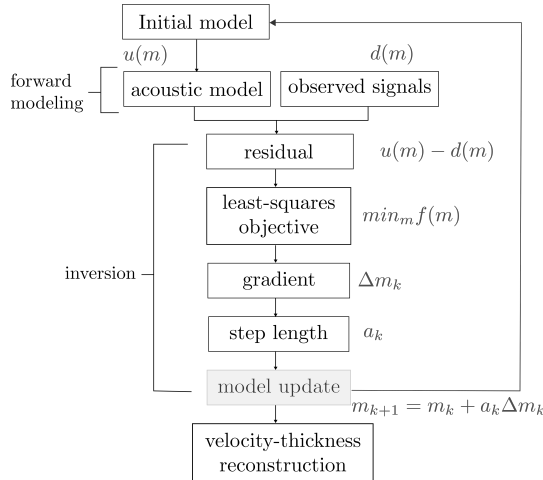


Figure 6: Flow diagram depicting the full-waveform inversion algorithm. The inverse problem is designed to incrementally minimize the sum of squared residuals (from **Publication III**).

3 Methods

3.1 Pipe Bend Specimen

The focus of the subsequent chapters in this thesis is on the experimental and numerical analyses of a steel pipe specimen, as illustrated in Figure 7. The specimen features an interior radius of $r_{in} = 0.1015$ m, an exterior radius of $r_{out} = 0.1095$ m, and a 90-degree bend with a radius of $R = 0.329$ m. Additionally, it includes two straight pipe segments, each measuring 0.20 m in length, positioned at both the start and finish of the bend. Steel's properties are provided in Table 1.

From this point forward, the terminology used to refer to the longest and shortest arcs of the bend will be *extrados* and *intrados*, respectively. Conversely, the mid-bend arc located between the intrados and extrados will be referred to as *top* and *bottom*. This study also incorporates the deployment of twenty evenly spaced measurement points across each terminal of the pipe bend, referred to as ring (A-B), as depicted in Figure 7(c). The guided waves were excited individually at both rings and measured from the opposing ring, resulting in a total of 20 time traces for each transmission. Consequently, this methodology generated a total of 800 time traces from the 40 emissions.

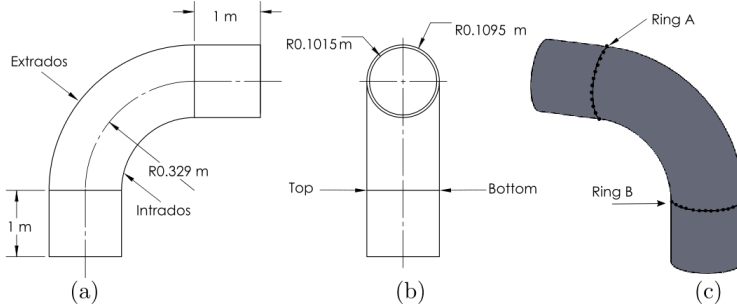


Figure 7: Illustration of the pipe bend. (a) Aerial view, (b) Side view, and (c) Perspective view of the conceptualized pipe bend (from **Publication I**).

ρ (kg/m^3)	E_m (GPa)	ν
7932	216.9	0.2865

Table 1: Material attributes of the steel pipe: Density ρ , Young's modulus E_m , and Poisson ratio ν .

3.2 Numerical Methods

3.2.1 FE Modeling

The 3-D guided wave propagation simulations in pipe bends were conducted using the software Abaqus Explicit [51], as demonstrated in Figure 7. The construction of the bend section commenced with the creation of a circular mesh, comprising 560 individual elements around the circumference of the pipe and 6 through the thickness. This mesh was subsequently adapted to align with the geometry of the pipe bend, as depicted in Figure 8. This geometric adjustment extended over a 90-degree rotation, incorporating 550 elements. Throughout this process, the element type C3D8R, an 8-node brick, was utilized.

To mitigate potential disturbances caused by boundary reflections, absorbent regions

were established within the straight sections of the pipe, in line with the approach suggested by [52]. Each of these straight segments comprised 160 circumferential layers. At one extremity of the bend, the generation of the A_0 mode was facilitated through the application of an out-of-plane force applied radially on the pipe surface.

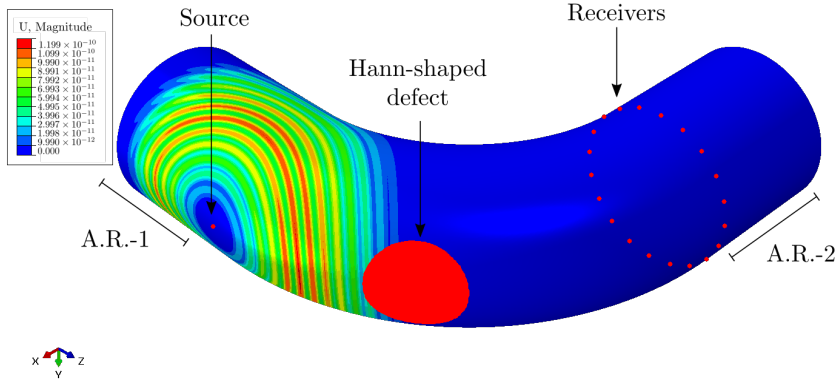


Figure 8: Configuration of the pipe simulated in ABAQUS, exhibiting a Hann-shaped defect, absorbing areas 1 and 2, and propagating wave displacements at $100 \mu\text{s}$ (from **Publication I**).

Beyond mere transmission observations, the investigation also examined the scattering from Hann-shaped defects. The uniqueness of the defect wavefield was determined by implementing baseline wavefield subtraction.

3.2.2 Acoustic Modeling

Investigations were conducted in the acoustic domain using the finite difference (FD) method. This encompassed the exploration of guided wave propagation and phase velocity reconstructions, taking advantage of the mixed-grid method [53]. Within the computational domain, three replicas were present to accommodate the intricate higher-order helical wave trajectories in the simulation [40]. The discretization of each replica involved 161 grid points circumferentially and 166 grid points axially, with a grid interval of 4.143 mm applied.

The distribution of Thomsen parameters along with the velocity distribution on the bend is exemplified in Figure 9. Isotropic wave propagation occurs along the bend's extrados where the Thomsen parameters are nullified. However, as the waves progress through the intrados, they transition to an increasingly anisotropic state, where Thomsen parameters reach their peak. The velocity models for the required frequency were inferred from the thickness map, relying on the A_0 velocity-frequency-thickness dispersion curve.

The two-dimensional frequency-domain engine, TOY2DAC [50], was employed to resolve Equation (2) for the relevant frequency components in the frequency domain. It also addressed the minimization challenge represented by Equation (10) for a specific frequency. The conversion of frequency-domain results into the time domain was enabled through the inverse fast Fourier transform. Calculations were performed on a cluster equipped with 2 x Intel Xeon E5-2660v2 and 64 GB of RAM, with a computing duration of 7 minutes for one excitation scenario.

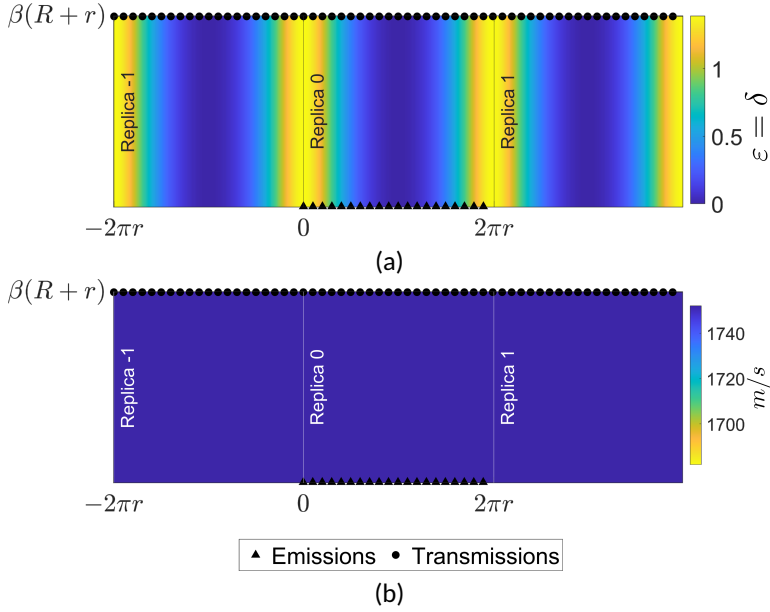


Figure 9: Figure (a) shows ϵ and δ distribution along the bend with 3 replicas. Sources are positioned at the central replica. Figure (b) shows background phase velocity v_0 at 50 kHz (from **Publication III**).

3.2.3 Hann-Shaped Defect

To investigate the dispersion of waves due to anomalies, a defect exemplified as a Hann-shaped reduction in thickness, located at a central point $\{X_c, Y_c, Z_c\}$, was constructed by adjusting the thickness T of the pipe from its outer surface. This was achieved through the following equation:

$$T = \begin{cases} T_0 - \frac{D}{2} \left[1 + \cos \left(\frac{2\pi|T|}{W} \right) \right], & |T| < \frac{W}{2} \\ T_0, & |T| > \frac{W}{2} \end{cases} \quad (12)$$

In this equation, $|T| = \sqrt{(X - X_c)^2 + (Y - Y_c)^2 + (Z - Z_c)^2}$ signifies the absolute value of T . Here, T_0 denotes the initial thickness of the pipe, while D and W represent the deterioration depth and width, respectively. Figure 10 illustrates the location of an arbitrary Hann-shaped defect, positioned at three variations: extrados, top, and intrados. Initially, the defect takes on a round shape at the extrados; however, it morphs into an elliptical configuration as it transitions towards the intrados. Naturally, this reshaping is triggered by the unwrapping of the bend.

3.3 Data and Experimental Preconditioning

3.3.1 Chirp Excitation

In this thesis, a broad frequency range of 10 to 80 kHz was explored using a broadband chirp to collect data. This was followed by applying deconvolution to isolate multiple narrowband responses [54]. This approach enables examination across various frequencies, achieving a high signal-to-noise ratio and consequently reducing the time required for

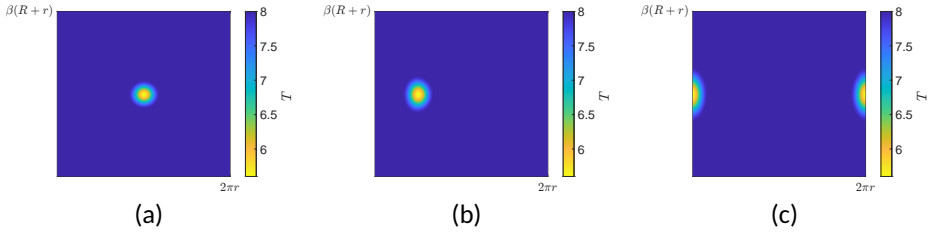


Figure 10: Thickness T (mm) in the 2-D acoustic domain with a Hann-shaped defect at three different locations: (a) extrados, (b) top, and (c) intrados (from **Publication I**).

data collection. The mathematical representation of a typical chirp is given by:

$$s_c(t) = w(t) \sin \left(2\pi f_0 t + \frac{\pi B t^2}{t_c} \right) \quad (13)$$

In this equation, f_0 represents the initial frequency, t_c denotes the duration of the chirp, B indicates the chirp bandwidth, and $w(t)$ corresponds to a rectangular window of unit amplitude extending over $[t, T]$. After optimizing the frequency and duration for the necessary tone burst excitation $s_d(t)$, an extended narrowband chirp $s_c(t)$ is introduced as the actual excitation. The required tone burst response $r_d(t)$ is then extracted in the frequency domain from the transmitted chirp response $r_c(t)$, as demonstrated in the equation:

$$R_d(\omega) = R_c(\omega) \frac{S_d(\omega)}{S_c(\omega)} \quad (14)$$

In this instance, uppercase letters represent the Fourier transform, with ω symbolizing the angular frequency.

As illustrated in Figure 11(a), the input chirp applied in this study is displayed alongside a sample tone burst modulated by a Hanning window. This tone burst features a central frequency of 44 kHz and includes five cycles, which is extracted prior to further examination for each transmitted time trace Rx. Figure 11(b) presents the transmitted chirp response for a section of a pipe bend at the point of excitation located in the intrados position. The desired response is also shown in Figure 11(c). Notably, the interference caused by cross-talk is significantly reduced in Figure 11(c), as are the peaks of the time traces.

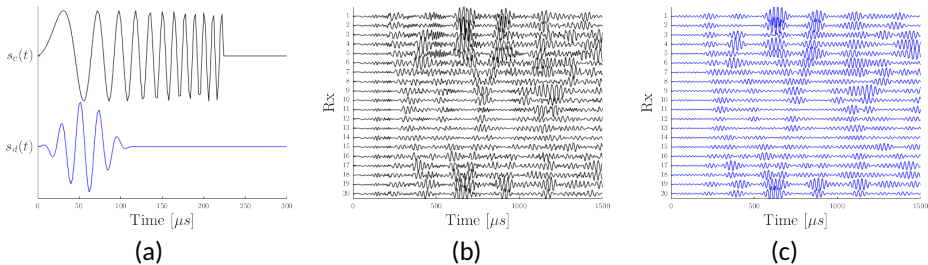


Figure 11: Excited chirp function $s_c(t)$ and desired tone burst modulated with a Hanning window and a central frequency of 44 kHz and 5 cycles $s_d(t)$ in (a). Transmitted chirp response $r_c(t)$ in the pipe bend specimen from Figure 7 when exciting at the intrados position (b) and the extracted response $r_d(t)$ (c).

3.3.2 Helical Path Separation

The existing 2-D acoustic model, as denoted by Equation (2), does not account for the repetitive structure of a pipe within a predefined area marked by two transducer rings. To effectively segregate the primary transmitted wave packet based on the collected experimental data, a robust helical path separation algorithm [55] was adopted.

Within this separation algorithm, the time sequences $u_{r,s}(t)$ emerging from emission s and intercepted at transmission r are duplicated m times, resulting in $u_{r+Nm,s}(t)$. Here, N represents the total number of sources, m denotes the number of duplications, and Nm signifies the increment in each receiver transducer number.

The first wave packet $u_{\tilde{r},s}^{hp}(t)$ is isolated from the duplicated time sequences $u_{\tilde{r},s}(t)$ by subtracting the waveforms associated with other duplicated sequences. Formally, this is expressed as:

$$u_{\tilde{r},s}^{hp}(t) = u_{\tilde{r},s}(t) - \phi_{\tilde{r}+Nm,s}(t), \quad (15)$$

where the resultant wavefield $\phi_{\tilde{r}+Nm,s}(t)$ is obtained by time-reversing $u_{\tilde{r},s}(t)$, applying several band-pass filters and windows, and finally forwarding it again. A graphical illustration of the helical path separation algorithm can be seen in Figure 12.

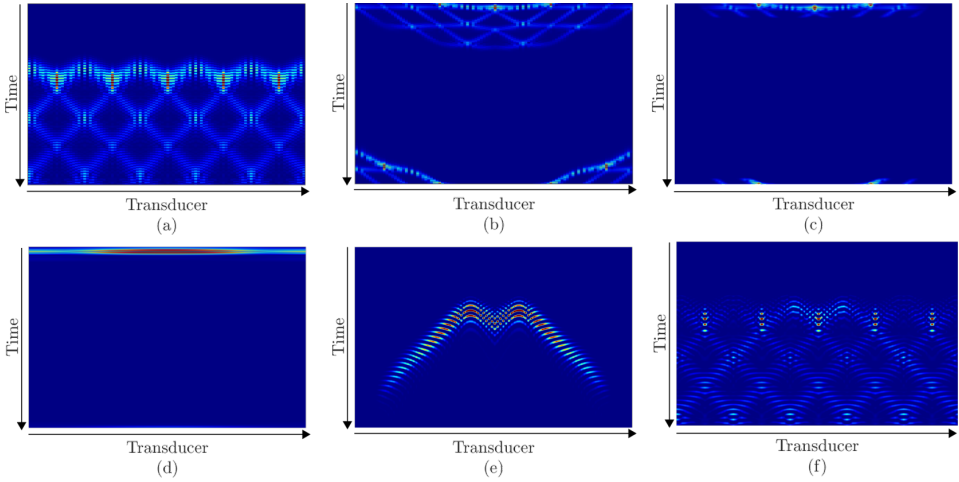


Figure 12: This figure illustrates a single iteration of the helical path separation algorithm as referenced in [55]. Here, $N = 20$ and $M = 5$. The simulation data originates from a finite element model of the pipe bend setup as detailed in Section 3.1. Initially, signals are replicated five times as depicted in (a). The wavefield is then reversed in time to align the first-arrived wavefront, shown in (b). A window is applied in stage (c) to eliminate the majority of unwanted helical paths. Subsequently, in (d), another window is applied in the wavenumber-frequency domain to filter out higher-order modes using a 2D-FFT. The purged waveform is then forwarded, as shown in (e). In the final stage (f), the purged signals from (e) are horizontally translated and subtracted from all the helical modes in (a), excluding the central mode. The cleared waveform is now ready for the next iteration, where additional 2D-FFT components may be included (from **Publication II**).

The time-reversal step is mathematically represented as:

$$\overleftarrow{U}_{\tilde{r},s}(\omega) = \text{FFT}(u_{\tilde{r},s}(t)) \exp[-ik(\omega)x_{\tilde{r},s}], \quad (16)$$

where $k(\omega)$ denotes the wavenumber and $x_{\tilde{r},s}$ represents the distance covered by the ray from source s to receiver \tilde{r} . It is crucial to note that Equation (16) is dependent on the distance traveled by the ray $x_{\tilde{r},s}$. Therefore, determining the shortest path $x_{\tilde{r},s}$ is imperative for successful implementation.

3.3.3 Shortest Path Using the Geodesic Equations

In a conventional setup for a straight pipe transducer array, the distance $x_{s,r}$ is intuitively a straight line [56, 57]. However, in complex geometries, such as a pipe bend, the shortest route between points s and r takes the form of a geodesic. Thus, the task of eliminating the helical path using any helical path separation technique becomes more complex due to the necessity of calculating this minimal transmitted path [55, 58].

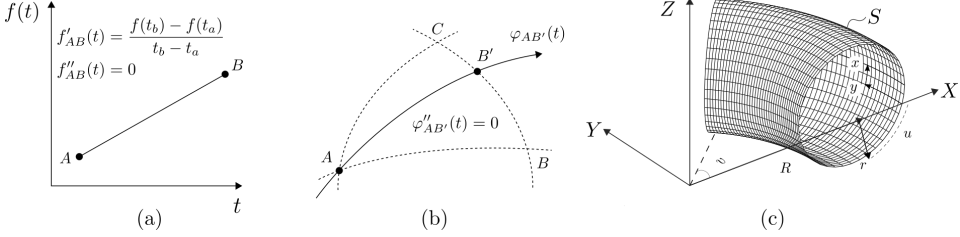


Figure 13: In (a), the direct route between points A and B is the straight line $f_{AB}(t)$, where $f''_{AB}(t) = 0$. In (b), on the arbitrary surface S defined by vertices A, B , and C , the geodesic $\varphi_{AB'}(t)$ represents the shortest path between A and B' , with $\varphi''_{AB'}(t) = 0$. In (c), the torus section S illustrates the bend of a pipe in the 3D domain (from **Publication II**).

Consider two arbitrary points A and B on a plane, as illustrated in Figure 13(a). The minimum distance between A and B is represented by a linear path, denoted by $f_{AB}(t)$, which passes through both points. Here, $f(t)$ represents the plane's position as a function of time, t . In this context, the first derivative $f'_{AB}(t)$ is the slope of the straight line $f_{AB}(t)$ or the velocity, which remains constant. Therefore, a particle traveling along $f_{AB}(t)$ will have zero acceleration, represented as $f''_{AB}(t) = 0$. In simple terms, the shortest route connecting points A and B is traced by a particle moving at a constant speed on a plane.

Similarly, on a geometric surface S , a curve $\varphi(t)$ is considered a *geodesic* if its acceleration is zero (i.e., $\varphi''(t) = 0$), or when it is perpendicular to the surface's tangent plane at the point $\varphi(t)$ [59]. Figure 13(b) demonstrates this concept, where A, B , and C are vertices of a triangle on surface S . The shortest path between A and B' is represented by the curve $\varphi_{AB'}(t)$, where $\varphi_{AB'}(t)$ denotes the position on surface S as a function of time t .

The geodesic equations for a parametric surface $S(u(t), v(t))$, where $u(t)$ and $v(t)$ denote the circumferential and longitudinal positions respectively as a function of time t , are conventionally expressed as given by [60]:

$$\begin{aligned} \ddot{u} + \frac{E_u}{2E} \dot{u}^2 + \frac{E_v}{E} \dot{u}\dot{v} - \frac{G_u}{2E} \dot{v}^2 &= 0 \\ \ddot{v} + \frac{E_v}{G} \dot{u}^2 + \frac{G_u}{G} \dot{u}\dot{v} + \frac{G_v}{2G} \dot{v}^2 &= 0, \end{aligned} \quad (17)$$

along with

$$\begin{aligned} E &= S_u S_u & E_u &= 2S_{uu} S_u \\ F &= S_u S_v & E_v &= 2S_{uv} S_{uv} \\ G &= S_v S_v & G_u &= 2S_{vu} S_v \\ & & G_v &= 2S_{vv} S_v. \end{aligned} \quad (18)$$

Here, the top superscripts \cdot and $\ddot{\cdot}$ denote the first and second derivatives with respect to time, while the subscripts u and v indicate the derivatives with respect to positions u and v .

Considering the toroidal section illustrated in Figure 13(c), defined in a 3-D domain with mid-thickness or central radius r , bend radius R , toroidal azimuth longitude v about the Z -axis, and toroidal latitude u with respect to the XZ plane, by incorporating the parametric toroidal surface $S(u, v) = \{(R + r \cos(u)) \cos(v), (R + r \cos(u)) \sin(v), r \sin(u)\}$ into (17) and, after some algebraic manipulation, the geodesic equations for the torus can be represented as an ordinary differential equation system [61]:

$$\begin{aligned}\dot{\varphi}_1 &= \varphi_2 \\ \dot{\varphi}_2 &= -\frac{1}{r} \sin(\varphi_1)(R + r \cos(\varphi_1))\varphi_4^2 \\ \dot{\varphi}_3 &= \varphi_4 \\ \dot{\varphi}_4 &= \frac{2r \sin(\varphi_1)}{R + r \cos(\varphi_1)} \varphi_2 \varphi_4,\end{aligned}\tag{19}$$

where $\varphi_1 = u$, $\varphi_2 = \dot{u}$, $\varphi_3 = v$, and $\varphi_4 = \dot{v}$.

Figure 14 shows three excitation points on the bend: intrados (a), top (b), and extrados (c), along with their shortest paths towards 20 evenly distributed monitoring points. Additionally, the traveled distance x_{AB} can be determined through a simple numerical integration of the geodesic path $\varphi_{AB}(t)$. This methodology is particularly useful in the context of structural health monitoring and guided wave propagation for determining the shortest path between any configuration of a transducer array. Further information on the numerical computation of the shortest path is elaborated in **Publication II**, and extended applications of shortest path trajectories for detecting fouling in a pipe bend are detailed in **Publication VI**.

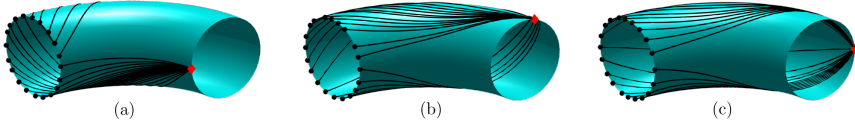


Figure 14: Shortest paths from three distinct starting points: intrados (a), top (b), and extrados (c); along with 20 evenly spaced monitoring points around the torus latitude (from **Publication II**).

3.3.4 Autocalibration

Considering the dependence of the inversion algorithm on finite difference (FD) acoustic modeling, it is essential to adjust or re-scale the data pertaining to the acoustic model. This adjustment is necessary regardless of whether the data is obtained through simulations or experimental means [6]. Calibration is required to rectify any inconsistencies between the two models. Traditionally, the calibration factor Q is measured as

$$Q_{r,s} = \frac{U_{r,s}(\omega)}{D_{r,s}(\omega)},\tag{20}$$

where $U_{r,s}$ and $D_{r,s}$ indicate the transmitted data from r to s by FD modeling and the observed data, both in the frequency domain, respectively. According to previous studies, $Q_{r,s}$ is typically computed with a reference data set, where $D_{r,s}$ is the transmitted data devoid of any flaw or by manually selecting a ray where the propagation field is unblemished [31, 43, 49, 62]. However, in practical scenarios, a reference data set may be (a) inaccessible or (b) could lead to erroneous alarms [63].

In this research, an auto-calibration method for the re-scaling phase was adopted, as proposed by [64]. Essentially, the auto-calibration approach entails determining the

defect location and using the so-called *healthy* rays to calculate the average \bar{Q} for those rays near the flaw. In summary, $Q_{r,c}$ is established in three phases:

1. **Localization of the defect.** Initially, a baseline velocity model is established, achievable through algorithms grounded on ray tomography [64].
2. **Choosing the healthy rays.** Next, all ray paths $U_{r,s}^d$ near the flaw are removed, maintaining a threshold distance of 1%, preserving only the unblemished rays $U_{r,s}^h$ for the subsequent step.
3. **Computation of the confidence ellipse.** Subsequently, a 95% confidence ellipse of the calibration factors $Q_{r,s}^h$ of the remaining ray paths $U_{r,s}^h$ is calculated. The calibration factors for all the ray paths outside the confidence ellipse are set to the mean of the rays contained inside the ellipse, as expressed in:

$$\bar{Q} = \frac{1}{P} \sum_{p=1}^P (Q_x^p + iQ_y^p), \quad (21)$$

where subscripts x and y denote the real and imaginary components, and p represents the calibration factor number.

Additionally, considering that the calibration factors for the unblemished rays $Q_{r,s}^h$ should approximate the average, the defect's position can also be ascertained by directly performing step III with a modest level of confidence (e.g., 65%). However, this method may generate additional artifacts in the reconstructed wavefield, which is why steps 1 and 2 are critical for enhancing accuracy.

Moreover, it is important to recall that $Q_{r,s}$ is a complex number expressed as $Q = ze^{i\psi}$, where ψ signifies the phase and z represents the amplitude, defined as $z^p = |Q_x^p + iQ_y^p|$. However, Equation (21) primarily considers the phase information, since \bar{Q} is the geometrical average of the distribution of Q^p points. It follows that $|\bar{Q}| \neq \bar{z}$.

Furthermore, if the amplitudes of the observed data are not calibrated, there is a risk of being caught in local minima during the inversion, thus converging into a wrong solution [65, 66]. Therefore, the incorporation of amplitude data in the auto-calibration method is proposed as follows:

$$\bar{Q} = \frac{1}{P^2} \sum_{p=1}^P (Q_x^p + iQ_y^p) \cdot \sum_{p=1}^P |Q_x^p + iQ_y^p|. \quad (22)$$

Note that Equation 22 is the product of the mean phase \bar{Q} and the mean amplitude \bar{z} .

In Figure 15(a), the velocity field of a pipe bend with an arbitrary defect located at the center of the surface is depicted. By computing a 65% confidence ellipse with all the transmitted measurements, the defect was identified, and $Q_{r,s} = \bar{Q}$ was established for those rays outside the confidence ellipse. Then, in Figure 15(b), the rays near the flaw were eliminated to compute the calibration factors $Q_{r,s}$. Note that the rays are bent due to the anisotropy of the wave field. Additional details and analysis on the effects of Equations (21) and (22) on the inversion reconstruction are given in **Publication IV**.

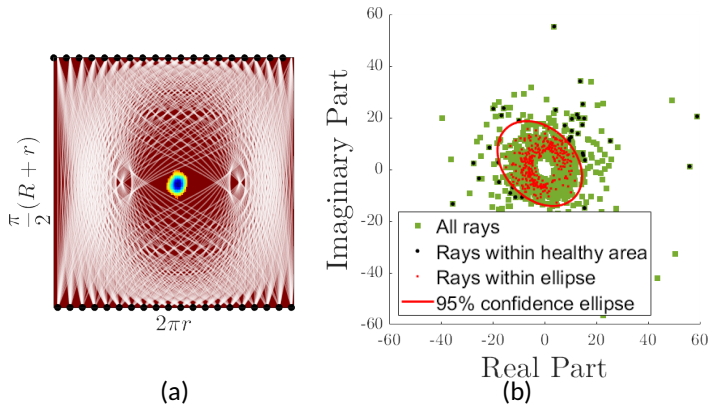


Figure 15: All the rays used in order to calibrate $D_{r,s}$ (a), and calibration factors $Q_{r,s}$ plotted in the complex plain (b) (from **Publication IV**).

3.4 Instrumentation

3.4.1 Measurements of Guided Waves

The experimental setup, illustrated in Figure 16(a), utilized a curved steel pipe supported by four wooden pillars. Its specifications and dimensions, detailed in Table 1 and Figure 7, were consistent with those previously reported. The linear sections of the pipe were maintained at 1 m in length to prevent reflections from the ends during measurements.

This measuring system was designed with two transducer rings positioned at both ends of the curved pipe, a multiplexer for generating signals, and a data acquisition unit. Transducer Ring A and Ring B each contained twenty individual piezoelectric transducers (sourced from Doppler Ltd, Guangzhou, China), operating at an average frequency of approximately 44 kHz. Each transducer served as both a signal transmitter and receiver.

The transducers were evenly distributed around the pipe's circumference and secured using springs, allowing them to initiate radial excitation and measure radial displacement with the receiving transducer ring. Sensor no. 1 was located at the inner curve of the pipe bend, referred to as the *intrados*. Sensor no. 6 was positioned at the *top*, while sensor no. 11 was situated at the *extrados*, or the outer curve of the pipe bend.

The multiplexer used in this setup featured 20 channels specifically designed for amplifying and conditioning the measured responses. This configuration allowed for the excitation signal to be sent to any transducer on one ring while maintaining the receiving channels connected to all elements on the opposite ring. Further details regarding the instrumentation can be found in **Publication I**.

3.4.2 Impedance Measurements

Throughout the course of this work, the transducers displayed high variability in performance. Initially, this was attributed to coupling conditions, as it was physically challenging to apply the same force to press them against the pipe uniformly. As a result, the time-of-flight (TOF) measurements varied among the transducers, making direct comparisons difficult. Figure 17 illustrates the TOF and amplitude variations across three replicas when exciting the structure at the intrados, top, and extrados. While the TOF plots from the measurements correspond with the numerical model, the amplitude values show a random distribution.

Since 120 identical model transducers were available, but only 40 were needed for

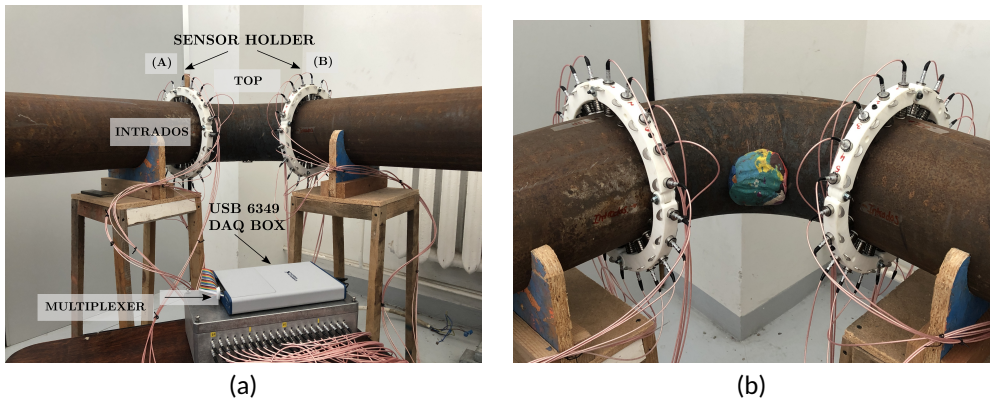


Figure 16: (a) Steel pipe bend specimen with characteristics consistent with Table 1. Measurement setup showing transducer arrays (A) and (B), each with 20 transducers and an acquisition system; (b) Pipe bend with an artificial defect made from plasticine located on the intrados, viewed from the intrados (from **Publication I**).

the measurement setup described in Section 3.4.1, transducers with similar resonance frequencies were selected. To achieve this, their impedance resistance was measured using a Digilent oscilloscope [67].

The impedance measurement process involved applying a sinusoidal excitation current to the transducer and measuring the response voltage across it. The frequency range was logarithmically divided into 500 points, with the measurement repeated at each point to explore the relevant spectra.

The transducers exhibited multiple resonance peaks ranging from 40 kHz to 70 kHz. The precise resonance frequencies of each transducer were identified by locating the peak points in their impedance measurements, allowing for the categorization of the sensors.

While this method does not provide a direct measure of sensitivity, it relies on the impedance spectra, which reflect the sensors' physical properties. This approach is deemed sufficient for classifying the sensors, aiming to minimize potential errors arising from sensitivity variations.

Figures 18(a) and (b) display a histogram of the measured resonance frequencies and the impedance resistance as a function of frequency, respectively. Although the transducers are of the same model, Figure 18(a) reveals two distinct Gaussian distributions, one centered around 44 kHz and the other around 55 kHz, likely due to manufacturing inconsistencies.

Transducers were selected with a resonance frequency of 44 kHz, as this was the most common range among the available units. The selection process involved systematically reducing a confidence interval from 95% in decrements of 5% until at least 40 transducers fell within the range, resulting in a final confidence level of 75%, as shown in Figure 18(b).

Moreover, an increasing discrepancy in performance relative to resonance frequency is observed in Figure 18(b). This variance can be attributed to the substantial heat produced by piezoelectric transducers at resonance, leading to decreased efficiency [68].

Therefore, based on the impedance measurements, the most consistent operating range for the transducers was found to be between 20 and 40 kHz, as indicated by the dashed lines in Figure 18(b).

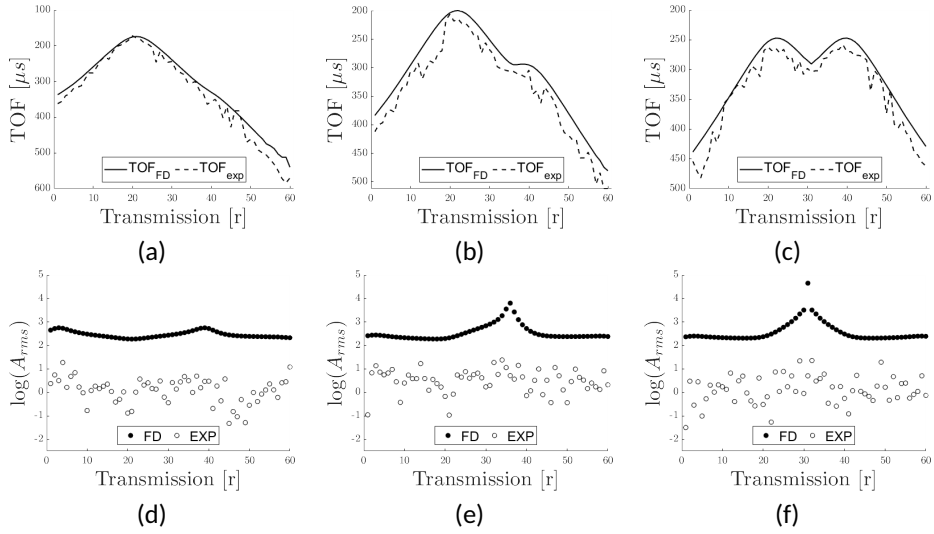


Figure 17: Time-of-flight (TOF) and logarithmic root mean square amplitudes from forward modeling and experimental measurements. TOFs from the intrados (a), top (b), and extrados (c), along with their respective amplitude variations (d)-(f) (from **Publication III**).

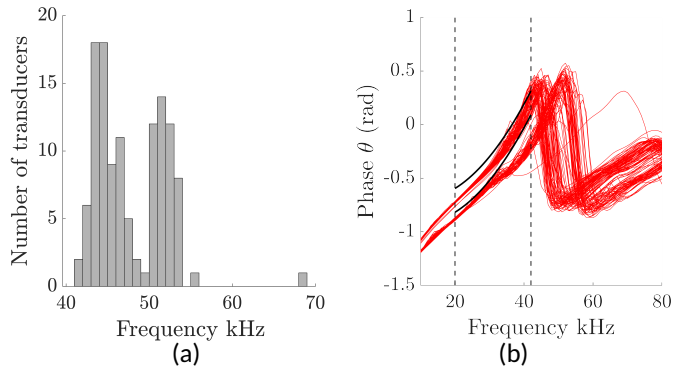


Figure 18: A histogram of the 120 resonance frequencies is shown in (a), while (b) presents the impedance resistance as a function of frequency. In (b), the dashed lines indicate the most reliable operating interval for the transducers, and the solid lines encompass the transducers within a 75% confidence interval (from **Publication IV**).

4 Experiments and Results

The primary objective of this thesis is to achieve guided wave tomography based on full waveform inversion for a pipe bend. To accomplish this, the workflow necessitated three principal steps: (i) the development of an acoustic forward model, (ii) the preconditioning of the experimental data, and (iii) the integration with full waveform inversion tomography. Consequently, this chapter encapsulates the results from all four publications. The pipe bend specimen is described in Section 3.1, along with the numerical methodologies for FD and FE modeling in Section 3.2.

In **Publication I**, an acoustic forward model for the wavefield propagating in the pipe bend was introduced. The elliptical anisotropy was synthetically rendered anisotropic by utilizing the anisotropic Thomsen parameters ε and δ , which modify the wavefield across the circumference.

The preconditioning of the data prior to its integration with full waveform inversion was addressed in **Publication II** and **Publication IV**. **Publication II** presented a methodology to extract the first-arriving wave packets in curved geometries using the geodesic equations, thereby fully translating the cyclic nature of guided wave propagation in pipes into a 2-D domain. Additionally, **Publication IV** proposed an updated version of the re-scaling step needed to mitigate artifacts resulting from the disparity between the elastic and acoustic models, as well as the substantial experimental uncertainties arising from the inhomogeneous performance of the transducers.

Lastly, **Publication III** presents a numerical study of the thickness map reconstruction, complemented by an experimental validation.

4.1 Acoustic Forward Modeling for a Pipe Bend

4.1.1 Guided Wave Propagation

The precision of the acoustic forward model in simulating guided wave propagation within a bend was assessed through experiments. These experiments excited the A_0 mode at 50 kHz in three distinct locations within the bend: the extrados, the top, and the intrados. The resulting wavefield propagation was subsequently measured using a transducer ring located at the terminus of the bend.

This acoustic forward model was then juxtaposed with both the elastic model and the experimental findings for comparison. The results consisted of radially displaced contour plots of the received waves, as determined via both FE and FD methodologies. Represented in Figure 19, these plots were normalized according to the maximum displacement value of the recorded signals to present the wave amplitude.

Recognizing the cyclicity of the pipe, the wavefields of three separately triggered replicas were integrated into the FD model. Each of these replicas was equipped with 60 virtual transducers, a particular adaptation visible in the third column of Figure 19. This approach provided a more comprehensive representation of wave propagation within the circular structure, thereby demonstrating the potential and precision of the acoustic forward model.

It is notable that the recorded wave patterns vary for different excitation points due to the influence of differing ray paths and distances. A symmetric wave pattern is evident when the excitation is located at the extrados and intrados positions, while a non-symmetric behavior is characteristic of the excitation at the top. This is associated with the symmetry of the model parameters of the bend and the position of the excitation, as illustrated in Figure 9. Additionally, the direct first arrivals are succeeded by wave packets that are helical waves circulating around the bend multiple times. Some helical waves ar-

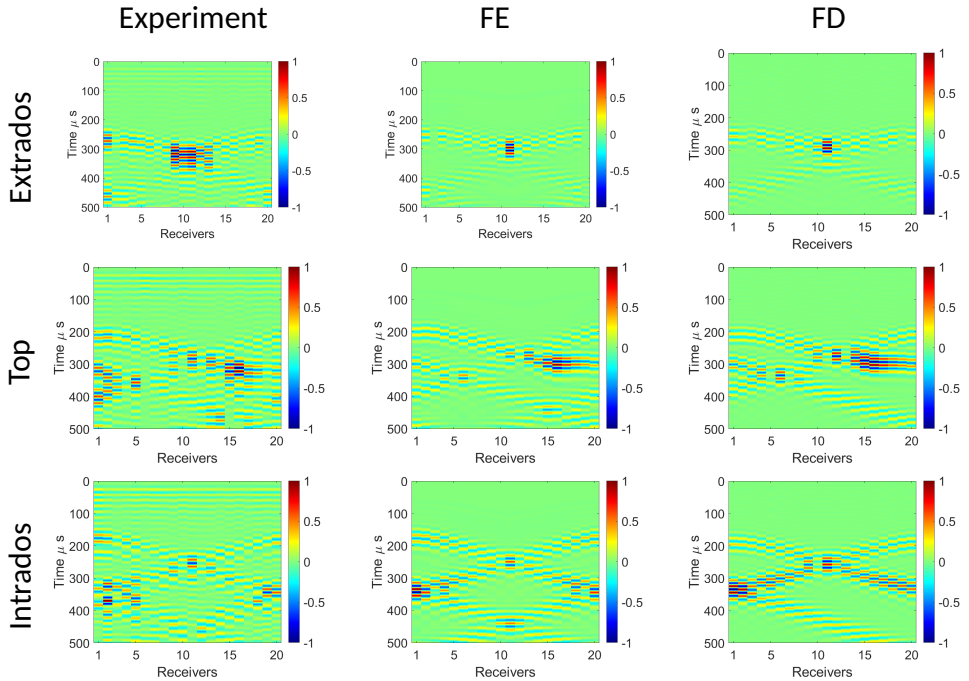


Figure 19: Experimental, FE, and FD contour plots of the normalized radial displacement in the bend for three excitation positions: extrados, top, and intrados. The A_0 mode was triggered with a central frequency of 50 kHz (from **Publication I**).

ringing after 400 μs are not visible in the FD results due to the restricted number of replicas used in the simulation.

In summary, the FD results obtained by the proposed acoustic forward model align well with the FE results, which represent the closest model to reality, as well as the experimental results. The experimental results are noisier and exhibit more amplitude variations compared to the simulation results. This discrepancy can be attributed to the uneven coupling of the transducer to the pipe surface and their inhomogeneous resonance frequencies. Furthermore, significant noise is present before 150 μs , which results from crosstalk between the transducer-source and transducer-receivers. However, the arrival times of the wave packets align well with those from the simulations, and the focusing effect in the cases of extrados and top excitation can be observed. Generally, this measurement example demonstrates the suitability of the introduced 2-D acoustic model to predict waveforms of guided waves in pipe bends.

Additional details about the acoustic forward modeling, the focusing effect, energy distribution of the wavefield as a function of the circumferential position, and the scatterring study are provided in **Publication I**.

4.1.2 Helical Path Separation for a Pipe Bend

As explained in Section 3.3.2, the 2-D acoustic forward model disregards the cyclic attribute inherent to the structure of a pipe. In the context of the previous section, it was essential to stimulate three independent replicas and merge the resulting wavefields into one central replica. This was done to mimic the higher-order helical paths due to the model's failure to account for the cyclic nature of the pipe bend. For the reduction of

complexity during the inversion process, the ideal approach was to extract the initially arrived wavefield. This approach was implemented despite several research studies integrating higher-order helical paths into their models [3, 69–71].

To illustrate the method of helical path separation, the initially arrived wave packets obtained from the experimental measurements are depicted in Figure 20. The measured wave fields across a group of 100 replicated transducers are shown in Figures 20(a) to (c) when the source of excitation is placed at various positions: the intrados, top, and extrados. The original measurements, referred to as the central replica, correspond to transducers 41–60. To ensure a standard reference scale, the amplitudes of the received waves were normalized using the largest recorded displacement value. Some noise was observed around 100 μs , likely resulting from crosstalk between the transducers. Conversely, the separated wave fields for each excited location are shown in Figures 20(d) to (f). This separation was achieved by following the procedures outlined in Section 3.3.2.

In evaluating the results, a significant observation was the complete elimination of crosstalk between the transducers, which was achieved thanks to the windowing treatment applied to the wave fields during the back-propagation phase of the helical path separation algorithm. Furthermore, Figures 20(e) and (f) show that the central replica retains the focusing effect while it is removed from higher-order replicas, providing proof that the helical path separation algorithm can withstand experimental uncertainties.

A detailed explanation of the helical path separation algorithm and its utility in the context of pipe bends is available in **Publication II**. This publication highlights the imperative nature of accurately calculating the traveled distance for the separation algorithm and provides a comparative study between using the geodesic distance and an estimated traveled distance, which is calculated as a product of the group velocity and the time of flight of the first-arrived wave packet. This comparative analysis is also applicable to scattered wavefields.

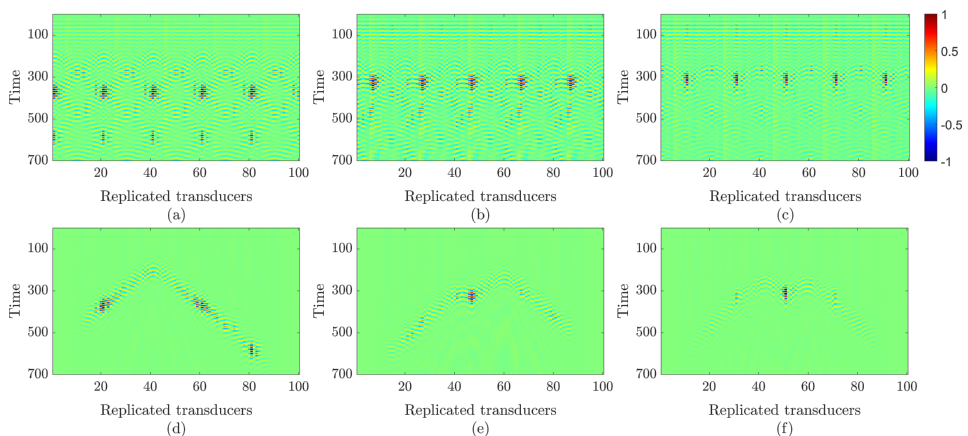


Figure 20: Experimental wave fields are presented. The A_0 mode was stimulated with a central frequency of 50 kHz. The measured wave fields, replicated 5 times, were excited at the intrados (a), top (b), and extrados (c). The wave fields extracted after the helical path separation are shown in (d)-(f). Following the helical path separation, the noise from the crosstalk is windowed, and the focusing effect remains intact (from **Publication II**).

4.2 Guided Wave Tomography Based on Full Waveform Inversion for a Pipe Bend

4.2.1 Numerical Study

The principal impediment of tomographic methodologies based on travel-time for pipe bends is the restricted precision in identifying defects in close proximity to the extrados position. The limited reach of the ray paths in the bend can be exemplified via Figure 21, which exhibits the proclivity of the ray paths amid three excitation points: intrados (a), top (b), and extrados (c). Naturally, due to the elliptically anisotropic phase velocity being at its highest at the intrados position, the rays predominantly converge towards the edges of the domain. However, the extrados position is generally unpopulated by the rays.

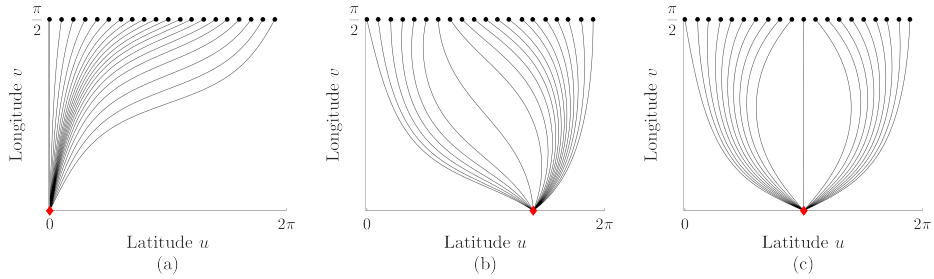


Figure 21: The ray paths that cross on a pipe bend when the intrados (a), top (b), and extrados (c) are excited. The grouping of the ray paths is evident towards the edges of the domain (intrados) (from Publication II).

To further understand the effectiveness of FWI in replicating the thickness map of a pipe bend, particularly when Hann-shaped defects situated at varying circumferential positions are present, a detailed numerical analysis was carried out. For all cases, the defect width remained constant at 120 mm, while the depth varied between 10 and 50 percent of the wall thickness. The defect was positioned at seven different circumferential locations, labeled as α : 0° , 30° , 60° , 90° , 120° , 150° , and 180° . Figure 22 shows the three primary defect positions: extrados (a), top (b), and intrados (c). Figure 22(c) depicts the transducer distribution used for both the numerical and experimental studies. More information about the Hann-shaped defect characterization is featured in Section 3.2.3.

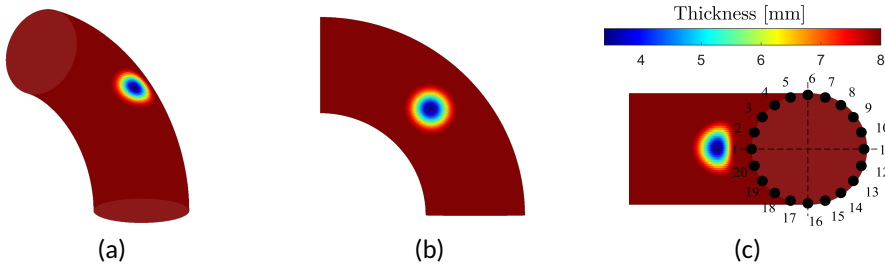


Figure 22: Hann-shaped defect with 50% of thickness reduction located at 0° (a), 90° (b), and 180° (c) (from Publication III).

The evaluation of the reconstructed maps of wall-thickness loss was done quantitatively, using the *mean magnitude of relative error* (MMRE) of the residuals between the actual defect T and the replicated wall-thickness maps Γ . The MMRE signifies the average

of the ratios of the absolute difference between two values to the magnitude of the actual value [72]. For a total of n ratios, the following equation is used:

$$MMRE = \frac{1}{n} \sum_{i=1}^n \frac{|T_i - \Gamma_i|}{T_i}. \quad (23)$$

Figure 23(a) presents the relationship between the reconstructed maximum depth and the nominal defect depth, adjusting with the defect's position across the pipe's circumference. Depth is given as a percentage of the nominal wall thickness. Meanwhile, Figure 23(b) displays the variation of the MMRE with respect to the depth and position of the defect around the circumference. Figure 23(a) clearly shows the maximum depth of

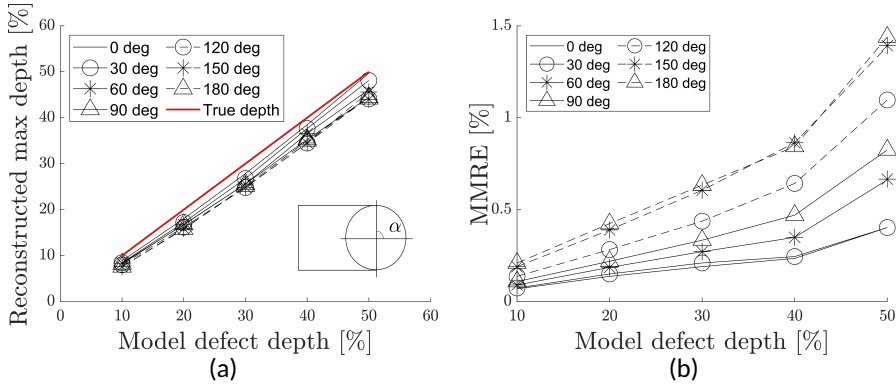


Figure 23: (a) illustrates the reconstructed maximum thickness maps regarding defect depth and position around the pipe circumference, while (b) displays the relative mean error for each case (from **Publication III**).

reconstruction accuracy exhibiting a linear trend for each circumferential position. Moreover, Figure 23(b) demonstrates that the MMRE is circumferential-position dependent, becoming more precise as the defect moves towards the center of the 2-D domain. This trend can be linked to the limited view angles [73].

Relative to GWT based on Time of Flight (TOF) for a pipe bend [41, 74], a typical pair of transducers is sufficient for FWI to accurately locate the defect, regardless of its circumferential position. Moreover, FWI efficiently exploits the focusing effect [25], thus leading to a more precise reconstruction when the defect is close to the extrados, as illustrated in Figure 23(b). In contrast, TOF methods tend to bypass the extrados positions in the bend due to the focusing effect [25], limiting the coverage of view angles. Consequently, Brath et al. [43] suggested an additional array of transducers along the extrados position to enhance detection capabilities at the expense of increasing the technical complexity for practical applications.

4.2.2 Experimental Validation

The pipe bend specimen, as described in Section 3.1, underwent a controlled reduction in thickness achieved by employing an angle grinder, a versatile tool often used for material removal. This operation followed a plan designed to create a defect with specific dimensions of a 100 mm diameter and a thickness reduction of 47%. This manipulation is visually depicted in Figure 24(a).

The coordinates of the defect's center align with $[0, \pi/2]$, which depict the circumferential and azimuth coordinates, respectively. This position represents the extrados loca-

tion, an exterior curve in architecture or mechanics where stress or tension generally concentrates. Post-creation of the defect, the remaining surface area was carefully measured using Creaform’s ACADEMIA 50 scanner, as cited in [75]. This advanced scanner utilizes structured white light technology, projecting structured light onto the object under study and capturing the deformations of this light pattern using high-resolution cameras.

Following this process, the resulting data was then manipulated and processed to construct a highly detailed 3-D prototype of the pipe bend, which provides a comprehensive visual aid. The remaining wall-thickness map was further interpolated to fit within the elastic model as described in Section 3.2 of the pipe bend. In clearer depiction, Figure 24(b) visually represents the remaining thickness of the pipe bend after the intentional creation of the defect. Furthermore, the measured remaining thickness was interpolated again to adjust the mesh size of the FE model, reinforcing the specificity of the study. This methodology retains the integrity of the FE model while allowing for the incorporation of the measured data.

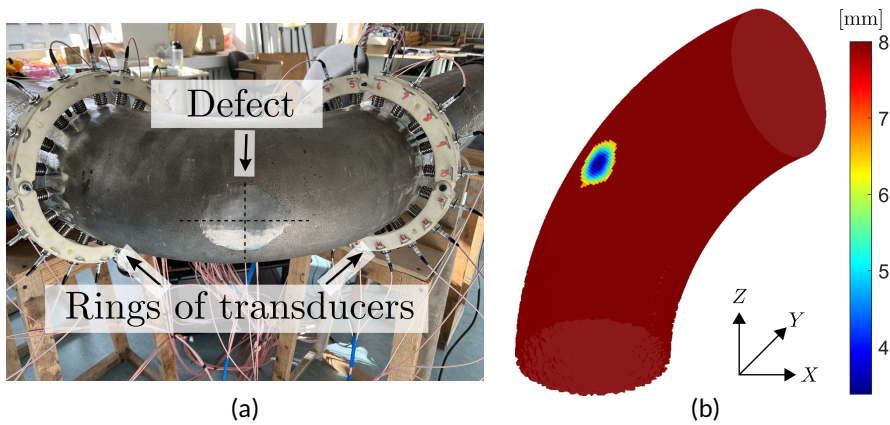


Figure 24: Thickness reduction on a steel pipe bend (a) and its remaining thickness (b) (from **Publication III**).

The transmission of the A_0 mode was measured from each transducer to the opposing ring, with 400 signals per transducer ring being recorded. A similar process was applied to the FE model. From the recorded wavefields, the first wave packets for both the elastic model and the experimental environment were extracted. These procedures were previously detailed in Section 4.1.2. Before the inversion process, an autocalibration method, as outlined in Section 3.3.4, was adopted to calibrate the elastic model and the measured wavefields. The inversion scheme utilized only three replicas. However, the process of the separation algorithm resulted in some loss of data from the transducers proximate to the edges of the domain due to applied smoothing.

The reconstruction of the actual defect and its monochromatic representation are displayed in Figure 25 at 50 kHz. This resulted from 40 iterations applied uniformly to the elastic model and the experiment, giving a 2-D interpretation. Profiles along the circumferential and azimuthal directions are depicted in Figure 26, providing a deeper understanding of the thickness map’s construction process. High-level artifacts were discarded to maintain simplicity. The elastic model output, visible in Figure 25(b), yielded an exceptionally clear and accurate image. Despite minor artifacts, the quality of the defect’s inner region remained unblemished. This outcome aligns with the expected 0.4% MMRE from the previously mentioned maximum thickness map study in Figure 23(b). A noteworthy

thy presence of artifacts was observed in the images reconstructed from the experimental readings, exemplified in Figure 25(c). The defect's length was considerably underestimated in the circumferential direction, as portrayed in Figure 26(a). A close agreement was achieved in the azimuthal direction, as shown in Figure 26(b), yielding an MMRE of 0.7%.

The anisotropy factor of the wave field introduces a significant challenge, even when using similar transducers for measurements. This leads to inaccuracies in the circumferential direction and the substantial presence of artifacts because of the normalized scattered signals in the autocalibration stage. Additionally, the inversion process produces more errors when the mismatch between observed and synthesized signals increases [66].

Furthermore, the reliability of the experimental results can be affected by several factors, including tolerances in manufacturing the bend, the positioning of the transducers, noise, the performance of the transducer, flaws in the helical path algorithm, and coupling.

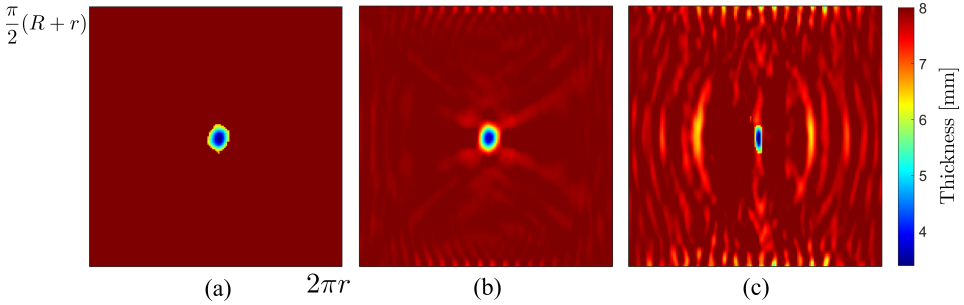


Figure 25: Remaining thickness (a) and reconstructed thickness by FWI from elastic modeling (b) and experimental measurements (c) (from Publication III).

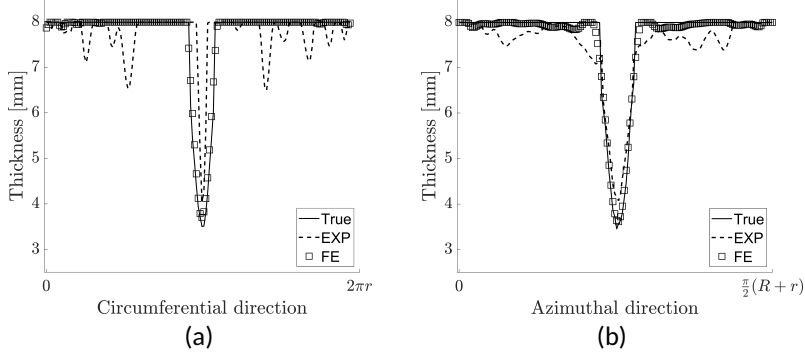


Figure 26: Axial thickness profiles along the circumferential (a) and the azimuthal direction (b) (from Publication III).

In summary, this study demonstrates the effectiveness of FWI in accurately reconstructing defects in pipe bends, regardless of their circumferential position. This is in contrast to TOF approaches, which have limitations in covering certain angles. The research suggests that further accuracy in FWI can be achieved through various methods such as increasing the number of replicas or implementing different types of regularization [76, 77].

However, the experimental data showed significant artifacts and an underestimation of the defect length in the circumferential direction, with an MMRE of 0.7%. **Publication III** delves into the impact of the experimental uncertainties caused by the transducers.

5 Discussion and Concluding Remarks

The research conducted in this thesis presents a comprehensive methodology and a practical demonstration for computing full waveform inversion. This computation is based on the propagation of guided waves specifically for pipe bends, a topic of significant interest in the field.

The successful implementation of this methodology hinges on three key components. Firstly, an accurate 2-D acoustic model is required. This model is made artificially anisotropic by the application of the Thomsen parameter, a well-regarded approach in the field. Secondly, signal processing techniques are employed, including the separation of helical paths and data calibration. These techniques ensure the accuracy and reliability of the results obtained. Lastly, the methodology involves purging experimental uncertainties. This step is crucial to ensure the validity of the results and to minimize potential errors.

The results obtained from this research were validated both numerically and experimentally. The detailed descriptions of these results have been published in various research publications, contributing to the body of knowledge in this field. In addition, the methods and studies used in this research have not been performed before in such detail, making this thesis unique. This level of detail provides a deeper understanding of the subject matter and contributes to its advancement.

5.1 Summary of results

In **Publication I** an efficient and straightforward forward model was developed to simulate the propagation and scattering of guided waves in pipe bends. The 3-D elastic bend was replaced by a 2-D rectangular anisotropic acoustic domain using orthogonal parametrization. The equivalence in wave propagation was established by implementing approximate anisotropic Thomsen parameters that describe the angular variability of the velocity in the acoustic model. The A_0 mode propagation and interaction with defects from different excitation points across the bend were simulated using the model. The focusing effect was observed, and a good agreement was found between the results from the proposed modeling, the FE modeling, and the experimental results.

The journey towards full waveform inversion commenced with the 2-D modeling of the complex wavefield of the bend. To accommodate the cyclic nature of the wave field, the subsequent step involved the extraction of the first arrived wave packets. This process essentially unwraps the 3-D wavefield by incorporating additional replicas into the 2-D domain.

Existing algorithms for helical path separation are predominantly dependent on a single key variable: the distance traversed by the ray-paths. Consequently, in **Publication II**, a novel method was introduced to compute the distances traveled from the source to the receivers in a pipe bend. The proposed shortest-path algorithm was rooted in the geodesic equations of a torus. This approach, when juxtaposed with traditional ray-tracing and grid-based methods, offers a more straightforward means of determining the particle trajectory in a bend, necessitating only information about the bend geometry. Moreover, the computation of geodesics can enhance our understanding of the guided wave propagation in the bend, provide estimates of the arrival times to the receivers, and even trace helical paths.

The final step towards achieving full waveform inversion entailed the re-scaling of the experimental data. This was done to align it with the acoustic model, a crucial step that served to minimize artifacts and enhance accuracy. **Publication IV** provides an in-depth exploration of the pre-conditioning process, which involved normalizing the scattered wave-

fields by the mean of the non-scattered ones.

An updated auto-calibration method was introduced to address the critical issue of amplitude variations among the transducers. This step is vital because the inversion scheme relies on a least square function, which assumes that data errors follow a Gaussian distribution. In simpler terms, this means the errors are expected to form a bell-shaped curve, where most values cluster around the average, and extreme deviations become increasingly rare as they move further from the mean. Ignoring this assumption can cause the inversion process to get stuck in a local minimum, leading to inaccurate results. Therefore, careful calibration and meticulous data handling are essential to ensure the accuracy and reliability of the results.

Numerical and experimental validation was conducted on a carbon steel pipe bend with specific dimensions and characteristics. Despite a minor underestimation of the maximum depth, the detection of thickness loss was successfully achieved, irrespective of the damage position around the bend. FWI exhibited its proficiency in mapping a defect independently of its circumferential location, thereby outperforming travel-time-based tomographic methods. The experimental validation slightly deviated from the real thickness map due to pronounced inhomogeneous transducer performance. Nevertheless, the robustness of the autocalibration method in anisotropic media was demonstrated when reconstructing the defect from elastic modeling data, resulting in a maximum reconstructed thickness error of a mere 0.7%.

5.2 Key Conclusions Presented for Defense

- An efficient and simple acoustic forward model was developed to simulate guided wave propagation and scattering in pipe bends. The 3D elastic bend was replaced by a 2D rectangular anisotropic acoustic domain using orthogonal parameterization, and the equivalence in wave propagation was established by anisotropic Thomsen parameters.
- The 2-D acoustic wavefield was demonstrated to capture the focusing effect, as a result of the elliptical anisotropy condition imposed by the curvature of the bend.
- The cyclic nature of the bend was represented in the 2-D domain by adding an extra number of replicas.
- The traveled distance of the wave packets is the key variable for the successful implementation of the robust helical path separation algorithm.
- The geodesic equations helped to determine the ray-path trajectories in the bend, estimate times of arrival, and understand the focusing effect, relying only on the geometrical properties rather than on the wavefield.
- Preconditioning of the input data for FWI is of paramount importance in order to reduce artifacts in the image reconstruction.
- Strong amplitude variations from experimental uncertainties and poor transducer performance caused the inversion algorithm to get trapped in a local minimum. Therefore, attention should be paid to rescale the amplitudes if needed.

5.3 Perspectives of Future Work

Future work can explore into more detail various aspects of this thesis, including:

- Full Waveform Inversion can be extended to other parametric surfaces, such as the paraboloid or saddle point. This can be achieved by using an appropriate orthogonal parametrization and exploring the right Thomsen parameters for their respective wavefields. This extension allows FWI to be applied in a wider range of scenarios, enhancing its versatility and applicability in structures.
- Based on the shortest-path algorithm, the application of time-reversal based methods would be possible for more complicated geometries. This not only broadens the scope of geometries that can be analyzed but also provides some insight into the characteristics of their wavefields. Understanding these characteristics can lead to more accurate predictions and analyses, contributing to the overall effectiveness of the method.
- More accurate image reconstructions can be achieved by means of energy compensation of the experimental data or pre-conditioning of the input data, via digital filters (e.g., Kalman filters) or machine learning techniques. These methods can help to mitigate the effects of noise and other distortions in the data, leading to clearer and more accurate reconstructions. In the case of machine learning, advanced algorithms can be trained to recognize and correct for specific types of distortions, further enhancing the quality of the reconstructions.

List of Figures

1	A guided wave tomography set-up (a) , integrated by two rings of transducers, and dispersion curves of fundamental Lamb wave modes for an 8 mm steel plate (b) (from Publication II).....	15
2	Flowchart of the GWT algorithm: real data (measured signals) and synthetic data (from forward model) are compared iteratively until a given residual criteria is reached. The role of the forward model is highlighted (from Publication I).	15
3	Ray paths traveling in a 2-D representation of a straight pipe (a) and a pipe bend (b) with an arbitrary defect (from Publications III and IV).	17
4	A torus section, representing the bend of the pipe, is translated from (a) , the 3-D space domain Σ to (b) , the 2-D space domain Ω (from Publication I).	18
5	(a) Acoustic representation of GW propagation in a vertically transversely isotropic plate. (b) top perspective of the wave-field, tilt angle θ , wave number \bar{k} , and phase angle ϕ (from Publication I).	19
6	Flow diagram depicting the full-waveform inversion algorithm. The inverse problem is designed to incrementally minimize the sum of squared residuals (from Publication III).	21
7	Illustration of the pipe bend. (a) Aerial view, (b) Side view, and (c) Perspective view of the conceptualized pipe bend (from Publication I).	22
8	Configuration of the pipe simulated in ABAQUS, exhibiting a Hann-shaped defect, absorbing areas 1 and 2, and propagating wave displacements at 100 μs (from Publication I).	23
9	Figure (a) shows ε and δ distribution along the bend with 3 replicas. Sources are positioned at the central replica. Figure (b) shows background phase velocity v_0 at 50 kHz (from Publication III).....	24
10	Thickness T (mm) in the 2-D acoustic domain with a Hann-shaped defect at three different locations: (a) <i>extrados</i> , (b) <i>top</i> , and (c) <i>intrados</i> (from Publication I).	25
11	Excited chirp function $s_c(t)$ and desired tone burst modulated with a Hanning window and a central frequency of 44 kHz and 5 cycles $s_d(t)$ in (a) . Transmitted chirp response $r_c(t)$ in the pipe bend specimen from Figure 7 when exciting at the intrados position (b) and the extracted response $r_d(t)$ (c)	25
12	Helical Path Separation Algorithm.....	26
13	In (a) , the direct route between points A and B is the straight line $f_{AB}(t)$, where $f''_{AB}(t) = 0$. In (b) , on the arbitrary surface S defined by vertices A, B , and C , the geodesic $\varphi_{AB'}(t)$ represents the shortest path between A and B' , with $\varphi''_{AB'} = 0$. In (c) , the torus section S illustrates the bend of a pipe in the 3D domain (from Publication II).	27
14	Shortest paths from three distinct starting points: intrados (a) , top (b) , and extrados (c) ; along with 20 evenly spaced monitoring points around the torus latitude (from Publication II).....	28
15	All the rays used in order to calibrate $D_{r,s}$ (a) , and calibration factors $Q_{r,s}$ plotted in the complex plain (b) (from Publication IV).	30

16	(a) Steel pipe bend specimen with characteristics consistent with Table 1. Measurement setup showing transducer arrays (A) and (B), each with 20 transducers and an acquisition system; (b) Pipe bend with an artificial defect made from plasticine located on the intrados, viewed from the <i>intrados</i> (from Publication I).	31
17	Time-of-flight (TOF) and logarithmic root mean square amplitudes from forward modeling and experimental measurements. TOFs from the intrados (a), top (b), and extrados (c), along with their respective amplitude variations (d)-(f) (from Publication III).	32
18	A histogram of the 120 resonance frequencies is shown in (a), while (b) presents the impedance resistance as a function of frequency. In (b), the dashed lines indicate the most reliable operating interval for the transducers, and the solid lines encompass the transducers within a 75% confidence interval (from Publication IV).	32
19	Experimental, FE, and FD contour plots of the normalized radial displacement in the bend for three excitation positions: extrados, top, and intrados. The A_0 mode was triggered with a central frequency of 50 kHz (from Publication I).	34
20	Experimental wave fields are presented. The A_0 mode was stimulated with a central frequency of 50 kHz. The measured wave fields, replicated 5 times, were excited at the intrados (a), top (b), and extrados (c). The wave fields extracted after the helical path separation are shown in (d)-(f). Following the helical path separation, the noise from the crosstalk is windowed, and the focusing effect remains intact (from Publication II).	35
21	The ray paths that cross on a pipe bend when the intrados (a), top (b), and extrados (c) are excited. The grouping of the ray paths is evident towards the edges of the domain (intrados) (from Publication II).	36
22	Hann-shaped defect with 50% of thickness reduction located at 0° (a), 90° (b), and 180° (c) (from Publication III).	36
23	(a) illustrates the reconstructed maximum thickness maps regarding defect depth and position around the pipe circumference, while (b) displays the relative mean error for each case (from Publication III).	37
24	Thickness reduction on a steel pipe bend (a) and its remaining thickness (b) (from Publication III).	38
25	Remaining thickness (a) and reconstructed thickness by FWI from elastic modeling (b) and experimental measurements (c) (from Publication III).	39
26	Axial thickness profiles along the circumferential (a) and the azimuthal direction (b) (from Publication III).	39

List of Tables

1	Material attributes of the steel pipe: Density ρ , Young's modulus E_m , and Poisson ratio ν	22
---	---	----

References

- [1] Takahiro Hayashi, Koichiro Kawashima, Zongqi Sun, and Joseph L. Rose. Guided wave propagation mechanics across a pipe elbow. *Journal of Pressure Vessel Technology*, 127(3):322–327, January 2005.
- [2] M. Talebi, M. Zeinoddini, M. Mo'tamedi, and A.P. Zandi. Collapse of hsla steel pipes under corrosion exposure and uniaxial inelastic cycling. *Journal of Constructional Steel Research*, 144:253–269, 2018.
- [3] Stylianos Livadiotis, Arvin Ebrahimkhanlou, and Salvatore Salamone. Monitoring internal corrosion in steel pipelines: a two-step helical guided wave approach for localization and quantification. *Structural Health Monitoring*, 20(5):2694–2707, nov 2020.
- [4] Beata Zima and Rafał Kedra. Detection and size estimation of crack in plate based on guided wave propagation. *Mechanical Systems and Signal Processing*, 142:106788, aug 2020.
- [5] Zhenxing Yan, Lida Wang, Piji Zhang, Wen Sun, Zhengqing Yang, Bingyan Liu, Jisheng Tian, Xiangquan Shu, Yongpeng He, and Guichang Liu. Failure analysis of erosion-corrosion of the bend pipe at sewage stripping units. *Engineering Failure Analysis*, 129:105675, 2021.
- [6] Jing Rao, Madis Ratssepp, and Zheng Fan. Guided wave tomography based on full waveform inversion. *IEEE Transactions on Ultrasonics, Ferroelectrics, and Frequency Control*, 63(5):737–745, May 2016.
- [7] Tom Druet, Huu Hoang, Bastien Chapuis, and Emmanuel Moulin. Passive guided wave tomography for pipes inspection. In *QNDE2019 - 46th Annual Review of Progress in Quantitative NondestructiveEvaluation*, Portland, United States, July 2019.
- [8] Leak blamed as Mexico explosion death toll rises. <https://www.theguardian.com/world/2016/apr/22/leak-blamed-as-mexico-explosion-death-toll-rises>. (Accessed on 2021-06-30).
- [9] B. G. N. Muthanna, Mouna A., M. H. Meliani, B. Mettai, Z. B., R. Suleiman, and A. Sorour. Inspection of internal erosion-corrosion of elbow pipe in the desalination station. *Engineering Failure Analysis*, 102:293–302, 2019.
- [10] Kusmono and Khasani. Analysis of a failed pipe elbow in geothermal production facility. *Case Studies in Engineering Failure Analysis*, 9:71–77, 2017.
- [11] Carol A. Lebowitz and Lawrence M. Brown. *Review of Progress in Quantitative Non-destructive Evaluation*, chapter Ultrasonic Measurement of Pipe Thickness, pages 1987–1994. Springer US, Boston, MA, 1993.
- [12] Sandeep Kumar Dwivedi, Manish Vishwakarma, and Prof. Akhilesh Soni. Advances and Researches on Non Destructive Testing: A Review. *Materials Today: Proceedings*, 5(2, Part 1):3690–3698, January 2018.

- [13] Devesh Mishra, Krishna Kant Agrawal, Ali Abbas, Rekha Srivastava, and R. S. Yadav. PIG [Pipe Inspection Gauge]: An Artificial Dustman for Cross Country Pipelines. *Procedia Computer Science*, 152:333–340, January 2019.
- [14] Mira Mitra and S. Gopalakrishnan. Guided wave based structural health monitoring: A review. *Smart Materials and Structures*, 25(5):053001, March 2016.
- [15] Ruiqi Guan, Ye Lu, Wenhui Duan, and Xiaoming Wang. Guided waves for damage identification in pipeline structures: A review. *Structural Control and Health Monitoring*, 24(11):e2007, 2017.
- [16] Zhongqing Su, Lin Ye, and Ye Lu. Guided lamb waves for identification of damage in composite structures: A review. *Journal of Sound and Vibration*, 295(3-5):753–780, August 2006.
- [17] David Alleyne and Peter Cawley. Long range propagation of lamb waves in chemical plant pipework. *Materials evaluation*, 55:504–508, 1997.
- [18] Aidin Ghavamian, Faizal Mustapha, B.T Baharudin, and Noorfaizal Yidris. Detection, localisation and assessment of defects in pipes using guided wave techniques: A review. *Sensors*, 18(12):4470, December 2018.
- [19] Thomas Vogt, Sebastian Heinlein, Josh Milewczyk, Stefano Mariani, Robin Jones, and Peter Cawley. Guided wave monitoring of industrial pipework – improved sensitivity system and field experience. In Piervincenzo Rizzo and Alberto Milazzo, editors, *European Workshop on Structural Health Monitoring*, pages 819–829, Cham, 2021. Springer International Publishing.
- [20] P. S. Lowe, R. Sanderson, S. K. Pedram, N. V. Boulgouris, and P. Mudge. Inspection of Pipelines Using the First Longitudinal Guided Wave Mode. *Physics Procedia*, 70:338–342, January 2015.
- [21] Shi Yan, Bowen Zhang, Gangbing Song, and Jiaoyun Lin. PZT-based ultrasonic guided wave frequency dispersion characteristics of tubular structures for different interfacial boundaries. *Sensors*, 18(12):4111, November 2018.
- [22] Zhenhua Song, Xiangshang Qi, Zenghua Liu, and Hongwei Ma. Experimental study of guided wave propagation and damage detection in large diameter pipe filled by different fluids. *NDT & E International*, 93:78–85, January 2018.
- [23] Samuel Chukwuemeka Olisa, Muhammad A. Khan, and Andrew Starr. Review of current guided wave ultrasonic testing (GWUT) limitations and future directions. *Sensors*, 21(3):811, January 2021.
- [24] Sebastian Heinlein, Peter Cawley, and Thomas Vogt. Validation of a procedure for the evaluation of the performance of an installed structural health monitoring system. *Structural Health Monitoring*, 18(5-6):1557–1568, 2019.
- [25] Joseph L. Rose, Li Zhang, Michael J. Avioli, and Peter J. Mudge. A natural focusing low frequency guided wave experiment for the detection of defects beyond elbows. *Journal of Pressure Vessel Technology*, 127(3):310–316, February 2005.
- [26] A. Demma, P. Cawley, M. Lowe, and B. Pavlakovic. The effect of bends on the propagation of guided waves in pipes. *Journal of Pressure Vessel Technology*, 127(3):328–335, February 2005.

- [27] Kevin E. Rudd, Kevin R. Leonard, Jill P. Bingham, and Mark K. Hinders. Simulation of guided waves in complex piping geometries using the elastodynamic finite integration technique. *The Journal of the Acoustical Society of America*, 121(3):1449–1458, March 2007.
- [28] S. Heinlein, P. Cawley, and T.K. Vogt. Reflection of torsional T(0,1) guided waves from defects in pipe bends. *NDT & E International*, 93:57–63, January 2018.
- [29] Zhao-Dong Xu, Chen Zhu, and Ling-Wei Shao. Damage identification of pipeline based on ultrasonic guided wave and wavelet denoising. *Journal of Pipeline Systems Engineering and Practice*, 12(4):04021051, 2021.
- [30] D.P. Jansen and D.A. Hutchins. Lamb wave tomography. In *IEEE Symposium on Ultrasonics*, pages 1017–1020 vol.2, 1990.
- [31] P. Huthwaite. Evaluation of inversion approaches for guided wave thickness mapping. *Proceedings of the Royal Society A: Mathematical, Physical and Engineering Sciences*, 470(2166):20140063, June 2014.
- [32] A. H. Rohde, M. Veidt, L. R. F. Rose, and J. Homer. A computer simulation study of imaging flexural inhomogeneities using plate-wave diffraction tomography. *Ultrasonics*, 48(1):6–15, March 2008.
- [33] Peter Huthwaite and Francesco Simonetti. High-resolution guided wave tomography. *Wave Motion*, 50(5):979–993, 2013.
- [34] Min Lin, Caleb Wilkins, Jing Rao, Zheng Fan, and Yang Liu. Corrosion detection with ray-based and full-waveform guided wave tomography. In Tzu-Yang Yu, editor, *Non-destructive Characterization and Monitoring of Advanced Materials, Aerospace, Civil Infrastructure, and Transportation XIV*, volume 11380, pages 102 – 109. International Society for Optics and Photonics, SPIE, 2020.
- [35] Arno Volker, Arjan Mast, and Joost Bloom. Experimental results of guided wave travel time tomography. *AIP Conference Proceedings*, 1211(1):2052–2059, 2010.
- [36] C. L. Willey, F. Simonetti, P. B. Nagy, and G. Instanes. Guided wave tomography of pipes with high-order helical modes. *NDT and E International*, 65:8 – 21, 2014.
- [37] Peter Huthwaite, Remo Ribichini, Peter Cawley, and Michael J.S. Lowe. Mode selection for corrosion detection in pipes and vessels via guided wave tomography. *IEEE Transactions on Ultrasonics, Ferroelectrics, and Frequency Control*, 60(6):1165–1177, 2013.
- [38] Arno Volker and Tim van Zon. Guided wave travel time tomography for bends. AIP, 2013.
- [39] R. M. Sanderson, D. A. Hutchins, D. R. Billson, and P. J. Mudge. The investigation of guided wave propagation around a pipe bend using an analytical modeling approach. *The Journal of the Acoustical Society of America*, 133(3):1404–1414, mar 2013.
- [40] Alex J. Brath, Francesco Simonetti, Peter B. Nagy, and Geir Instanes. Acoustic formulation of elastic guided wave propagation and scattering in curved tubular structures. *IEEE Transactions on Ultrasonics, Ferroelectrics, and Frequency Control*, 61(5):815–829, 2014.

- [41] Alex J. Brath, Francesco Simonetti, Peter B. Nagy, and Geir Instanes. Guided wave tomography of pipe bends. *IEEE Transactions on Ultrasonics, Ferroelectrics, and Frequency Control*, 64(5):847–858, may 2017.
- [42] Yu Wang and Xueyi Li. Elbow damage identification technique based on sparse inversion image reconstruction. *Materials*, 13(7), 2020.
- [43] Alex J. Brath, Francesco Simonetti, Peter B. Nagy, and Geir Instanes. Experimental validation of a fast forward model for guided wave tomography of pipe elbows. *IEEE Transactions on Ultrasonics, Ferroelectrics, and Frequency Control*, 64(5):859–871, May 2017.
- [44] Jing Rao, Madis Ratssepp, and Zheng Fan. Investigation of the reconstruction accuracy of guided wave tomography using full waveform inversion. *Journal of Sound and Vibration*, 400:317–328, July 2017.
- [45] Carlos-Omar Rasgado-Moreno, Marek Rist, Raul Land, and Madis Ratssepp. Acoustic Forward Model for Guided Wave Propagation and Scattering in a Pipe Bend. *Sensors*, 22(2):486, January 2022.
- [46] Tariq Alkhalifah. An acoustic wave equation for anisotropic media. *GEOPHYSICS*, 65(4):1239–1250, July 2000.
- [47] Hongbo Zhou, Guanquan Zhang, and Robert Bloor. An anisotropic acoustic wave equation for modeling and migration in 2d TTI media. In *SEG Technical Program Expanded Abstracts 2006*. Society of Exploration Geophysicists, jan 2006.
- [48] L. Thomsen. Weak elastic anisotropy. *GEOPHYSICS*, 50(10):1954–1966, October 1986.
- [49] Madis Ratssepp, Jing Rao, Xudong Yu, and Zheng Fan. Modeling the effect of anisotropy in ultrasonic guided wave tomography. *IEEE Transactions on Ultrasonics, Ferroelectrics, and Frequency Control*, pages 1–1, 2021.
- [50] Ludovic Métivier and Romain Brossier. The seiscscope optimization toolbox: A large-scale nonlinear optimization library based on reverse communication. *GEOPHYSICS*, 81(2):F1–F15, 2016.
- [51] *ABAQUS/Standard User's Manual, Version 6.14*. Dassault Systèmes Simulia Corp, United States.
- [52] M. Drozd, L. Moreau, M. Castaings, M. J. S. Lowe, and P. Cawley. Efficient Numerical Modelling of Absorbing Regions for Boundaries Of Guided Waves Problems. *AIP Conference Proceedings*, 820(1):126–133, March 2006.
- [53] Stéphane Operto, Jean Virieux, A. Ribodetti, and J. E. Anderson. Finite-difference frequency-domain modeling of viscoacoustic wave propagation in 2d tilted transversely isotropic (TTI) media. *GEOPHYSICS*, 74(5):T75–T95, September 2009.
- [54] Jennifer E. Michaels, Sang Jun Lee, Anthony J. Croxford, and Paul D. Wilcox. Chirp excitation of ultrasonic guided waves. *Ultrasonics*, 53(1):265–270, January 2013.
- [55] Peter Huthwaite and Matthias Seher. Robust helical path separation for thickness mapping of pipes by guided wave tomography. *IEEE Transactions on Ultrasonics, Ferroelectrics, and Frequency Control*, 62(5):927–938, May 2015.

- [56] R.L. Lucena and J.M.C. Dos Santos. Structural health monitoring using time reversal and cracked rod spectral element. *Mechanical Systems and Signal Processing*, 79:86–98, oct 2016.
- [57] Ryan Watkins and Ratneshwar Jha. A modified time reversal method for lamb wave based diagnostics of composite structures. *Mechanical Systems and Signal Processing*, 31:345–354, aug 2012.
- [58] Zhi Qian, Chenchen Zhang, Peng Li, Bin Wang, Zhenghua Qian, Iren Kuznetsova, and Xiangyu Li. A dictionary-reconstruction approach for separating helical-guided waves in cylindrical pipes. *Journal of Physics D: Applied Physics*, 56(30):305301, May 2023.
- [59] Barrett O'Neill. *Elementary Differential Geometry*. Elsevier Science Publishing Co Inc, 2 edition, May 2006.
- [60] A. N. Pressley. *Elementary Differential Geometry*. Springer London, March 2010.
- [61] Vladimir Rovenski. *Modeling of Curves and Surfaces with MATLAB®*. Springer New York, 2010.
- [62] F. Simonetti and M.Y. Alqaradawi. Guided ultrasonic wave tomography of a pipe bend exposed to environmental conditions: A long-term monitoring experiment. *NDT & E International*, 105:1 – 10, 2019.
- [63] Jiawei Wen, Can Jiang, Yubing Li, Hao Chen, Weiwei Ma, and Jian Wang. An Auto-Calibration Algorithm for Hybrid Guided Wave Tomography Based on Full Waveform Inversion. *IEEE Access*, 11:62496–62509, 2023.
- [64] Tom Druet, Jean-Loup Tastet, Bastien Chapuis, and Emmanuel Moulin. Autocalibration method for guided wave tomography with undersampled data. *Wave Motion*, 89:265–283, June 2019.
- [65] Zhikai Wang, Satish C Singh, and Mark Noble. True-amplitude versus trace-normalized full waveform inversion. *Geophysical Journal International*, 220(2):1421–1435, February 2020.
- [66] A. J. Brenders and R. G. Pratt. Full waveform tomography for lithospheric imaging: results from a blind test in a realistic crustal model. *Geophysical Journal International*, 168(1):133–151, January 2007.
- [67] Digilent. Using the oscilloscope - diligent reference, 2019. Accessed: 2024-04-24.
- [68] Xiaoxiao Dong, Tao Yuan, Minqiang Hu, Husain Shekhani, Yuichi Maida, Tonshaku Tou, and Kenji Uchino. Driving frequency optimization of a piezoelectric transducer and the power supply development. *Review of Scientific Instruments*, 87(10), October 2016.
- [69] Zhe Wang, Songling Huang, Gongtian Shen, Shen Wang, and Wei Zhao. High resolution tomography of pipeline using multi-helical lamb wave based on compressed sensing. *Construction and Building Materials*, 317:125628, jan 2022.
- [70] Yanping Zhu, Yue Hu, Fucai Li, Saqlain Abbas, Wenjie Bao, and Wensheng Su. Internal damage localization for large-scale hollow cylinders based on helical sensor network. *Structural Health Monitoring*, page 147592172211245, sep 2022.

- [71] A. Golato, F. Ahmad, S. Santhanam, and M. G. Amin. Multi-Helical Path Exploitation in Sparsity-Based Guided-Wave Imaging of Defects in Pipes. *Journal of Nondestructive Evaluation*, 37(2):27, March 2018.
- [72] Magne Jørgensen, Torleif Halkjelsvik, and Knut Liestøl. When should we (not) use the mean magnitude of relative error (MMRE) as an error measure in software development effort estimation? *Information and Software Technology*, 143:106784, March 2022.
- [73] Peter Huthwaite, Alicia A. Zwiebel, and Francesco Simonetti. A new regularization technique for limited-view sound-speed imaging. *IEEE Transactions on Ultrasonics, Ferroelectrics, and Frequency Control*, 60(3):603–613, March 2013.
- [74] Yu Wang and Xueyi Li. Elbow Damage Identification Technique Based on Sparse Inversion Image Reconstruction. *Materials*, 13(7):1786, January 2020.
- [75] Creaform. Academia 50 3d scanner, 2019. Accessed: 2024-04-09.
- [76] A. Tikhonov and V. Arsenin. Solution of incorrectly formulated problems and the regularization method. *Sov. Math. Dokl.*, 4:1035 – 1038, 1963. Cited by: 48.
- [77] Jing Rao, Madis Ratssepp, and Zheng Fan. Limited-view ultrasonic guided wave tomography using an adaptive regularization method. *Journal of Applied Physics*, 120(19):194902, November 2016.

Acknowledgements

Completing this PhD thesis has been a journey filled with challenges, growth, and gratitude. I would like to take this opportunity to acknowledge the people and institutions whose support and guidance have made this achievement possible.

First and foremost, I wish to express my deepest gratitude to my grandparents. Their hardworking lives laid the foundation for my parents to pursue university degrees, a legacy of perseverance and education that has inspired me throughout my life.

To my parents, I owe everything. Your unwavering support, encouragement, and belief in me have been my greatest strengths. It is because of you that I am where I am today.

I would also like to thank the rest of my family for their care and vigilance, especially during my time living abroad. Your constant concern and love have been a comforting anchor during this journey.

To my friends, thank you for walking with me through the ups and downs of this journey. Your companionship and encouragement have made all the difference.

To my colleagues, project leaders and supervisors from the GW4SHM project. This would not have been possible without your vision, mentor-ship and support.

I am profoundly grateful to Madis and the many colleagues who have provided me with invaluable advice and guidance along the way. Your insights and expertise have greatly shaped this work.

I would also like to extend my heartfelt thanks to my former professors from the University of Veracruz. Your mentorship, advice, and guidance played a crucial role in shaping my academic path. Most importantly, you nourished my love for mathematics and research, which has been the foundation of my passion for this work.

My sincere thanks go to the European Union (Horizon 2020) and the Estonian government for their generous funding. Without their support, this project would not have been possible. I am also immensely thankful to the Study in Estonia program for giving me the opportunity to share my love for this remarkable country.

Finally, I wish to extend my heartfelt thanks to Ene, who has been the cornerstone of everything during this past year. The engineering department runs smoothly thanks to your dedication and efforts, and I am deeply grateful for all you have done.

Abstract

Developing Guided Wave Tomography for a Pipe Bend

Pipeline systems, particularly pipe bends, are critical components in industrial infrastructure. Traditional Non-destructive methods, such as ultrasonic thickness measurements, are labor-intensive and may not provide a comprehensive assessment of the pipe's condition. The unique challenges faced by pipe bends, including higher stress levels due to changes in fluid direction, make them particularly vulnerable to fatigue, corrosion, and cracking. Therefore, there is a critical need for advanced techniques that can provide a more holistic and efficient solution for monitoring these components. As a result, this thesis explores the application of Guided Wave Tomography (GWT) based on Full Waveform Inversion (FWI) for the high-resolution reconstruction of pipe bend thickness, addressing the unique challenges posed by the anisotropic wave fields resulting from bend curvature.

The research presented in this thesis is structured around the next key components: developing a two-dimensional (2-D) acoustic forward model using Thomsen parameters to represent elliptical anisotropy, enhancing data processing algorithms to reduce experimental uncertainties, and implementing GWT based on FWI to accurately reconstruct the remaining wall thickness of pipe bends. The methodology involves a combination of numerical analysis and experimental validation, demonstrating the effectiveness of the proposed techniques.

Key findings include the successful development of an efficient 2-D acoustic forward model, the implementation of a robust helical path separation algorithm for torus surface, the pre-processing of recorded data, and the validation of the FWI approach through both numerical simulations and experimental data. The 2-D acoustic forward model effectively simulates guided wave propagation and scattering in pipe bends, demonstrating a high degree of agreement between numerical simulations and experimental data. The helical path separation algorithm accurately computes the distances traveled by wave packets, enhancing the precision of defect detection. The updated auto-calibration method resizes the observed data accordingly to address the non-uniqueness problem, and the experimental validation confirms the practical applicability of the methods, with a maximum thickness reconstruction error of only 0.7%.

In addition, the results highlight the advantages of GWT based on FWI over traditional ray-tracing algorithms, particularly in terms of defect detection accuracy and independence from the defect's circumferential position.

This thesis makes a significant contribution to the field by extending the application of GWT based on FWI to more complex structures like pipe bends and addressing key challenges in the process. The findings highlight the advantages of GWT based on FWI over traditional ray-tracing algorithms, particularly in terms of defect detection accuracy and independence from the defect's circumferential position. The methodologies and results presented in this thesis have the potential to drive further research and development, ultimately enhancing the safety and efficiency of pipeline systems.

Kokkuvõte

Ultrahelitomograafia toru põlvede kontrollimiseks

Torustikud ja toru põlved on tööstuse infrastruktuuri kriitilised komponendid. Traditsioonilised mittepurustava kontrolli meetodid, nagu ultrahelil põhinevad paksusmõõtmised, on töömahukad ega pruugi pakkuda toru seisukorra terviklikku hinnangut. Toru põlved on eriti vastuvõtlikud väsimusele, korrosioonile ja pragunemisele, kuna need põhjustavad suuremaid pingeid vedeliku liikumise tõttu. Seetõttu on vajalikud täpsemad ja tõhusamad meetodid nende komponentide jälgimiseks.

Käesolev doktoritöö uurib juhitud lainete tomograafia kasutamist, mis põhineb täieliku lainevormi pöördülekanal, et saavutada kõrge resolutsiooniga toru seinapaksuse rekonstrueerimine.

Töö keskendub anisotroopse akustilise mudeli arendamisele, andmetöötlusalgoritmide täiustamisele ja ultrahelitomograafia rakendamisele, et leida lahendus täpseks toru põlve seinapaksuse rekonstrueerimiseks. Metoodika hõlmab nii numbrilist analüüsi kui ka eksperimentaalset valideerimist, mis tõestavad pakutud tehnikate tõhusust. Eksperimentaalsed tulemused näitavad, et meetod tagab täpsuse, mille maksimaalne toru seina paksuse rekonstrueerimise viga on vaid 0,7%.

Peamised tulemused hõlmavad tõhusa kahemõõtmelise akustilise mudeli väljatöötamist, helikoidaalsete lainevormide lahutamise algoritmi rakendamist geodeetiliste võrrandite põhjal, salvestatud andmete eeltöötlemist ja ultrahelitomograafia meetodi valideerimist nii numbriliste simulatsioonide kui ka eksperimentaalsete andmete põhjal. Eksperimentide valideerimine kinnitab meetodite praktilist rakendatavust maksimaalse paksuse rekonstrueerimise veaga vaid 0.7%.

Tulemused kinnitavad, et ultrahelitomograafial põhinevad meetodid on täpsemad kui traditsioonilised lennuaja tomograafia meetodid, eriti defektide lokaliseerimisel ja kuju täpsel kirjeldamisel. Töö panustab oluliselt torusüsteemide ohutuse ja tõhususe parandamisse ning avab uusi uurimisvõimalusi keerukamate struktuuride analüüsiks.

Appendix 1

I.

Carlos-Omar Rasgado-Moreno, Marek Rist, Raul Land, and Madis Ratassepp. Acoustic Forward Model for Guided Wave Propagation and Scattering in a Pipe Bend. *Sensors*, 22(2):486, January 2022

Article

Acoustic Forward Model for Guided Wave Propagation and Scattering in a Pipe Bend

Carlos-Omar Rasgado-Moreno ^{1,*} , Marek Rist ², Raul Land ² and Madis Ratassepp ^{1,*}

- ¹ Department of Civil Engineering and Architecture, Tallinn University of Technology, 19086 Tallinn, Estonia
² Thomas Johann Seebeck Department of Electronics, Tallinn University of Technology, 19086 Tallinn, Estonia; marek.rist@taltech.ee (M.R.); raul.land@taltech.ee (R.L.)
* Correspondence: carlos.rasgado@taltech.ee (C.-O.R.-M.); madis.ratassepp@taltech.ee (M.R.)

Abstract: The sections of pipe bends are hot spots for wall thinning due to accelerated corrosion by fluid flow. Conventionally, the thickness of a bend wall is evaluated by local point-by-point ultrasonic measurement, which is slow and costly. Guided wave tomography is an attractive method that enables the monitoring of a whole bend area by processing the waves excited and received by transducer arrays. The main challenge associated with the tomography of the bend is the development of an appropriate forward model, which should simply and efficiently handle the wave propagation in a complex bend model. In this study, we developed a two-dimensional (2D) acoustic forward model to replace the complex three-dimensional (3D) bend domain with a rectangular domain that is made artificially anisotropic by using Thomsen parameters. Thomsen parameters allow the consideration of the directional dependence of the velocity of the wave in the model. Good agreement was found between predictions and experiments performed on a 220 mm diameter (d) pipe with 1.5d bend radius, including the wave-field focusing effect and the steering effect of scattered wave-fields from defects.

Keywords: guided waves; scattering; pipe bend; acoustic model; Thomsen parameters; finite differences



Citation: Rasgado-Moreno C.-O.; Rist, M.; Land, R.; Ratassepp, M. Acoustic Forward Model for Guided Wave Propagation and Scattering in a Pipe Bend. *Sensors* **2022**, *22*, 486. <https://doi.org/10.3390/s22020486>

Academic Editor: Luca De Marchi

Received: 10 December 2021

Accepted: 7 January 2022

Published: 9 January 2022

Publisher's Note: MDPI stays neutral with regard to jurisdictional claims in published maps and institutional affiliations.



Copyright: © 2022 by the authors. Licensee MDPI, Basel, Switzerland. This article is an open access article distributed under the terms and conditions of the Creative Commons Attribution (CC BY) license (<https://creativecommons.org/licenses/by/4.0/>).

1. Introduction

Industrial pipelines are largely used to transport highly volatile fluids such as petrochemical products, steam, gas, or oil. However, these pipelines are vulnerable to corrosion and erosion damage [1,2]. Even a pipeline operating with minimal defects can experience catastrophic failures, such as the explosion of the vinyl petrochemical plant Pajaritos in the Gulf of Mexico, which was caused by a leak in one of the principal pipes [3]. Corrosion is often found in fittings, features, crossings, and complex geometries such as bends [4]. Particularly, the sections of pipe bends are damage hot spots due to the sudden change in the fluid flow direction and velocity, thus leading to significant wall thinning by flow-accelerated corrosion [5]. Erosion occurs when there are particles in the flowing solution damaging both the surface layers and the base metal. Therefore, detecting and quantifying damage in critical parts is crucial to guaranteeing the proper operation of pipelines and avoiding disastrous failures.

Common nondestructive testing techniques for pipe bends include local thickness gauges, radiography, and in-pipe robots. Local thickness gauges are handheld measuring devices capable of determining the thickness of a given material using mostly the travel time of ultrasound propagating through the thickness [6]. Although gauges are portable and small training is required to operate them, it is a slow method to cover large areas of interest. Radiography methods are based on using X-rays to penetrate a given structure. Even though they are quite sensitive, measurement systems are bulky, and users are exposed to the X-rays [7]. In addition, in-pipe robots are able to inspect curved pipelines and quantify damages in the structure [8]. Nonetheless, the main drawback is that the

inspected pipe must be removed from operation in order to place the in-pipe robot for inspection and maintenance.

In contrast, ultrasonic guided waves (GWs) have been demonstrated to be an efficient tool for structural health monitoring [9–11]. They are capable of covering large distances in pipelines, being sensitive to cracks and corrosion [12–14]. Usually, ordinary pipeline screening is performed by a single transducer array attached to the pipe in a ring form. The array consists of a fixed number of transducers that can send out the required signals and receive the reflections from the potential defects. As a result, GWs are suitable for constant monitoring, damage detection, developing proper maintenance cycles, and predicting the remaining life and service of pipelines, including bends [15–19]. However, GW propagation in a pipe elbow is more complicated than in a straight pipe due to the curvature of the bend, and it has been studied by a number of authors. For example, Rose et al. [20] reported the natural focusing effect of GWs in a pipe bend and analyzed the echo waveforms for sensing a drill defect. Demma et al. [21] and Hayashi et al. [22] demonstrated that the reflection and transmission of guided waves in the bend are affected by the mode conversions. Rudd et al. [23] studied GW propagation around bends using the elastodynamic finite integration technique. Sanderson et al. [24] introduced an analytical method for GW propagation in the bend and studied the transmission of the T(0,1) mode. Heinlein et al. [25] investigated the reflection of the T(0,1) mode from the cracks in a bend. Xu et al. [26] studied the relationship of GW reflection amplitude with the angle of the bend using a guided wave denoising method. Overall, the primary limitation of the existing screening approaches in characterizing defects in bends is that the information about the defect is limited and therefore does not allow mapping the defect's profile or properly monitoring its progression.

An alternative to overcoming the limitations of ordinary screening is to combine the methods with tomographic techniques. To do so, two transducer rings can be attached to the pipe instead of one, to make it possible to obtain a set of measurements from different angles. Guided wave tomography (GWT) works under the principle of measuring waveforms to form a wall thickness map of a given section. Then, any variation in the waveforms can be interpreted by tomographic algorithms as a thickness reduction in a specific location [27]. The reconstruction of the defects in GWT is based on the solution of an inverse problem that uses a forward model to predict a synthetic dataset for a given structure and a defect shape. The shape of the defect is updated iteratively by minimizing the residuals between the true and synthetic measurements until a convergence criterion is reached. Then, an accurate thickness reconstruction is obtained. The flow chart of the GWT algorithm is shown in Figure 1, where the role of the forward model is highlighted. As a result, the accuracy of the method is strongly influenced by a forward model capable of describing the guided wave propagation in a given structure [28].

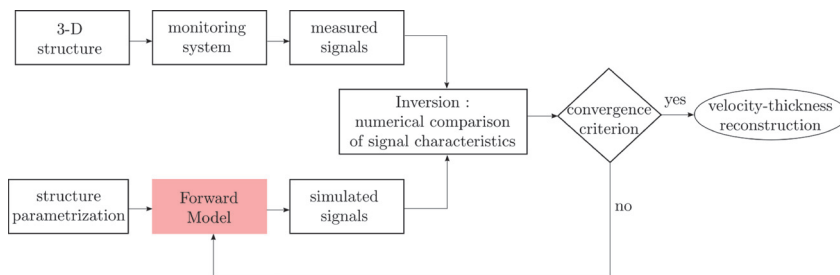


Figure 1. Flow chart of the GWT algorithm: real data (measured signals) and synthetic data (from forward model) are compared iteratively until a given residual criteria is reached. The role of the forward model is highlighted.

In general, approximate 2D forward models are preferred over exact 3D models, due to their simplicity, low computational cost, feasibility of combining with tomographic algorithms, and their capability to evaluate the thickness of the waveguides from the velocity. Furthermore, the majority of research on GWT has focused on simple geometries, such as flat plates [29–32] and straight pipes [33–35]. However, only a few studies have investigated the application of GWT to pipe bends. Volker and van Zon [36] developed a forward model based on a recursive wave-field extrapolation and a deformed 2D planar grid and applied it in travel-time tomography. Brath et al. [37] introduced a 2D rectangular forward model for GW propagation in the bend, in which the equivalence was established by the travel-time-preserving orthogonal parametric presentation of the bend. Later, it was extended to curved ray tomography [38]. A similar model with the sparse inversion method was used by Wang and Li [39] in GWT for quantifying defects in the bend. However, all these approaches are limited to using the travel times of first arrivals, which limits the resolution of tomographic imaging [40].

In this study, we developed a 2D acoustic forward model for pipe bends that can be further used in tomography along with the full waveform inversion (FWI) algorithm. The FWI makes use of the full information of the wave field, thus enabling more accurate inversion results to be achieved compared to travel-time tomography [41]. The forward model is discretized by the finite difference (FD) method and the equivalence with the bend domain is established by an artificial anisotropic formulation using Thomsen parameters [42]. We investigated the transmission of the A_0 mode through a 90° pipe bend from different excitation points and compared the simulation results of the FD method with the results obtained from finite element (FE) modeling and experiments. In addition, the scattering from artificial defects in the bend was analyzed.

This paper is structured as follows: Section 2 outlines the methods for translating the 3D geometry of the bend into the 2D domain, and the implemented numerical methods are presented in Section 3. This approach is subsequently validated with the experimental setup described in Section 4, and the results are presented in Section 5. Finally, conclusions are drawn in Section 6.

2. Forward Model

In this section, we describe the equivalent 2D wave propagation model for the simulation of guided waves in a 3D pipe bend. Firstly, the 3D modeling domain is mapped to the 2D domain by using orthogonal parameterization of the space. Secondly, the anisotropic wave propagation model is introduced and then anisotropic Thomsen parameters are defined to fit the acoustic velocity model with the real guided wave model.

2.1. Orthogonal Parameterization

Consider the section of the torus in Figure 2a, defined in the 3D space domain Σ , with mid-thickness or central radius r , bend radius R , torus azimuth longitude β around the Y -axis, and torus latitude α with respect to the XY plane. To model the anisotropic wave propagation around the bend in the 2D space domain Ω shown in Figure 2b, a translation of the torus section from Σ to Ω is needed. We followed the parametrization proposed by Brath et al. [37]. According to this, the torus section is unwrapped from the longest radius path of the bend (at extrados position $R + r$). Secondly, the 2D horizontal and vertical axes x and y were set equal to the torus circumference $2\pi r$ and the bend's extrados azimuth length $\beta(R + r)$, respectively. As a result, the 2D domain Ω can be expressed as $\Omega = [0, 2\pi r] \times [0, \beta(R + r)]$, with the extrados position located at the middle of the circumference at $(\pi r, y)$. The intrados position is located at the beginning of the circumference at $(0, y)$ and at the end $(2\pi r, y)$.

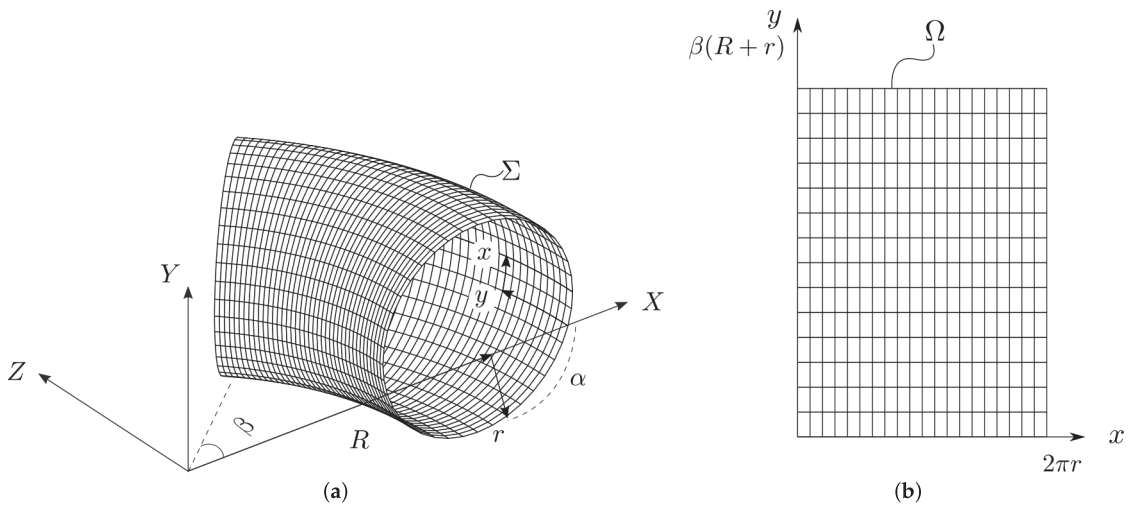


Figure 2. A torus section representing the bend of a pipe is translated from (a) the 3D space domain Ω to (b) the 2D space domain Ω .

Orthogonal parameterization of the torus is given by the set of equations as follows:

$$\begin{aligned} X &= \left(R + r \cos \frac{x}{r}\right) \cos \frac{y}{R+r} \\ Y &= r \sin \frac{x}{r} \\ Z &= \left(R + r \cos \frac{x}{r}\right) \sin \frac{y}{R+r}, \end{aligned} \quad (1)$$

where the two-dimensional coordinates $\{x, y\}$ are used to express the three-dimensional space coordinates $\{X, Y, Z\}$. In this way, the 3D space coordinates can be mapped directly into the 2D domain, and vice versa.

2.2. Acoustic Wave Equation

We assume that a guided wave propagating in a bent wall of varying thickness will behave the same as an acoustic wave traveling in a 2D medium with varying velocity. The model is shown in Figure 3, and the acoustic wave is modeled in transversely isotropic media with a vertical symmetry axis and is described by fourth-order partial differential equations in time t [43]:

$$\frac{\partial^4 F}{\partial t^4} - v_\phi^2(1 + 2\eta) \left(\frac{\partial^4 F}{\partial y^2 \partial t^2} \right) = v_0^2 \frac{\partial^4 F}{\partial x^2 \partial t^2} - 2\eta v_0^2 v_\phi^2 \left(\frac{\partial^4 F}{\partial y^2 \partial x^2} \right) \quad (2)$$

with η defined as

$$\eta = \frac{\epsilon - \delta}{1 + 2\delta}.$$

In Equation (2), $F(x, y, t)$ describes the pressure field of the propagating wave, v_ϕ is the phase velocity, v_0 is the phase velocity along the x -axis, and ϵ, δ is the nondimensional Thomsen parameters to describe the anisotropy of the wave field.

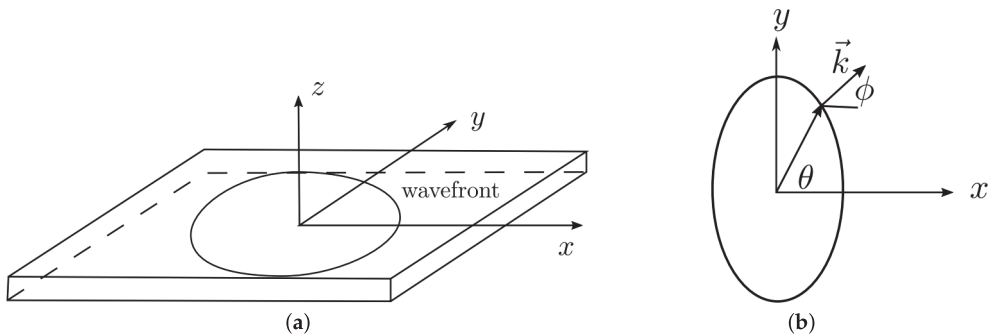


Figure 3. (a) Acoustic model of GW propagation in a plate with vertical transverse isotropy. (b) Top view of the wave field, group angle θ , wave number \vec{k} , and phase angle ϕ .

2.3. Implementation for a Pipe Bend

To link the phase velocity v_ϕ of the acoustic wave to the geometry of the pipe, we use the approximated Thomsen parameters [42,44], which are defined by the phase velocity v_ϕ at three different angles, horizontal v_0 , vertical $v_{\pi/2}$, and $v_{\pi/4}$:

$$\begin{aligned}\epsilon &= \frac{v_{\pi/2} - v_0}{v_0} \\ \delta &= 4\left(\frac{v_{\pi/4}}{v_0} - 1\right) - \epsilon,\end{aligned}\quad (3)$$

where ϵ quantifies the velocity difference between the wave propagation along the vertical direction, and δ is the wave propagation at intermediate phase angles.

As the pipe bend is unwrapped at the extrados position, the velocities $v_{\pi/2} = v_0$ and $\epsilon = 0$. Additionally, the vertical velocity $v_{\pi/2}$ at each point of the circumference can be expressed in terms of distance as $(R + r \cos(\alpha)) / (R + r)v_0$. In this way, ϵ can be written as a function of the radius of the bend R and the central radius r of the pipe as

$$\epsilon = \frac{R + r}{R + r \cos \alpha} - 1. \quad (4)$$

In addition, the phase velocity $v_{\pi/4}$ used to obtain δ can be computed from the phase angle ϕ related to the group angle θ [37] described by

$$\tan \phi = \frac{\tan \theta}{\left(\frac{v_{\pi/2}}{v_0}\right)^2}. \quad (5)$$

In this way, we use Equations (3) and (4) to compute Thomsen parameters for GW propagation in the bend.

3. Numerical Methods

3.1. Configuration of the Problem

For both models and measurements, we considered the steel pipe specimen described in Figure 4, with inner radius $r_{in} = 0.1015$ m, outer radius $r_{out} = 0.1095$, 90° bend with radius $R = 0.329$ m, and two straight pipe sections at the beginning and at the end of the bend that are 0.20 m long each (only included in the 3D model as absorbing regions). The steel's properties are listed in Table 1. We refer to the longest and shortest arcs of the bend as extrados and intrados, respectively. Similarly, we use top and bottom for the mid-bend's arc between the intrados and extrados.

Table 1. Steel pipe material properties. Density ρ , Young’s modulus E , and Poisson ratio ν .

ρ (kg/m ³)	E (GPA)	ν
7932	216.9	0.2865

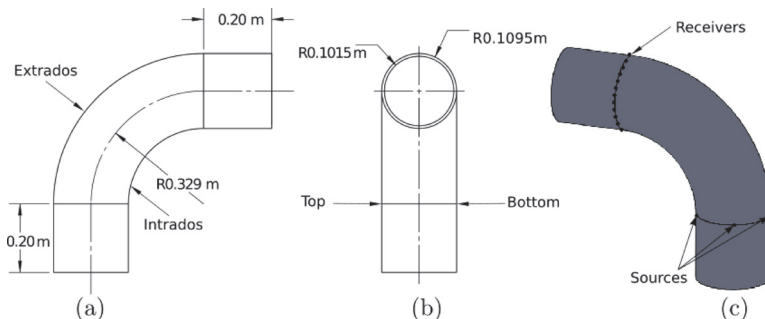


Figure 4. Schematic of the pipe bend. (a) Top view, (b) lateral view, and (c) isometric view of the simulated pipe bend.

Guided waves were excited at the beginning of the bend at three source positions: intrados, top, and extrados. We expected that the waves excited from these points would propagate differently due to the geometric anisotropy that can be described by Thomsen parameters. For the excitation, we used a five-cycle A_0 mode with central frequency at 50 kHz modulated by a Hanning window. The waves were monitored at the other side of the bend at 20 receiving points that were equally distributed around the circumference.

To investigate the scattering of the waves from defects, we modeled a Hann-shaped thickness reduction defect with a center $\{X_c, Y_c, Z_c\}$ by resizing the pipe thickness T from the outer surface using the following equation:

$$T = \begin{cases} t_0 - \frac{D}{2} \left[1 + \cos\left(\frac{2\pi|T|}{W}\right) \right], & |T| < \frac{W}{2} \\ t_0, & |T| > \frac{W}{2} \end{cases} \quad (6)$$

where $|T| = \sqrt{(X - X_c)^2 + (Y - Y_c)^2 + (Z - Z_c)^2}$, t_0 is the nominal pipe thickness, and D and W are the depth and width of the defect, respectively. In this study, the size of the selected defect was 120 mm wide and its maximum depth was 30% of the thickness reduction. The defect was placed at the center of the pipe elbow and was simulated in three locations: extrados, top, and intrados. The respective 2D thickness models are shown in Figure 5. It can be seen that the defect was circular at the extrados and became elliptical when moving toward the intrados as a consequence of the unwrapping of the bend.

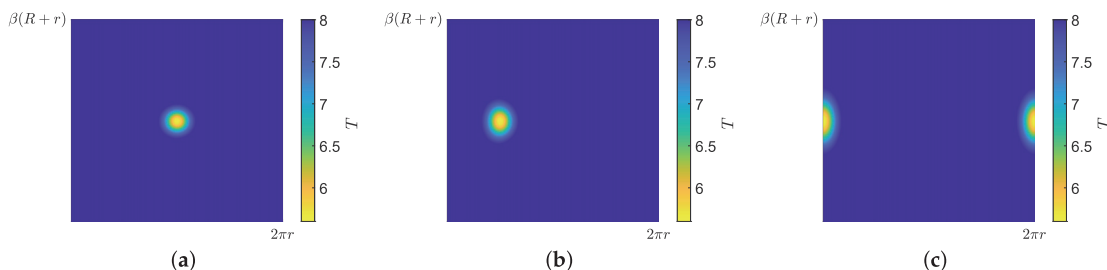


Figure 5. Thickness T (mm) in the 2D acoustic domain with a Hann-shaped defect at three different locations: (a) extrados, (b) top, and (c) intrados.

3.2. FE Modeling

The ABAQUS Explicit software was used [45] for the 3D guided wave propagation simulations in the pipe bend described in Figure 4. To build the section of the bend, first, we defined a circular mesh with 560 elements along the circumference of the pipe and 6 elements along with the thickness. Second, we rotated the circular mesh according to the geometry of the pipe bend, as shown in Figure 4a. The number of elements along the 90 degree rotation was 550. The eight-node brick element type C3D8R was used. In order to avoid reflections from the boundaries, we defined absorbing regions on the straight pipe sections [46]. The number of elements along each straight section was 160. On one bend's side, we generated the A_0 mode by applying an out-of-plane force in the radial direction. We excited three different source positions separately as we described previously (intrados, top, and extrados positions). On the other bend's side, we measured radial displacement components. A sample of the pipe bend geometry simulated in ABAQUS for the extrados case with a Hann-shaped defect is shown in Figure 6.

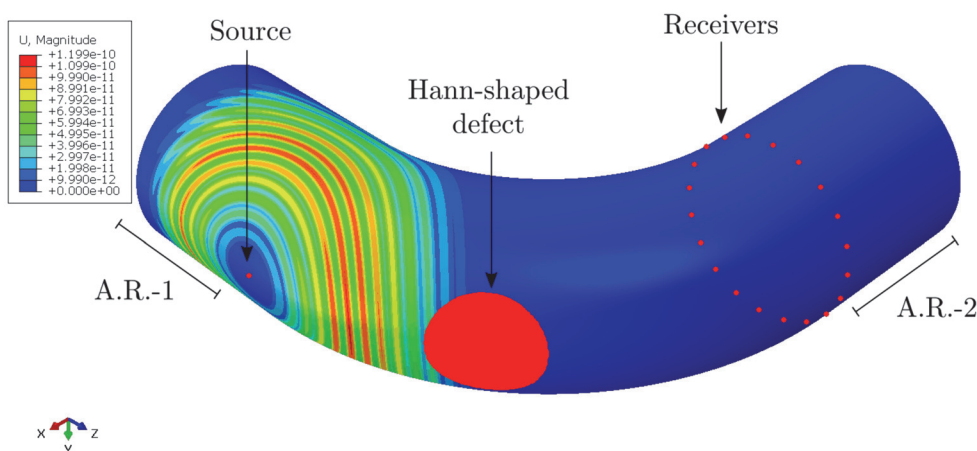


Figure 6. Geometry of the pipe bend simulated in ABAQUS for the *extrados* case with a Hann-shaped defect, absorbing regions (ARs) 1 and 2, and displacements of the propagating waves shown at 100 μ s.

In addition to transmission measurements, the scattering from Hann-shaped defects was investigated. The defect wave field was isolated by using the baseline wave-field subtraction.

3.3. Acoustic Modeling

The simulations in the acoustic domain were performed with the finite difference (FD) method using the mixed-grid approach [47]. The calculation domain consisted of three replicas to include the higher-order helical wave paths in the simulation [37]. Each replica was discretized with 161 grid points along the circumferential direction and 166 grid points in the axial direction, and it was sampled with a grid step of 4.143 mm. The background models showing the distribution of Thomsen parameters and the velocity distribution of the bend with the defect and the source located at the extrados position are shown in Figure 7. The wave propagation was isotropic along the extrados of the bend where Thomsen parameters were zero, while it became increasingly anisotropic when the waves transmitted through the intrados area where Thomsen parameters are the largest. The velocity models at a required frequency were obtained from the thickness map by using the velocity–frequency–thickness dispersion curve of the A_0 mode. To obtain the higher-order helical wave paths in the simulation, the source in each replica was excited separately and their responses were summed. The procedure was repeated with the source and the defect located at the top and intrados position of the bend.

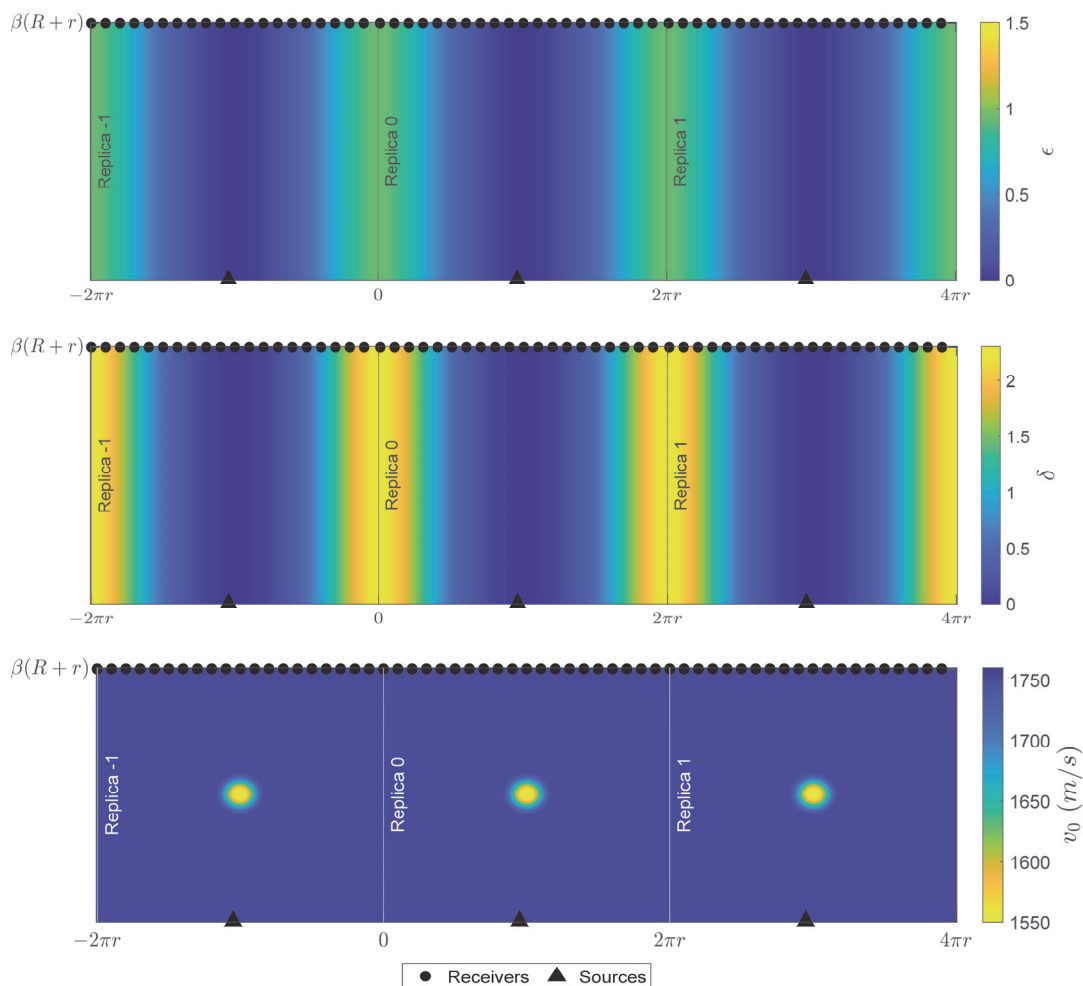


Figure 7. (a,b) ϵ and δ distribution along the bend with 3 replicas, respectively. Sources were placed at the extrados position of each replica. (c) v_0 in the bend with a Hann-shaped defect located at the extrados position. A similar velocity model was created for each computed frequency.

Calculations were performed using the two-dimensional frequency-domain engine TOY2DAC [48] to solve Equation (2) in the frequency domain for the required frequency components. The inverse fast Fourier transform was used to transform the frequency-domain results into a time domain. A 2x Intel Xeon E5-2660v2, 64 GB RAM cluster was used for the computation, and the calculation time was 7 min for a single excitation case.

4. Experimental Measurements

We used the experimental setup shown in Figure 8a. It consisted of a steel pipe bend, which was supported by four wooden holds, and it had the same properties and dimensions as described in Table 1 and Figure 4a, respectively; the only exception was that the straight pipe sections were 1 m long each, so that the reflections with the edges were avoided in the measurement. The measurement setup consisted of two rings of transducers located at each end of the bend, one multiplexer for exciting the desired signal, and a data acquisition box.

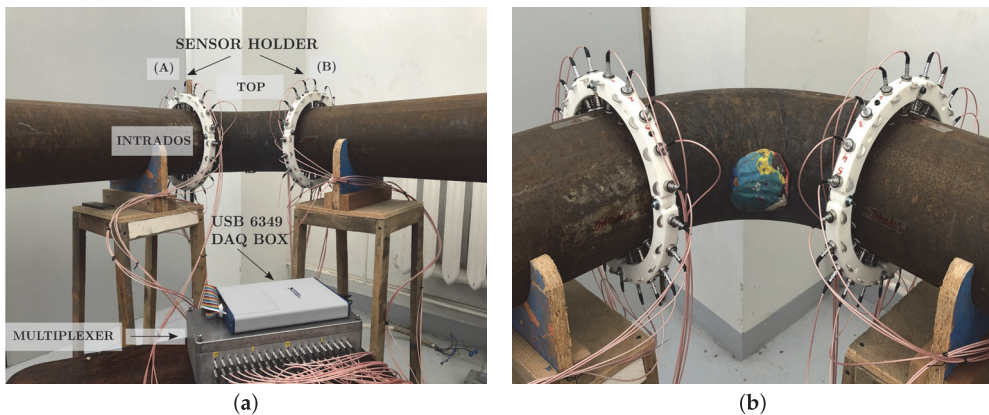


Figure 8. (a) Steel pipe bend specimen with the same characteristics as in Table 1. Measurement setup with transducer arrays A and B with 20 transducers each and an acquisition system; (b) pipe bend with an artificial defect composed of plasticine and located on the intrados position, *intrados* view.

Each ring of transducers (ring A and ring B) contained 20 piezoelectric transducers (Doppler Ltd., Guangzhou, China) with a central frequency of 50 kHz. They were used as both transducers and receivers. The transducers were equally distributed along the circumference and they were pressed against the pipe with springs so that the excitation was applied in the radial direction. Similarly, radial displacements were measured with the receiving transducer ring. Sensor no. 1 was located at the intrados, sensor no. 6 was at the top, and sensor no. 11 was at the extrados. The used multiplexer contained 20 sensing channels for amplification and conditioning the measured responses. The multiplexer network allowed switching the excitation to any transducer at one ring, and the receiving channels were connected to all the elements on the opposite ring.

In addition, the multifunctional USB-6349 from National Instruments was used for data acquisition. It was connected to the PC via a USB and featured 32 simultaneous analog input channels with a 500 kS/s sampling rate and 16-bit resolution. It also contained two 16-bit analog output channels and 24 general-purpose digital input/output channels. The acquisition software was created in LabView [49], and was used for creating the excitation waveforms, creating and running through the multiplexer channels, and connecting the piezoelectric elements to excitation amplifiers or receiving amplifiers. The excitation waveforms were sent to the data acquisition and the response waveforms were measured, digitally filtered, and logged.

The transmission of the A_0 mode through the bend was investigated for the three excitation points located at the extrados, top, and intrados positions of the bend. For the scattering studies, we used plasticine ($\rho = 1452.3 \text{ kg/m}^3$, $mass = 0.244 \text{ kg}$, $r = 50 \text{ mm}$) attached to the surface of the pipe, as shown in Figure 8b. It is thought that the A_0 mode, which has a wave field dominated by the out-of-plane displacement, is sensitive to the coating layer and causes scattering. Additionally, plasticine has easy molding properties so it could be attached and removed from the pipe without changing the pipe's material or the coupling condition between the transducers and the pipe. This was important for the baseline wave-field subtraction. Therefore, the position of the plasticine was changed for each excitation point and was aligned with the excitation point along the bend axis.

5. Results and Discussion

In this section, we investigate the wave field of the A_0 mode transmitted through the bend and its scattering from the defect located in the bend. The results from the experiment, FE, and FD modeling are presented and compared.

5.1. Guided Wave Propagation in the Pipe Bend

The A_0 mode at 50 kHz was excited separately in three different locations: at the extrados, top, and intrados of the bend beginning; and its propagating wave field was measured with a transducer ring at the bend end. The experimentally obtained contour plots of radial displacements of the received waves are shown in Figure 9 with FE and FD methods. The amplitudes of the received waves were normalized by the maximum displacement value of the recorded signals.

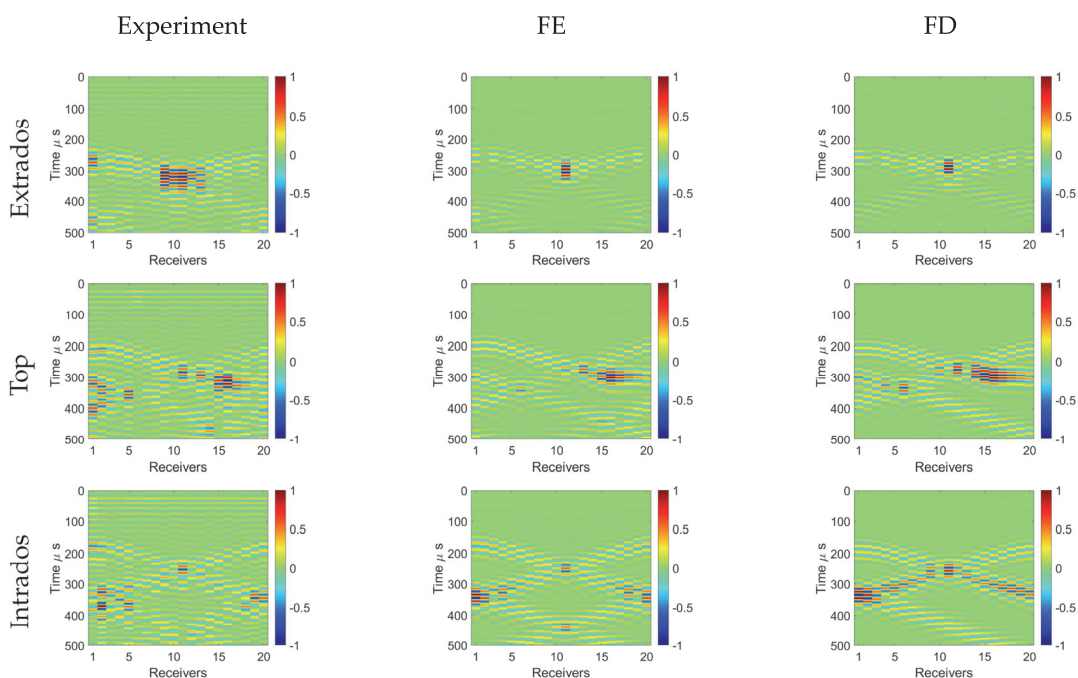


Figure 9. Experimental, FE, and FD contour plots of normalized radial displacement in the bend for three excitation positions: extrados, top, and intrados. The A_0 mode was excited with a central frequency of 50 kHz.

First, it can be seen that the recorded wave patterns differed for different excitation points, which occurred due to the effect of dissimilar ray paths and distances. A symmetric wave pattern can be seen in the case of the excitation located at the extrados and intrados positions, and nonsymmetric behavior was characteristic for the excitation at the top. This is related to the symmetry of the model parameters of the bend and the position of the excitation, as shown in Figure 7. Second, it can be observed that the direct first arrivals were followed by the wave-packets, which were helical waves propagating around the bend multiple times. Some helical waves arriving after 400 μ s were not seen in the FD results due to the limited number of replicas used in the simulation.

Some specific observations were made for each excitation location. In the case of the extrados excitation, the slowest but most energetic signal was measured at the extrados position (transducer no. 11). This is due to the longest traveling distance along the extrados

and the wave-field focusing caused by the lensing effect determined by the sound-speed valley [37]. When exciting from the top position (transducer no. 6), the waves naturally followed the shortest path toward the intrados and there were helical paths arriving before the wavefront. This was observed at receivers 13–20, where the focusing effect was also present but pushed more toward the intrados of the bend due to the horizontal velocity component of the wave. For the intrados excitation (transducer no. 1), the wave propagation was fastest along the intrados direction but lost more energy in this direction compared to the wavefront making the full circle around the bend. As the helical trajectory was also shorter compared to extrados excitation, the higher-order helical waves arrived earlier to the receivers. In addition, the right helical wave, which should have appeared at transducer 20 from 300 μs , was missing in the FD result. One extra replica is needed on the right side of the model to make it appear.

Overall, it can be seen that the FD results obtained by the proposed acoustic forward model agree well with the FE result, showing that the model can accurately represent reality and the experimental results. The results from the experiment were noisier and there were more variations in the amplitudes compared to the simulation results. This can be explained by the uneven coupling of the transducer to the pipe surface. In addition, there was notable noise present before 150 μs . This noise was a consequence of the crosstalk from the transducer source with the transducer receivers. However, the arrival times of the wave-packets well-matched the ones from the simulations, and we could observe the focusing effect in the case of extrados and top excitation. In general, this measurement example demonstrated the suitability of the introduced 2D acoustic model for predicting waveforms of guided waves in pipe bends.

5.2. Scattered Wave Fields in the Pipe Bend

The scattering of the A_0 mode was investigated from the defects at the center of the pipe elbow on the extrados, top, and intrados positions, separately. In simulations, a defect as the outer surface thickness reduced with Hann-shape variations was considered; in the experiment, a circular plasticine layer attached to the pipe surface was used. Wave fields scattered from the defect were isolated by subtracting the received waveforms of the intact pipe bend from the waveforms measured in the pipe bend with the defect.

The contour plots of radial displacements of the scattered waves are shown in Figure 10, obtained experimentally with the FE and FD methods. The amplitudes of the waves were normalized by the maximum displacement value of the recorded signals from the intact pipe bend measurements. We focused on the first-arrived scattering, which was the most energetic. It can be seen that the scattering was dependent on the location of the excitation and the defect. In the case of the extrados excitation, we observed that the scattering was localized and remained at the extrados position. Interestingly, for the top excitation (transducer no. 6), the scattered wave was strongly steered and it arrived on the bottom side of the bend. Similar behavior to that of the waves was observed in the intact bend where the wave energy from the top excitation focused on the opposite side of the bend. Finally, when the excitation and the defect were at the intrados of the bend, the scattered wave followed the intrados direction but its pattern was much wider as the wave energy tried to escape from the sound-speed hill, which is opposite to the lensing effect and focusing.

In general, there was a clear resemblance in the scattered wave fields obtained with the different methods. The interaction of the wave with the plasticine in the experiment was a bit weaker compared to the interaction with the thickness reduction in the simulations. In addition, the experimental results were contaminated by noise, especially observed for the case with top excitation; however, the scattered wave field could be confidently observed. The biggest difference was observed with the intrados excitation, where the scattered field in the experiment was not symmetric compared to the modeling results, and spread across the bend. We think that this may have been caused by the directionality of the transducers, meaning that the waves were not equally excited around the intrados directions. In Figure 9, we can see that larger amplitudes were received at receivers 1–5 than

those at 15–20, which could have resulted in some directivity in the scattering patterns. This scattering study demonstrated that the proposed acoustic model is capable of predicting correct waveforms from the defects in different locations, which is an important feature for accurate tomographic calculation.

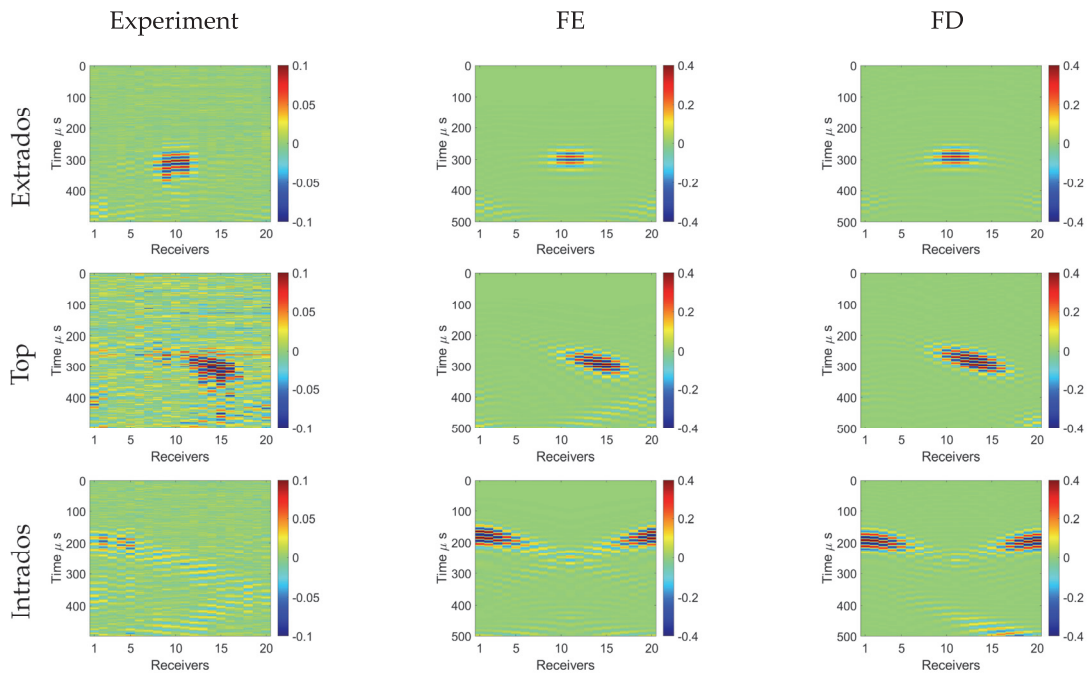


Figure 10. Experimental, FE, and FD scattered wave fields in the bend when the excitation sources and defects were located at three different positions: extrados, top, and intrados. Plasticine was used for producing scattered waves in the experiment, and a Hann-shaped defect was modeled in FE and FD simulations.

6. Conclusions

In this study, an efficient and simple forward model was developed to simulate guided wave propagation and scattering in pipe bends. The 3D elastic bend was replaced by the 2D rectangular anisotropic acoustic domain by using orthogonal parameterization. The equivalence in the wave propagation was established based on implementing approximate anisotropic Thomsen parameters that describe the angular variability of the velocity in the acoustic model. The model was used to simulate the A_0 mode propagation and interaction with the defects from different excitation points across the bend. We found that the wave excited at the extrados focused at the extrados side of the bend. The wave excited from the top tended to focus on the opposite bottom side of the bend, which also caused the steering effect of the wave field scattered from the defect. The wave excited from the intrados tended to lose energy in other directions. Good agreement was found between the results from the proposed modeling method, the FE modeling, and the experimental results. Future work should involve combining the introduced forward model with FWI tomography to construct accurate corrosion maps for the pipe bends.

Author Contributions: Conceptualization, C.-O.R.-M. and M.R. (Madis Ratassepp); methodology, C.-O.R.-M.; simulations and data acquisition, C.-O.R.-M.; experimental setup and software, M.R. (Marek Rist) and R.L.; writing—original draft preparation, C.-O.R.-M.; writing—review and editing,

C.-O.R.-M. and M.R. (Madis Ratassepp); project administration and funding acquisition, M.R. (Madis Ratassepp). All authors have read and agreed to the published version of the manuscript.

Funding: This research was funded by the European Union’s Horizon 2020 Research and Innovation Programme under grant agreement no. 860104, project GW4SHM (Guided Waves for Structural Health Monitoring), and the Estonian Research Council, grant PRG737.

Institutional Review Board Statement: Not applicable.

Informed Consent Statement: Not applicable.

Data Availability Statement: The measurement data are available on request from the authors.

Conflicts of Interest: The authors declare no conflict of interest.

References

- Talebi, M.; Zeinoddini, M.; Mo’tamedi, M.; Zandi, A. Collapse of HSLA steel pipes under corrosion exposure and uniaxial inelastic cycling. *J. Constr. Steel Res.* **2018**, *144*, 253–269. [CrossRef]
- Yan, Z.; Wang, L.; Zhang, P.; Sun, W.; Yang, Z.; Liu, B.; Tian, J.; Shu, X.; He, Y.; Liu, G. Failure analysis of Erosion-Corrosion of the bend pipe at sewage stripping units. *Eng. Fail. Anal.* **2021**, *129*, 105675. [CrossRef]
- Leak Blamed as Mexico Explosion Death Toll Rises. Available online: <https://www.theguardian.com/world/2016/apr/22/leak-blamed-as-mexico-explosion-death-toll-rises> (accessed on 30 June 2021).
- Muthanna, B.G.N.; Amara, M.; Meliani, M.H.; Mettai, B.; Božić, Z.; Suleiman, R.; Sorour, A. Inspection of internal erosion-corrosion of elbow pipe in the desalination station. *Eng. Fail. Anal.* **2019**, *102*, 293–302. [CrossRef]
- Kusmono; Khasani. Analysis of a failed pipe elbow in geothermal production facility. *Case Stud. Eng. Fail. Anal.* **2017**, *9*, 71–77. [CrossRef]
- Lebowitz, C.A.; Brown, L.M. Measurement of Pipe Thickness. In *Review of Progress in Quantitative Nondestructive Evaluation: Volumes 12A and 12B*; Springer: Boston, MA, USA, 1993; pp. 1987–1994. [CrossRef]
- Dwivedi, S.K.; Vishwakarma, M.; Soni, P.A. Advances and Researches on Non Destructive Testing: A Review. *Mater. Today Proc.* **2018**, *5*, 3690–3698. [CrossRef]
- Mishra, D.; Agrawal, K.K.; Abbas, A.; Srivastava, R.; Yadav, R.S. PIG [Pipe Inspection Gauge]: An Artificial Dustman for Cross Country Pipelines. *Procedia Comput. Sci.* **2019**, *152*, 333–340. [CrossRef]
- Mitra, M.; Gopalakrishnan, S. Guided wave based structural health monitoring: A review. *Smart Mater. Struct.* **2016**, *25*, 053001. [CrossRef]
- Guan, R.; Lu, Y.; Duan, W.; Wang, X. Guided waves for damage identification in pipeline structures: A review. *Struct. Control. Health Monit.* **2017**, *24*, e2007. [CrossRef]
- Su, Z.; Ye, L.; Lu, Y. Guided Lamb waves for identification of damage in composite structures: A review. *J. Sound Vib.* **2006**, *295*, 753–780. [CrossRef]
- Alleyn, D.; Cawley, P. Long range propagation of Lamb waves in chemical plant pipework. *Mater. Eval.* **1997**, *55*, 504–508.
- Ghavamian, A.; Mustapha, F.; Baharudin, B.; Yidris, N. Detection, Localisation and Assessment of Defects in Pipes Using Guided Wave Techniques: A Review. *Sensors* **2018**, *18*, 4470. [CrossRef] [PubMed]
- Vogt, T.; Heinlein, S.; Milewicz, J.; Mariani, S.; Jones, R.; Cawley, P. Guided Wave Monitoring of Industrial Pipework—Improved Sensitivity System and Field Experience. In *European Workshop on Structural Health Monitoring*; Springer International Publishing: Berlin/Heidelberg, Germany, 2021; pp. 819–829.
- Lowe, P.S.; Sanderson, R.; Pedram, S.K.; Boulgouris, N.V.; Mudge, P. Inspection of Pipelines Using the First Longitudinal Guided Wave Mode. *Phys. Procedia* **2015**, *70*, 338–342. [CrossRef]
- Yan, S.; Zhang, B.; Song, G.; Lin, J. PZT-Based Ultrasonic Guided Wave Frequency Dispersion Characteristics of Tubular Structures for Different Interfacial Boundaries. *Sensors* **2018**, *18*, 4111. [CrossRef]
- Song, Z.; Qi, X.; Liu, Z.; Ma, H. Experimental study of guided wave propagation and damage detection in large diameter pipe filled by different fluids. *NDT E Int.* **2018**, *93*, 78–85. [CrossRef]
- Olisa, S.C.; Khan, M.A.; Starr, A. Review of Current Guided Wave Ultrasonic Testing (GWUT) Limitations and Future Directions. *Sensors* **2021**, *21*, 811. [CrossRef]
- Heinlein, S.; Cawley, P.; Vogt, T. Validation of a procedure for the evaluation of the performance of an installed structural health monitoring system. *Struct. Health Monit.* **2019**, *18*, 1557–1568. [CrossRef]
- Rose, J.L.; Zhang, L.; Avioli, M.J.; Mudge, P.J. A Natural Focusing Low Frequency Guided Wave Experiment for the Detection of Defects Beyond Elbows. *J. Press. Vessel. Technol.* **2005**, *127*, 310–316. [CrossRef]
- Demma, A.; Cawley, P.; Lowe, M.; Pavlakovic, B. The Effect of Bends on the Propagation of Guided Waves in Pipes. *J. Press. Vessel. Technol.* **2005**, *127*, 328–335. [CrossRef]
- Hayashi, T.; Kawashima, K.; Sun, Z.; Rose, J.L. Guided Wave Propagation Mechanics Across a Pipe Elbow. *J. Press. Vessel. Technol.* **2005**, *127*, 322–327. [CrossRef]

23. Rudd, K.E.; Leonard, K.R.; Bingham, J.P.; Hinders, M.K. Simulation of guided waves in complex piping geometries using the elastodynamic finite integration technique. *J. Acoust. Soc. Am.* **2007**, *121*, 1449–1458. [[CrossRef](#)]
24. Sanderson, R.M.; Hutchins, D.A.; Billson, D.R.; Mudge, P.J. The investigation of guided wave propagation around a pipe bend using an analytical modeling approach. *J. Acoust. Soc. Am.* **2013**, *133*, 1404–1414. [[CrossRef](#)]
25. Heinlein, S.; Cawley, P.; Vogt, T. Reflection of torsional T(0,1) guided waves from defects in pipe bends. *NDT E Int.* **2018**, *93*, 57–63. [[CrossRef](#)]
26. Xu, Z.D.; Zhu, C.; Shao, L.W. Damage Identification of Pipeline Based on Ultrasonic Guided Wave and Wavelet Denoising. *J. Pipeline Syst. Eng. Pract.* **2021**, *12*, 04021051. [[CrossRef](#)]
27. Jansen, D.; Hutchins, D. Lamb wave tomography. In *IEEE Symposium on Ultrasonics*; IEEE: New York, NY, USA, 1990; Volume 2, pp. 1017–1020. [[CrossRef](#)]
28. Huthwaite, P. Evaluation of inversion approaches for guided wave thickness mapping. *Proc. R. Soc. A Math. Phys. Eng. Sci.* **2014**, *470*, 20140063. [[CrossRef](#)]
29. Rohde, A.H.; Veidt, M.; Rose, L.R.F.; Homer, J. A computer simulation study of imaging flexural inhomogeneities using plate-wave diffraction tomography. *Ultrasonics* **2008**, *48*, 6–15. [[CrossRef](#)]
30. Huthwaite, P.; Simonetti, F. High-resolution guided wave tomography. *Wave Motion* **2013**, *50*, 979–993. [[CrossRef](#)]
31. Rao, J.; Ratasseppe, M.; Fan, Z. Guided Wave Tomography Based on Full Waveform Inversion. *IEEE Trans. Ultrason. Ferroelectr. Freq. Control.* **2016**, *63*, 737–745. [[CrossRef](#)]
32. Lin, M.; Wilkins, C.; Rao, J.; Fan, Z.; Liu, Y. Corrosion detection with ray-based and full-waveform guided wave tomography. In *Nondestructive Characterization and Monitoring of Advanced Materials, Aerospace, Civil Infrastructure, and Transportation XIV*; SPIE: Bellingham, WA, USA, 2020; Volume 11380, pp. 102–109. [[CrossRef](#)]
33. Volker, A.; Mast, A.; Bloom, J. Experimental results of guided wave travel time tomography. *AIP Conf. Proc.* **2010**, *1211*, 2052–2059. [[CrossRef](#)]
34. Willey, C.L.; Simonetti, F.; Nagy, P.B.; Instanes, G. Guided wave tomography of pipes with high-order helical modes. *NDT E Int.* **2014**, *65*, 8–21. [[CrossRef](#)]
35. Huthwaite, P.; Ribichini, R.; Cawley, P.; Lowe, M.J. Mode selection for corrosion detection in pipes and vessels via guided wave tomography. *IEEE Trans. Ultrason. Ferroelectr. Freq. Control.* **2013**, *60*, 1165–1177. [[CrossRef](#)]
36. Volker, A.; van Zon, T. Guided wave travel time tomography for bends. *AIP Conf. Proc.* **2013**, *1511*, 737–744. [[CrossRef](#)]
37. Brath, A.J.; Simonetti, F.; Nagy, P.B.; Instanes, G. Acoustic formulation of elastic guided wave propagation and scattering in curved tubular structures. *IEEE Trans. Ultrason. Ferroelectr. Freq. Control.* **2014**, *61*, 815–829. [[CrossRef](#)] [[PubMed](#)]
38. Brath, A.J.; Simonetti, F.; Nagy, P.B.; Instanes, G. Guided Wave Tomography of Pipe Bends. *IEEE Trans. Ultrason. Ferroelectr. Freq. Control.* **2017**, *64*, 847–858. [[CrossRef](#)]
39. Wang, Y.; Li, X. Elbow Damage Identification Technique Based on Sparse Inversion Image Reconstruction. *Materials* **2020**, *13*, 1786. [[CrossRef](#)]
40. Belanger, P.; Cawley, P. Feasibility of low frequency straight-ray guided wave tomography. *NDT E Int.* **2009**, *42*, 113–119. [[CrossRef](#)]
41. Rao, J.; Ratasseppe, M.; Fan, Z. Investigation of the reconstruction accuracy of guided wave tomography using full waveform inversion. *J. Sound Vib.* **2017**, *400*, 317–328. [[CrossRef](#)]
42. Ratasseppe, M.; Rao, J.; Yu, X.; Fan, Z. Modeling the Effect of Anisotropy in Ultrasonic Guided Wave Tomography. *IEEE Trans. Ultrason. Ferroelectr. Freq. Control.* **2022**, *69*, 330–339. [[CrossRef](#)]
43. Alkhalifah, T. An acoustic wave equation for anisotropic media. *Geophysics* **2000**, *65*, 1239–1250. [[CrossRef](#)]
44. Thomsen, L. Weak elastic anisotropy. *Geophysics* **1986**, *50*, 1954–1966. [[CrossRef](#)]
45. *ABAQUS/Standard User's Manual*, version 6.14; Dassault Systèmes Simulia Corp.: Providence, RI, USA, 2014.
46. Drozd, M.; Moreau, L.; Castaings, M.; Lowe, M.J.S.; Cawley, P. Efficient Numerical Modelling of Absorbing Regions for Boundaries Of Guided Waves Problems. *AIP Conf. Proc.* **2006**, *820*, 126–133. [[CrossRef](#)]
47. Operto, S.; Virieux, J.; Ribodetti, A.; Anderson, J.E. Finite-difference frequency-domain modeling of viscoacoustic wave propagation in 2D tilted transversely isotropic (TTI) media. *Geophysics* **2009**, *74*, T75–T95. [[CrossRef](#)]
48. Métivier, L.; Brossier, R. The SEISCOPE optimization toolbox: A large-scale nonlinear optimization library based on reverse communication. *Geophysics* **2016**, *81*, F1–F15. [[CrossRef](#)]
49. Bitter, R.; Mohiuddin, T.; Nawrocki, M. *LabVIEW: Advanced Programming Techniques*; CRC Press: Boca Raton, FL, USA, 2006.

Appendix 2

II.

Carlos-Omar Rasgado-Moreno and Madis Ratassepp. Geodesic equations for guided wave helical path separation for a pipe bend. *Mechanical Systems and Signal Processing*, 204:110820, December 2023



Geodesic equations for guided wave helical path separation for a pipe bend

Carlos-Omar Rasgado-Moreno^{*}, Madis Ratassepp

Department of Civil Engineering and Architecture, Tallinn University of Technology, Ehitajate tee 5, 19086, Tallinn, Estonia

ARTICLE INFO

Communicated by M. Rebillat

Keywords:

Time-reversal
Shortest-path
Helical path separation
Geodesic equations
Pipe bend
Guided waves
Structural health monitoring

ABSTRACT

The sections of pipe bends are susceptible to wall thinning by flow-accelerated corrosion due to the sudden change in the fluid flow direction and velocity. Compared to existing screening approaches, Guided Wave Tomography (GWT) has been demonstrated to provide more accurate information about the defect. In GWT an inversion problem is solved, in which a forward model is used to predict a synthetic dataset for a given physical model. Two-dimensional (2D) forward models are preferred for the inversion scheme due to the feasibility of combining these with tomographic algorithms. Since 2D models resemble the GW propagation of a plate, they do not consider the cyclic nature of the pipe. To overcome this limitation, a robust helical path separation was introduced in Huthwaite and Seher (2015) for a straight pipe. However, it relies on time-reversing the measured wave field $\phi(t)$ as a function of the propagation distance $x_{s,r}$ from the source to the receiver. Although ray-tracing and grid-based methods are capable of computing the distance $x_{s,r}$ for complex geometries such as the pipe bend, they are complex and time-consuming. Hence, in this paper a straight forward approach is proposed to compute $x_{s,r}$ based on the pipe geometry and the geodesic equations of a torus. Then the computed distance $x_{s,r}$ is used for removing the helical path trajectories. Compared to the distance obtained by using the Hilbert envelope, the results show that the geodesic distances preserve the information of the wavefront of interest, including the focusing effect and the scattered wave field from a Hann-shaped defect. The technique is applied to experimental data and demonstrated to separate the wavefront of interest.

1. Introduction

Industrial pipelines are widely used in the energy, oil, and gas industries for transporting highly volatile fluids such as gasoline, natural gas, oil, etc. Nonetheless, pipelines are vulnerable to corrosion and erosion damage [1–3]. In addition, complex sections of pipelines such as fittings, crossings, joints, and bends are most susceptible to developing damage [4]. In particular, pipe bends are susceptible to wall thinning by flow-accelerated corrosion due to the sudden change in the fluid flow direction and velocity [5]. Therefore, locating potential defects and estimating the corrosion rates of complex sections of pipelines is key to guaranteeing the proper operation of any complex industrial asset.

To rapidly inspect long parts of pipelines, ultrasonic guided waves (GWs) have been widely used for inspection in pipelines [6,7]. GWs travel within the wall of a pipe and are capable of covering large distances, being also sensitive to cracks and corrosion [8]. Conventionally, pipeline screening consists of a single transducer array attached to the pipe in a ring form. In this way, the transducer array can send out the required excitation signal and measure the reflections from the potential defects. Numerous researchers

^{*} Corresponding author.

E-mail address: carlos.rasgado@taltech.ee (C.-O. Rasgado-Moreno).

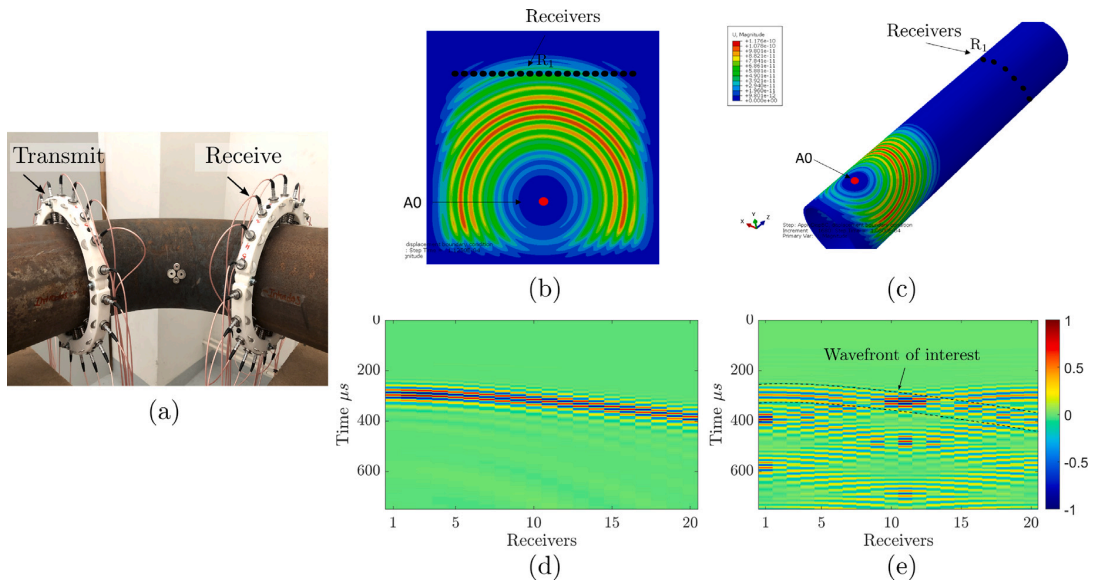


Fig. 1. Guided wave tomography configuration in a pipe bend with two transducer rings (a) and finite element snapshots for the transmission of the A_0 mode in an 8 mm thick plate (b) and pipe (c). A five-cycle tone-burst with a central frequency at 50 kHz modulated by a Hanning window was excited. For both models, absorbing boundaries were considered to avoid reflections with the edges. The excitation point is highlighted by the red point in each of the figures, and 20 equally distributed receivers were placed at 0.681 m from the excitation position represented by black dots. Measured wavefront for a plate (d) and for a straight pipe (e). The observed helical paths are a consequence of the cyclical nature of the pipe geometry. Conventionally, methods of guided wave tomography that offer high precision thickness mapping require only the first arrived wavefront, which is highlighted by dotted lines (e). (For interpretation of the references to color in this figure legend, the reader is referred to the web version of this article.)

have investigated GW propagation in a pipe elbow, which is more complex than a straight pipe owing to the curvature of the bend. In their study, Rose et al. [9] described the natural focusing effect of GWs within a curved pipe and examined the echo waveforms to detect drilling defects. Demma et al. [10], Hayashi et al. [11], and Wu et al. [12] demonstrated that the reflection and transmission of guided waves in the curved section are influenced by mode conversions. Rudd et al. [13] implemented the elastodynamic finite integration technique to investigate GW propagation around bends. Sanderson et al. [14] proposed an analytical approach to analyze GW propagation in the bend and focused on the transmission of the $T(0,1)$ mode. Wu et al. [15] implemented the normal-mode expansion method to study the reflection and mode conversion of the $L(0,1)$ mode. Heinlein et al. [16] examined the reflection of the $T(0,1)$ mode from cracks present in a curved section. Xu et al. [17] investigated the correlation between the amplitude of GW reflection and the bend angle, utilizing a guided wave denoising method. Nonetheless, the current screening methods for characterizing defects in curved sections have a major drawback: they are unable to locate and determine the size of the defect [9–11,16], preventing accurate mapping of its profile or effective monitoring of its progression.

In contrast, more accurate information about the defect can be achieved by combining the transducers arrays used in ordinary screening with tomographic techniques. In guided wave tomography (GWT), two transducer rings are attached to the pipe instead of one, in order to obtain a set of measurements from different angles. GWT works under the principle of solving an inverse problem that uses a forward model to predict a synthetic data set for a given physical model. The defect is calculated iteratively by minimizing the residuals between the true and synthetic measurements until the convergence criterion is reached [18]. To date, a number of GWT methods have been introduced to take advantage of the information carried by the helical paths for defects localization and thickness loss mapping in straight pipes. For example, Willey et al. [19] used ray tomography for defects characterization, Golato et al. [20] were able to locate defects using the group sparse reconstruction technique, while Da et al. [21] applied the Semi-analytical Finite Element method to model the helical paths and used the quantitative detection of the Fourier transform approach to successfully reconstruct defects on pipes, and later improved the accuracy by using the integral coefficient updating strategy [22]. Livadiotis et al. [23] modeled the helical paths using the Fast Marching Method and used an algebraic reconstruction algorithm to locate defects while providing some information about their size. In addition, Wang et al. [24] used diffraction tomography based on the Fourier diffraction theorem alongside high excitation frequencies to achieve a high-resolution defect characterization, and Zhu et al. [25] used the reconstruction algorithm for the probability inspection of damage in straight pipes. A standard GWT setup is illustrated in Fig. 1(a). Waves are excited in one ring and the radial displacements are recorded on the other ring. Then, any variation in the recorded wave field can be interpreted by tomographic algorithms as a thickness reduction in a specific location [26].

In general, in GWT a two-dimensional (2D) forward model is preferred over an exact three-dimensional (3D) model for the inversion scheme due to its low computational cost, simplicity and the feasibility of combining with tomographic algorithms. Conventionally, 2D forward models for straight pipes can be represented by a periodic unwrapped pipe [27]. To illustrate this

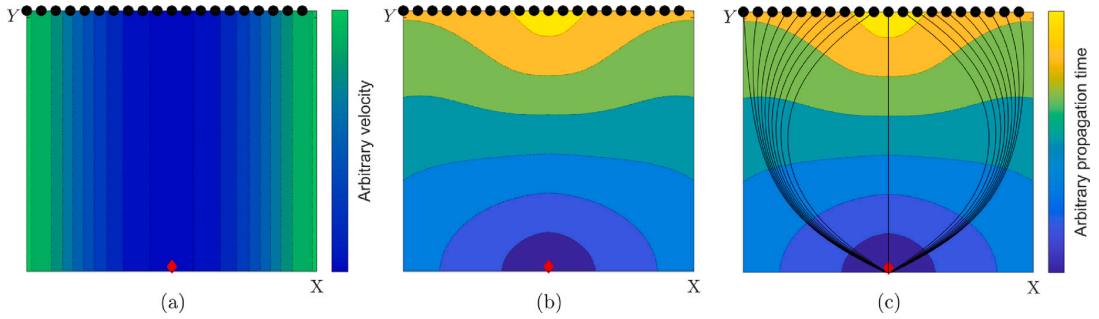


Fig. 2. Conventional steps to find the ray paths in a layered medium. Phase velocity distribution $v(x)$ for a hypothetical 8 mm thick steel plate (a), similar to the circumferential velocity distribution in a pipe bend. The arrival time of the wave field is computed at each point of the domain (b), then a gradient descent method is performed to find the shortest-paths from the excitation source highlighted in red and 20 equally distributed receivers (c). (For interpretation of the references to color in this figure legend, the reader is referred to the web version of this article.)

concept, Fig. 1(b) and (c), show the finite element modeling for the transmission of the A_0 mode for an 8 mm thick steel plate and straight pipe respectively. Fig. 1(d) shows the recorded wave field of the plate model from Fig. 1(b). In contrast, for the straight pipe case, a set of helical paths exist between the source and receivers due to the cyclic nature of the pipe geometry. As a result, these paths will be superposed in the measured wave field, as illustrated in Fig. 1(e). On the other hand, if the full signal of the single direct wave from Fig. 1(e), which is highlighted by dotted lines, can be extracted, a wide range of highly precise GWT techniques can be directly utilized in the pipe environment, such as the hybrid algorithm for robust breast ultrasound tomography (HARBUT) algorithm [28] and full waveform inversion [29].

To date, two methods for helical path separation have been reported, Robust Helical Path Separation [30] and a dictionary-reconstruction approach for separating helical-guided waves [31]. However, for both methods it is required to know the propagation distance $x_{s,r}$ from the source s to the receiver r , which is the shortest path between s and r [32]. Similarly, for most of the reconstruction algorithms previously introduced, $x_{s,r}$ is also required.

In a traditional transducer-array set-up for a rod, plate or a straight pipe, the distance $x_{s,r}$ is intuitively a straight line [33,34]. However, for more complex geometries such as a pipe bend, the shortest path between s and r will be given by a geodesic. Hence the complexity of using most of the GWT methods or any helical path separation method for removing the helical paths increases due to the need to compute the shortest path between the source and receiver.

In the context of GW propagation, 2D approaches based on ray-tracing and grid-based methods have been used for finding the trajectory between two arbitrary points of more complex mediums like a pipe bend. Volker and van Zon [35] used ray tracing for guided wave tomography in the bend. Similarly, Brath et al. [36] used the shortest-path ray tracing method to find the ray paths traveling around the bend and combined it with a tomographic algorithm [37], Wang and Li [38] used the fast marching method, and Rasgado et al. [39] modeled the guided wave propagation in a pipe bend using the finite difference method for a transversely isotropic medium.

However, for the above-mentioned methods, prior knowledge of a suitable 2D model is needed, since GW propagation in the bend is anisotropic due to the bend's curvature [36]; then, the ray paths can be obtained *a posteriori* by following the travel time gradient [40]. To illustrate this point, consider a layered medium in the form of an 8 mm thick steel plate with dimensions $X \times Y$ with a hypothetical phase velocity distribution $v(x) = v_0\alpha(x)$, as shown in Fig. 2(a), where v_0 is the phase velocity of an arbitrary dispersive mode at a given central frequency and $\alpha(x)$ a non-dimensional parameter that characterizes the inhomogeneity of the sound-speed field in the plate, which resembles the circumferential velocity variation in a pipe bend [36]. The source is located at $(X/2, 0)$ highlighted in red and 20 equally distributed receivers were placed in between $(0, Y)$ and (X, Y) . First, the velocity field in the domain is computed using the fast marching method [41], as shown in Fig. 2(b). Then, the ray trajectories are obtained by following the traveled time gradient from each receiver to the source, as shown in Fig. 2(c).

Although ray-tracing and grid-based methods are able to provide the arrival time of the wavefront across the domain, they are complex and time-consuming just for computing the traveled distance $x_{s,r}$ between the source and the receiver that is needed, e.g., for time-reversing the signals in the robust helical path separation algorithm [30]. However, a pipe bend geometry is analogous to a torus, so the ray paths in the bend can be simply obtained by solving numerically the geodesic equations, making it suitable to combine these with tomographic or helical path separation algorithms that require the propagation distance of the helical paths. Hence, in this paper a straightforward approach is proposed to compute $x_{s,r}$ based on the geodesic equations of a torus, which only needs information about the bend geometry rather than its acoustic wave field, and the first arriving wave packets are extracted using robust helical path separation [30].

This paper is structured as follows. First the geodesic equations, the shortest path algorithm using the geodesic equations, the helical path separation algorithm for the bend and the Finite Element simulation tools are described in Section 2. Secondly, in Section 3 a numerical study is carried out to compare the performance of the helical path separation algorithm when using the geodesic equations and the Hilbert transform to compute the distance from the source to the receivers. Additionally, the scattered wave field from a Hann-shaped defect is studied after the helical path separation. The helical path separation algorithm based on the geodesic equations is validated with experimental data in Section 4, and concluding remarks are listed in Section 5.

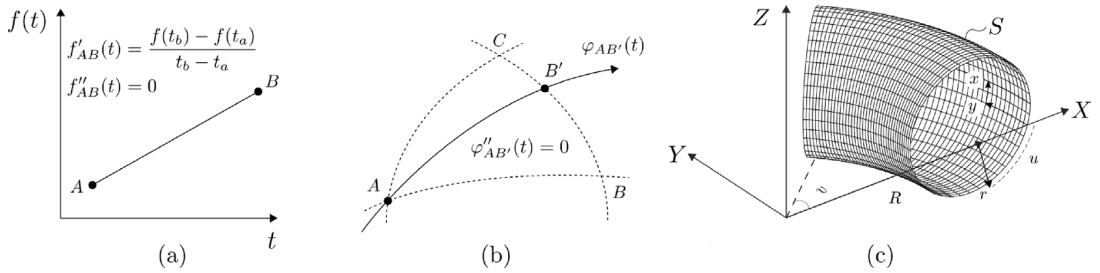


Fig. 3. In (a) the shortest path between the points A and B is the straight line $f_{AB}(t)$, with $f''_{AB}(t) = 0$. In (b), where the arbitrary surface S is defined by the vertices A, B, C , the geodesic $\varphi_{AB'}(t)$ is the shortest path between A and B' with $\varphi'_{AB'}(t) = 0$. In (c), the torus section S represents the bend of a pipe in the 3D domain.

2. Numerical methods

2.1. Geodesic equations of a torus

To introduce the geodesic equations, consider two arbitrary points A and B in the plane, as shown in Fig. 3(a). The shortest distance between A and B is the straight line $f_{AB}(t)$ that crosses the two points, where $f(t)$ is the position in the plane as a function of time t . In this context, the first derivative $f'_{AB}(t)$ will indicate the slope of the straight line $f_{AB}(t)$ or the velocity, which is constant. As a result, the acceleration of a particle moving in $f_{AB}(t)$ will be zero $f''_{AB}(t) = 0$. In other words, the shortest path between A and B is given by a particle traveling at constant speed in a plane.

Likewise, a curve $\varphi(t)$ in a geometric surface S is a geodesic when its acceleration is zero $\varphi''(t) = 0$ or perpendicular to the tangent plane of the surface at the point $\varphi(t)$ [42]. To exemplify this, in Fig. 3(b) let A, B and C be the vertices of a triangle on a surface S . The shortest distance between A and B' is given by the curve $\varphi_{AB'}(t)$, where $\varphi_{AB'}(t)$ is the position in the surface S as a function of time t .

Conventionally, the geodesic equations of a parametric surface $S(u(t), v(t))$ with $u(t)$ and $v(t)$ being the circumferential and longitudinal positions, respectively, as a function of time t , are written as follows [43]:

$$\begin{aligned} \ddot{u} + \frac{E_u}{2E} \dot{u}^2 + \frac{E_v}{E} \dot{u}\dot{v} - \frac{G_u}{2E} \dot{v}^2 &= 0 \\ \ddot{v} + \frac{E_v}{G} \dot{u}^2 + \frac{G_u}{G} \dot{u}\dot{v} + \frac{G_v}{2G} \dot{v}^2 &= 0, \end{aligned} \tag{1}$$

with

$$\begin{aligned} E &= S_u S_u & E_u &= 2S_{uu} S_u \\ F &= S_u S_v & E_v &= 2S_{uv} S_{uv} \\ G &= S_v S_v & G_u &= 2S_{uv} S_v \\ & & G_v &= 2S_{vv} S_v, \end{aligned} \tag{2}$$

where the top superscripts $\dot{\cdot}$ and $\ddot{\cdot}$ indicates the first and second derivatives with respect to time, and the subscripts u , and v indicate the derivatives with respect to positions u and v .

Consider the torus section from Fig. 3(c) defined in the 3D domain, with the mid-thickness or central radius r , bend radius R , torus azimuth longitude v around the Z -axis and torus latitude u with respect to the plane XZ . Substituting the parametric torus surface $S(u, v) = \{(R + r \cos(u)) \cos(v), (R + r \cos(u)) \sin(v), r \sin(u)\}$ into (1), and after some algebraic manipulation, the geodesic equations for the torus can be expressed as a system of ordinary differential equations [44]:

$$\begin{aligned} \dot{\varphi}_1 &= \varphi_2 \\ \dot{\varphi}_2 &= -\frac{1}{r} \sin(\varphi_1)(R + r \cos(\varphi_1))\varphi_4^2 \\ \dot{\varphi}_3 &= \varphi_4 \\ \dot{\varphi}_4 &= \frac{2r \sin(\varphi_1)}{R + r \cos(\varphi_1)} \varphi_2 \varphi_4, \end{aligned} \tag{3}$$

with $\varphi_1 = u, \varphi_2 = \dot{u}, \varphi_3 = v, \varphi_4 = \dot{v}$.

2.2. Shortest path using the geodesic equations

The principle of the shortest path algorithm is illustrated in Fig. 4, with the first row being the flow diagram of the algorithm (Fig. 4(a)), the second a 3D representation of the steps (Fig. 4(b)–(d)), and the third one a 2D representation as a function of the

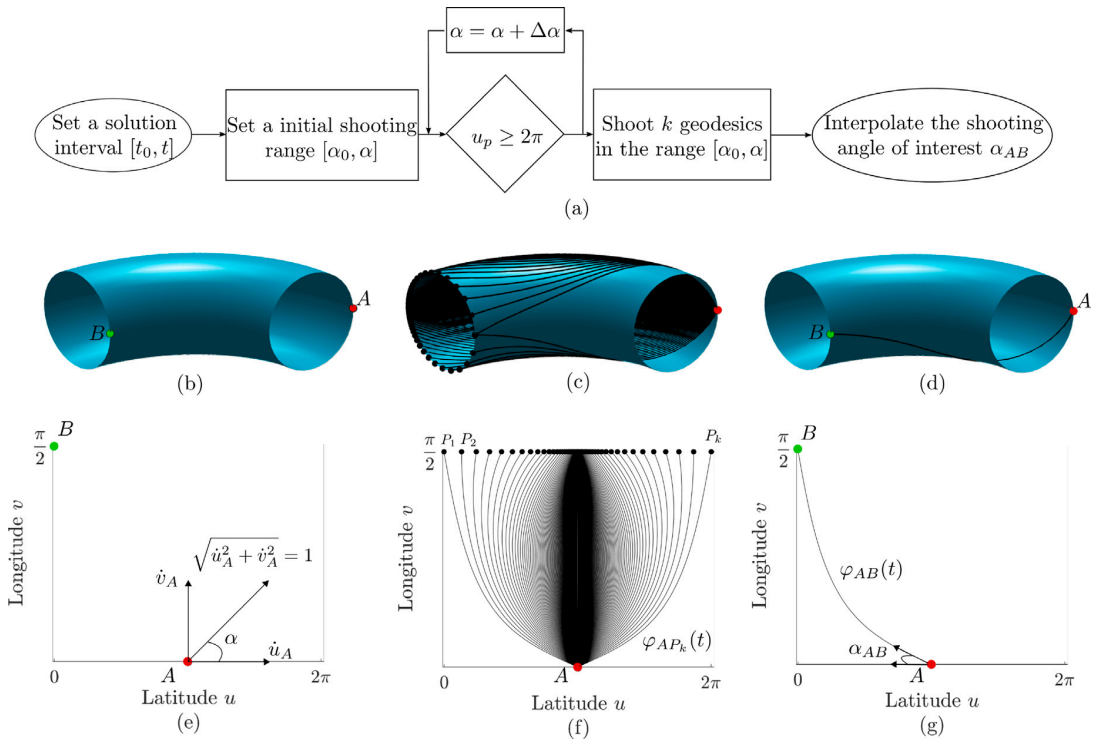


Fig. 4. Structure of the shortest path algorithm using the geodesic equations (a) with 3D and 2D representations of the steps in (b)–(d) and (e)–(g), respectively. In (b) and (e) the initial velocity components u_A, v_A indicate the initial direction α_{AP} of the geodesic path φ_{AP} . In (c) and (f) k geodesics are computed in $[\alpha_0, \alpha]$ with ending point coordinates $P_k(u_{P_k}, \pi/2)$. Finally, in (d) and (g), the shooting angle α_{AB} that traces φ_{AB} can be interpolated as a function of the circumferential positions of u_p .

longitudinal and circumferential positions u, v (Fig. 4(e)–(g)). Refer to the arbitrary points A and B in the torus section in Fig. 4(b). In order to find the geodesic $\varphi_{AB}(t)$, the following shortest path algorithm is proposed.

First, consider the initial conditions $u_0, v_0, \dot{u}_0, \dot{v}_0$. The initial position u_0, v_0 corresponds to the point A that is (u_A, v_A) . The velocity components \dot{u}_A, \dot{v}_A determine the direction of the geodesic path $\varphi_{AP}(t)$. The subscript AP refers to a geodesic path between the initial position A and any arbitrary end point P , as illustrated in Fig. 4(c). For the sake of simplicity, it can be assumed that the velocity $\dot{\varphi}_{AP}(t) = 1$, so that $\sqrt{\dot{u}_a^2 + \dot{v}_a^2} = 1$. This principle is illustrated in Fig. 4(e). As a result, the geodesic traveled distance will be equal to its traveled time $d_{AP} = t_{AP}$. In this way, the interval $[t_0, t]$ for computing the geodesic path $\varphi_{AP}(t)$ can be selected so that it does not extend farther than the longitude of interest. For a torus with the azimuth longitude of $v_B = \pi/2$, the time $t = 3\pi(R + r)/4$ is sufficient for mapping the longitude interval of interest $[0, \pi/2]$.

Secondly, the initial direction of the geodesic can be expressed in terms of a shooting angle α , with $\tan(\alpha) = \dot{u}_A/\dot{v}_A$, as in Fig. 4(e). Although for practical applications the shooting angle α_{AB} that traces the shortest path $\varphi_{AB}(t)$ between A and B is most likely to be unknown, the shooting angle range $[\alpha_0, \alpha]$ that contains α_{AB} , can be found by iteratively increasing α by $\Delta\alpha$ and solving Eq. (3) until the circumferential position of interest is reached, $u_p \geq u_B$. Then, a given number of k geodesics, $\varphi_{AP}(t)$, can be computed in the shooting angle window $[\alpha_0, \alpha]$.

It should be noted that the accuracy of the circumferential position u_B will depend on k . To illustrate this point, see Fig. 4(f). Due to a conservative number of k -geodesics, in Fig. 4(f) it is observed that the number of geodesics close to the longest meridian or *extrados* position (center of the figure) is denser than the shortest meridian or *intrados* (edges of the figure). Consequently, there is less information about the geodesics paths close to the edges, so k should be chosen so that it covers most of the points around the circumferential direction.

Finally, the computed paths can be restricted to the longitude interval of interest, in this case $[0, \pi/2]$, so that $v_p = v_B = \pi/2$. At this point, any shooting angle α leads to a geodesic ending at $(u_p, \pi/2)$. Since all the end points P have the same longitude coordinate v_B , the shooting angle α_{AB} that traces the geodesic path $\varphi_{AB}(t)$ can be interpolated as a function of the already computed circumferential positions u_p and their respective shooting angles α_{AP} . In other words, the algorithm consists of building a data set of ending points P which are located at the longitude v_B , to interpolate the shooting angle α_{AB} as a function of the circumferential position of interest u_{AB} . The 3D and 2D representation of $\varphi_{AB}(t)$ is illustrated in Fig. 4(d) and (g), respectively. To sum up:

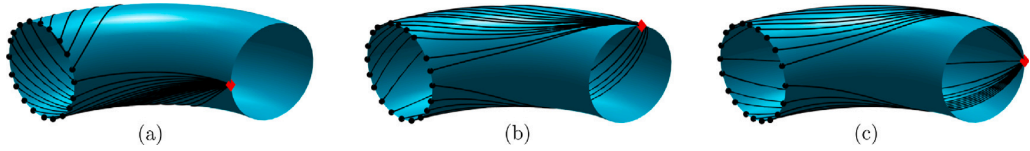


Fig. 5. Shortest paths between three different starting points: intrados (a), top (b) and extrados (c); and 20 equally distributed monitoring points around the torus latitude.

1. Set the initial conditions for an initial point A in a shooting range $[\alpha_0, \alpha]$.
2. Compute k number of geodesics $\varphi_{AP}(t)$ by solving numerically Eq. (3) in a given time interval $[t_0, t]$ and shooting angle window $[\alpha_0, \alpha]$. In addition, t should be chosen so that $\varphi_{AP}(t)$ is contained in the longitudinal interval of interest $[v_A, v_B]$ and therefore $v_p = v_B$.
3. Interpolate the shooting angle α_{AB} that traces the path of interest $\varphi_{AB}(t)$, as a function of the circumferential position of interest u_{AB} .

In the context of structural health monitoring and guided wave propagation, the above-mentioned algorithm can be extended to find the shortest path between any transducer-array configuration. Fig. 5 shows three excitation points in the bend: intrados (a), top (b) and extrados (c); and their shortest paths for 20 equally distributed monitoring points. In addition, the traveled distance x_{AB} can be obtained by a simple numerical integration of the geodesic path $\varphi_{AB}(t)$. Besides doing a time-reversal of the recorded wave field, it will also be possible to compute the time of flight (TOF) for a given mode, e.g., A_0 by $\text{TOF}_{AB} = x_{AB}/c_g$, where c_g is the group velocity of the excited mode.

2.3. Helical path separation algorithm for a pipe bend

To extract the first wave-packet arriving at the receivers, the robust helical path separation algorithm developed in [30] is used in this paper. The steps of the algorithm are briefly described as follows:

1. Time traces $\phi_{r,s}^{(1,1)}(t)$ from the source s to receiver r are replicated m times, $\phi_{r+Nm,s}^{(2,1)}(t)$, where N is the number of sources and m the replica number, so Nm represents the jump in each receiving transducer number, and the superscript (p, j) indicates the p th stage of the algorithm for the j th iteration. In the configuration considered in this work $M = 5$ and $N = 20$; see Fig. 6(a).
2. The replicated time traces $\phi_{r,s}^{(2,1)}(t)$ are time-reversed to align the central waveform:

$$\phi_{r,s}^{(3,1)}(\omega) = \text{FFT} \left(\phi_{r,s}^{(2,1)}(t) \right) \exp[-ik(\omega)x_{r,s}], \quad (4)$$

where $\phi_{r,s}(\omega)$ represents the signal in the frequency domain, $k(\omega)$ is the wave number for each frequency ω and $x_{r,s}$ is the distance from the receiver to the source. Subsequently, an inverse Fast Fourier Transform is applied to obtain the time-reversed traces $\phi_{r,s}^{(3,1)}(t)$, see Fig. 6(b). Furthermore, $\phi_{r,s}^{(3,1)}(t)$ is windowed to remove the majority of unwanted modes, as shown in Fig. 6(c). As a result, the signal of interest $\phi_{r,s}^{(4,1)}(t)$ is obtained.

3. A 2D Fast Fourier Transform (2D-FFT) is applied in the receiver direction,

$$\phi_s^{(4,1)}(k_\theta, \omega) = \mathfrak{D} \left\{ \phi_{r,s}^{(4,1)}(t) \right\} \quad (5)$$

where \mathfrak{D} represents the 2D-FFT operator and k_θ the circumferential wavenumber. Note that, since the 2D-FFT is applied in the receiver direction, the receiver subscript r is removed. Then

$$\phi_s^{(5,1)}(k_\theta, \omega) = \begin{cases} \phi_s^{(4,1)}(k_\theta, \omega) & |q| \leq G, \\ 0 & |q| > G \end{cases} \quad (6)$$

where q defines the circumferential wavenumber component and G the limit of the circumferential wavenumber components selected, and an inverse 2D-FFT is applied to $\phi_s^{(5,1)}(k_\theta, \omega)$, to bring them to the previous time-reversed step $\phi_{r,s}^{(5,1)}(t)$. At the first iteration $G = 1$ was used to select just the first component from the helical paths, as shown Fig. 6(d), and the cleaned time traces are forward-propagated, as shown in Fig. 6(e):

$$\phi_{r,s}^{(6,1)}(\omega) = \text{FFT} \left(\phi_{r,s}^{(5,1)}(t) \right) \exp[ik(\omega)x_{r,s}]. \quad (7)$$

4. The central replica is cleaned up by minimizing the waveforms belonging to other replicas. In Fig. 6(f), the extracted waveform from Fig. 6(e) has been translated horizontally and subtracted from all the helical modes in Fig. 6(a), while avoiding the central mode. Mathematically, this is represented as

$$\phi_{r,s}^{(7,1)}(t) = \phi_{r,s}^{(1,1)}(t) - \phi_{r+Nm,s}^{(6,1)}(t). \quad (8)$$

5. The previous steps (2–5) are repeated for other circumferential wavenumber components $G = 2, 3, 4, 5$.

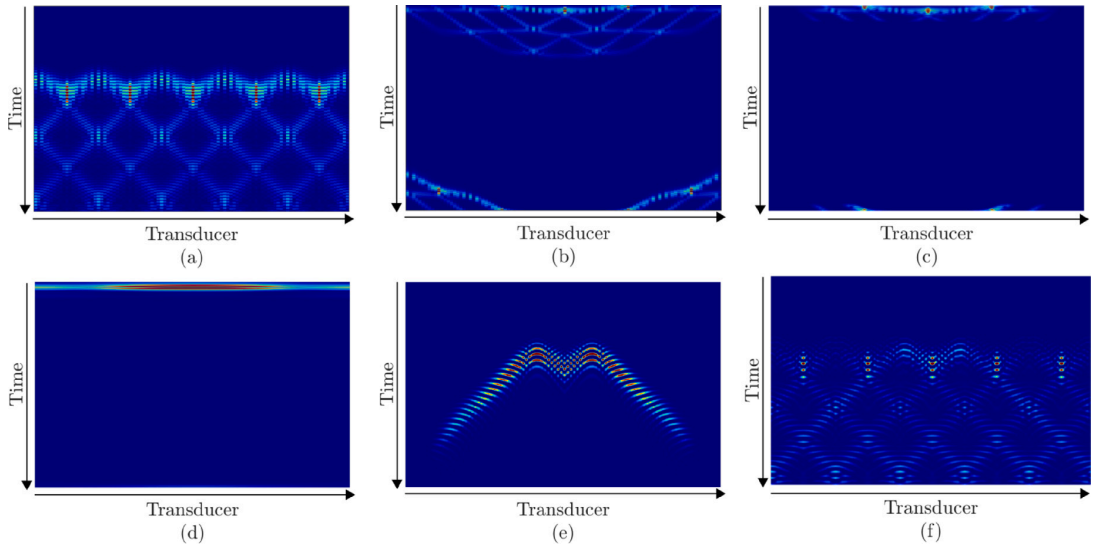


Fig. 6. Stages for one iteration of the helical path separation algorithm according to [30]. Here, $N = 20$ and $M = 5$. These are simulated data from a finite element model of the pipe bend setup described in Section 2.4. First, (a) shows the recorded signals across the receiving transducers when exciting on the extrados position, which are replicated 5 times. Secondly, the recorded signals are time-reversed in (b) so that the first waveform is aligned. Then, in (c), a window is applied to remove the majority of unwanted helical paths. In (d), a 2D-FFT transform has been applied to filter higher-order modes. Afterwards, the cleaned waveform is forward-propagated as shown in (e). In stage (f), the cleaned signals from (e) have been translated horizontally and subtracted from all the helical modes in (a), while avoiding the central mode. Finally, the cleaned waveform can be used for the next iteration, where more 2D-FFT components can be included.

6. Finally, a tighter window is applied to leave only the first arrival.

For the first step of the helical separation algorithm, it is required to copy the recorded wave field or replica 0, M times. Secondly, the signals to the virtual receivers' position are time-reversed using Eq. (4), where, $\phi_{\bar{r},s}^{(2,1)}(t)$ is the replicated wave field recorded for the bend, $k(\omega)$ is the wave number, which can be extracted from the dispersion curves, and $x_{\bar{r},s}$ the distance traveled from the source to the receivers. For a straight pipe, [19] introduced a formula to find $x_{\bar{r},s}$ for M number of replicas. However, for the pipe bend this formula cannot be directly used. Since the distance $x_{\bar{r},s}$ is likely to be unknown, the most common approach would be to compute as a function of the TOF $t_{\bar{r},s}$, so $x_{\bar{r},s} = c_g t_{\bar{r},s}$, where c_g is the group velocity of the excited mode and $t_{\bar{r},s}$ is the TOF from the source s to the receiver r . For a recorded wave field, the TOF $t_{\bar{r},s}$ can be computed by taking the difference between the Hilbert envelope of the input and the measured signal [18].

In contrast, the shortest path algorithm from Section 2.2 can be followed to compute the geodesics' paths from the source to the receivers $\varphi_{\bar{r},s}(t)$. Then the distance $x_{\bar{r},s}$ can be found simply by integrating $\varphi_{\bar{r},s}(t)$, and the wave field can be time-reversed.

In this paper, the geodesic and Hilbert distances $x_{\bar{r},s}^g$ and $x_{\bar{r},s}^h$ were used separately for the helical path separation algorithm. To compute $\varphi(t)_{\bar{r},s}$, the function `ode45` from MATLAB software [45] was used to solve the system of differential equations expressed in Eq. (3). The shooting angle window was found for each excitation point with $\Delta\alpha = 0.01$ and 500 geodesics were computed for each replica. The computational time for computing 2500 geodesics and interpolating the 100 paths of interest, using the parallel for loop `parfor` in MATLAB, was 4.05 s. Then the distance $x_{\bar{r},s}^g$ was found by numerically integrating the path $\varphi(t)_{\bar{r},s}$. On the other hand, since the helical paths overlap with the first arrivals in most of the recorded wave fields, the times of flight for computing $x_{\bar{r},s}^h$ were selected manually.

2.4. FE modeling

The pipe bend specimen used to demonstrate the effectiveness of the geodesics' shortest path algorithm alongside the helical path separation, consisted of a steel pipe specimen with inner radius $r_{in} = 0.1015$ m, outer radius $r_{out} = 0.1095$ m, a 90 degree bend with radius $R = 0.329$ m, and two straight pipe sections at the beginning and at the end of the bend each 0.20 m long, which were included in the 3D Finite Element (FE) model. Two separate FE models, with and without a defect, were defined to study the scattered wave field from the defect after the helical path separation. Further details about the pipe bend specimen, FE parameters, and defect characterization are described in [39].

ABAQUS Explicit software was used [46] for the 3D guided wave propagation simulations in the pipe bend. The FE model consisted of 560 elements along the circumference of the pipe, 6 elements along the thickness, and 550 elements along the 90 degree rotation, or axial direction. The eight-node brick element type C3D8R was used. Additionally, absorbing regions were defined at the edges of the bend, in order to avoid reflections from the boundaries [47].

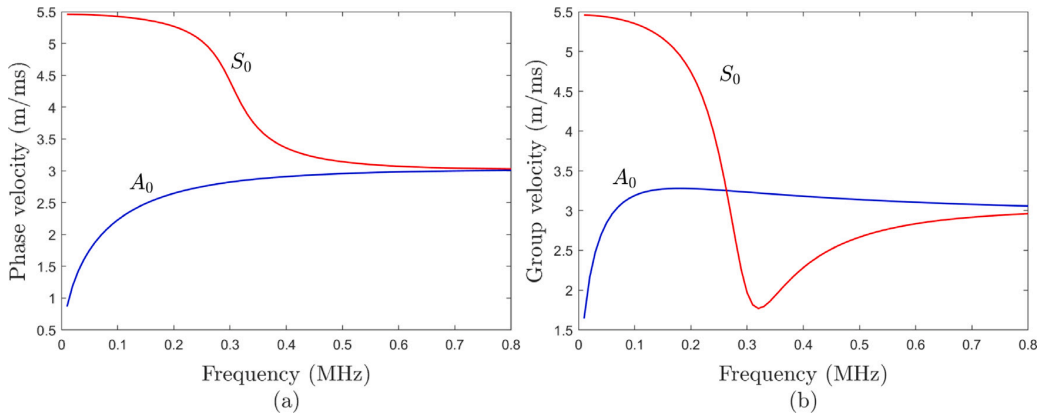


Fig. 7. Dispersion curves for the fundamental symmetric S_0 and antisymmetric A_0 modes in a 8 mm thick steel plate. (a) and (b) present phase and group velocity, respectively, as a function of frequency. The high dispersion is often exploited by GWT. The phase and group velocities are influenced by the frequency–thickness product. Thus, when the frequency remains constant, altering the thickness leads to a predictable variation in velocity. Therefore, if a reconstruction of velocity is produced, this can subsequently be converted back to thickness.

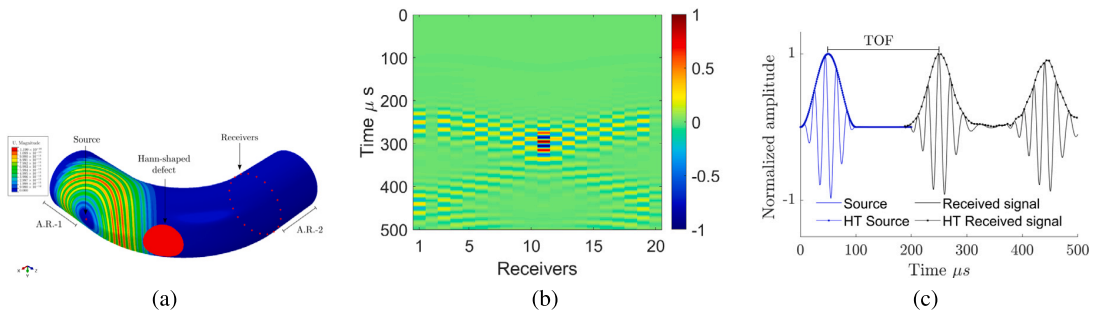


Fig. 8. Pipe bend geometry computed in ABAQUS when exciting on the *extrados* position with a Hann-shaped defect, element type C3D8R, absorbing region (A.R.) 1 and 2 is shown in (a). In (b) the normalized radial displacements measured for 500 μ s are shown, and in (c) the TOF is obtained by taking the difference between the peaks of the Hilbert envelope of the input and measured signal.

Three source positions were excited separately on one side of the bend at the intrados, top, and extrados. The A_0 mode was excited by applying an out-of-plane force in the radial direction. It is believed that the sensitivity of low frequency A_0 to thickness variations is higher to S_0 [48]. Then, the radial displacement components were measured by 20 equally distributed monitoring points placed at the end of the bend. Dispersion curves for an 8 mm thick steel plate are shown in Fig. 7, where the phase and group velocities are a function of the frequency in Fig. 7(a) and (b), respectively. Moreover, in Fig. 7 it is observed that the A_0 mode is highly dispersive at low frequencies. For the excitation, a five-cycle tone-burst with a central frequency at 50 kHz modulated by a Hanning window was excited.

In addition, a Hann-shaped defect 120 mm wide and with a maximum 30% of thickness reduction, was placed in the center of the pipe along the extrados position to study the scattered wave field of the separated wave fields using the geodesic $x_{F,S}^g$ and Hilbert $x_{F,S}^h$ distances. The scattered wave field was obtained by a simple baseline subtraction of the wave fields with and without a defect. A sample of the pipe bend geometry computed in ABAQUS for the extrados case with a Hann-shaped defect is shown in Fig. 8(a) and the measured wave field in Fig. 8(b). The TOF $t_{F,S}^h$ to compute $x_{F,S}^h$ was obtained by taking the difference between the peaks of the Hilbert envelope of the input and measured signal, as illustrated in Fig. 8(c).

3. Numerical analysis

3.1. Helical path separation

To extract the wavefront of interest required for GWT, the first step of the helical path separation algorithm requires the recorded wave field to be replicated, as illustrated in Fig. 9(a)–(c) when the excitation source is at the intrados, top and extrados, respectively. The recorded wave fields were replicated 5 times, with a total of 100 virtual receiving transducers, and the wavefront of interest for each case has been highlighted with dashed lines. From Fig. 9, it can be observed that the TOF based on the Hilbert cannot

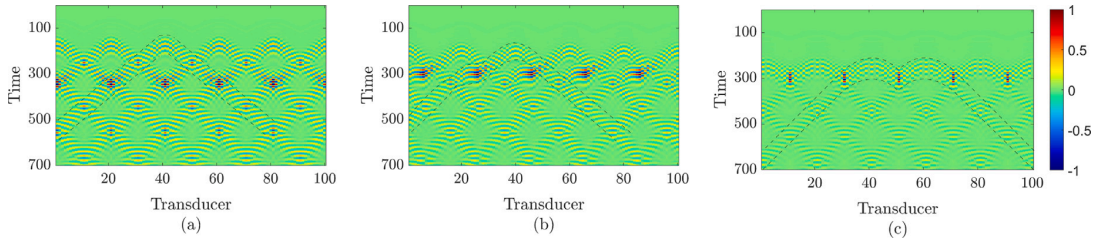


Fig. 9. Replicated wave fields when the excitation source is located at the intrados (a), top (b) and extrados (c). The recorded wave fields were replicated 5 times, with a total of 100 virtual receiving transducers and the wavefront of interest for each case is highlighted with dashed lines. The TOF based on the Hilbert transform for computing the distance $x_{r,s}^h$ cannot be selected accurately due to the crossing of the helical paths with the wavefront of interest.

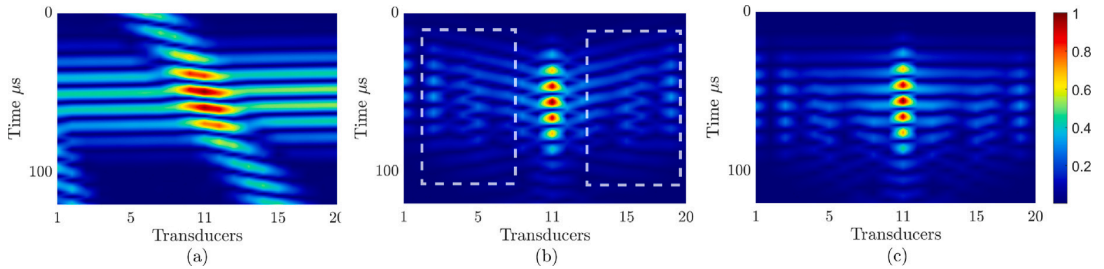


Fig. 10. Second step of the helical path separation algorithm. Time-reversed wave field for a straight pipe (a), and for the pipe bend using the Hilbert distances $x_{r,s}^h$ (b), and the geodesics distances $x_{r,s}^g$ (c). An aligned wave field should be expected when time-reversing the signals. Amplitudes are normalized.

be selected accurately when there is a crossing on the helical paths. Additionally, the natural dispersion of the guided wave might induce additional errors for estimating the TOF. As a result, the Hilbert distance $x_{r,s}^h$ will carry an uncountable error due to the helical path crossing and guided wave dispersion.

The above-mentioned error in $x_{r,s}^h$ becomes visible when time-reversing the wave field in the second step of the helical path separation algorithm. Fig. 10 shows the second step of the helical path separation algorithm when the excitation source is located at the extrados position. The aim of this step is to align the first arrivals so that the helical paths can be easily removed in further steps. To illustrate this point, Fig. 10(a) shows the ideal time-reversed wave field for a straight pipe with similar characteristics to the above-described pipe bend, where the wave field is clearly aligned and the energy is distributed homogeneously along the transducers. Similarly, when using the Hilbert distances $x_{r,s}^h$ in Fig. 10(b), the wave field is not smoothly aligned after the time-reversal due to the above-mentioned errors when computing $x_{r,s}^h$. The areas where the time-reversed wave field is more inconsistent are highlighted with dashed lines. In contrast, Fig. 10(c) shows the time-reversed wave field for the bend specimen when using the geodesic distances $x_{r,s}^g$. The high contrast in the wave field energy is a consequence of the focusing effect previously reported by [36]; however, the reversed wave field is aligned.

Afterwards, steps 3–6 from the helical separation algorithm can be performed with similar parameters as for the straight-pipe case in [30]. Results for the computed geodesics $\varphi_{r,s}(t)$ and the helical path separation using the geodesics and Hilbert distances are shown in Fig. 11. Fig. 11(a) shows the geodesic paths $\varphi_{r,s}(t)$ for the central replica (replica 0) and 2 additional replicas on both sides when exciting on the intrados. In addition, the separated wave fields when using $x_{r,s}^h$ and $x_{r,s}^g$ are shown in Fig. 11(b) and Fig. 11(c), respectively. Similarly, geodesic paths $\varphi_{r,s}(t)$ and separated wave fields are shown for the top Fig. 11(d) to (f), and extrados positions Fig. 11(g) to (i).

It can be seen from Fig. 11(b) and (e) that using the Hilbert distance $x_{r,s}^h$ for time-reversing the wave field leads to additional artifacts after the helical path separation, where the most remarkable artifacts have been circled. Furthermore, the energy of the wave field is not preserved accordingly. Since the wave field is not smoothly aligned, the selected windows will not be able to exclusively keep the wave field of interest. Instead, information belonging to other helical paths will remain. In Fig. 11(e), the circled area shows that the focusing effect from higher helical paths is not removed completely.

In contrast, the helical path separation algorithm performed as expected when using the geodesic distances $x_{r,s}^g$. In Fig. 11(c), most of the artifacts have vanished. The remaining artifacts are related to the helical path separation algorithm, which relies on minimizing higher-order helical paths without removing the wavefront of interest. Similar artifacts are observed for a straight pipe [30]. In addition, the focusing effect is well preserved in the central replica; see for example Fig. 11(f).

Moreover, the geodesic paths $\varphi_{r,s}(t)$ help to understand the focusing effect on the recorded wave fields. For example, in Fig. 11(g), when the source is located at the extrados position, a gap is observed at the center of replica 0. This phenomenon is a consequence of the geodesic paths being denser close to the extrados position. Therefore, the density of the geodesic paths $\varphi_{r,s}(t)$ at specific locations can be translated to the positions where the recorded signal will be stronger, which is the focusing effect.

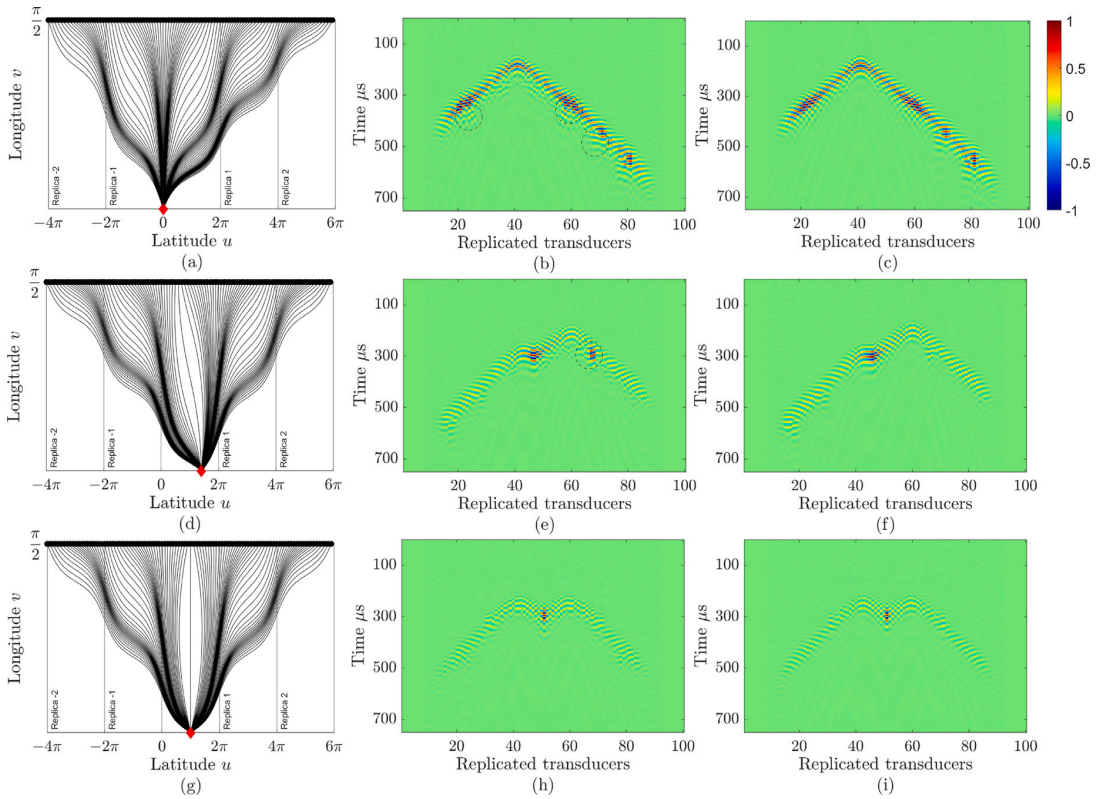


Fig. 11. Replicated wave fields and cleaned wave fields when using the Hilbert distances $x_{F,S}^h$ (second column) and geodesic distances $x_{F,S}^g$ (third column) for three excitation points: intrados (a)–(c), top (d)–(f) and extrados (g)–(i), respectively. Amplitudes are normalized.

3.2. Scattered wave fields

To observe that the information about the defect is preserved after the helical path separation, the scattering of the A_0 mode was investigated. A Hann-shaped thickness reduction of the outer surface was considered. The wave field scattered from the defect when exciting on the extrados position was isolated by subtracting the received waveforms of the intact pipe bend from the waveforms measured in the pipe bend with the defect. The contour plots of the scattered waves from FE and after the helical path separation using $x_{F,S}^h$ and $x_{F,S}^g$ are shown in Fig. 12(a)–(c), respectively. The excitation source was placed at the extrados position and the amplitudes of the waves were normalized by the maximum displacement value of the recorded signals from the intact pipe bend measurements.

In addition, to evaluate quantitatively the scattering information preserved after the helical path separation, the infinity norm was used to compute the residuals between the scatter wavefronts without separation and after separation. The infinity norm $\|S\|_\infty$ of a matrix S is defined as the largest magnitude among each element of S , hence

$$residual = \frac{\|S_{sep} - S\|_\infty}{\|S\|_\infty}, \tag{9}$$

where S_{sep} and S represent the scattered waveform with and without helical path separation, respectively.

Fig. 12(a) shows the original scatter wave field from FE, which includes the helical paths. The additional paths observed between 500 μs and 700 μs correspond to the information about the defect carried by the helical paths. In contrast, when using the Hilbert transform distances $x_{F,S}^h$ in Fig. 11(b), the original shape of the scattered wave field is distorted and a residual of 0.6531 was found. Also, additional artifacts are observed at both sides. This distortion in the scattered wave field from Fig. 11(b) implies that the information of the defect has not been preserved properly, and this will lead to less accurate thickness reconstruction when using a tomographic algorithm. However, when doing the helical path separation with the geodesic distances $x_{F,S}^g$, shown in Fig. 12(c), the scattered wave fields that follow the helical paths are removed and the main scattered field is preserved. In addition, the residual for this case is 0.35, which is 1.8 times less than the previous case. Although a more accurate separation was achieved than in the previous case, the residual will be $residual > 0$ due to the scattering field preserved in the helical trajectories, as it is shown in Fig. 12(a). However, this does not affect the thickness reconstruction, as reported by [30].

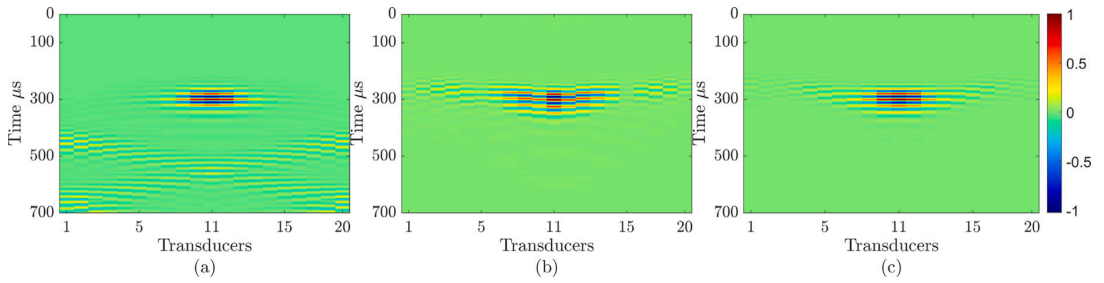


Fig. 12. Scattering plot for a Hann-shaped defect located at the extrados position of the bend, for the original wavefield (a), the separated traces using $x_{r,s}^h$ (b) and $x_{r,s}^g$ (c). Radial displacements were measured and the amplitudes were normalized.



Fig. 13. Experimental setup: (a) measurement setup with transducer arrays A and B with 20 transducers each and an acquisition system; (b) pipe bend with an artificial defect composed of plasticine and located on the extrados position. The experimental pipe dimensions are the same as described in Section 2.4, with the only exception being the straight pipe dimension whose longitudes are 1 m each to avoid reflections with the edges.

Finally, the influence of setting the right distance $x_{r,s}$ when time-reversing the signals is evident. Otherwise, additional artifacts would appear and influence further analysis or signal processing.

4. Experimental validation

A photograph of the experimental configuration used to demonstrate the separation algorithm based on the geodesic equations is shown in Fig. 13. The experimental pipe dimensions are the same as described in Section 2.4, with the only exception that the straight pipe dimensions are 1 m each to avoid reflections with the edges. The measurement setup in Fig. 13(a) consisted of two rings of 20 piezoelectric transducers manufactured by Doppler, Ltd., Guangzhou, China, each with a central frequency of 50 kHz located at each end of the bend, one multiplexer for exciting the desired signal, and a data acquisition box. The transducers were equally distributed along the circumference and they were pressed against the pipe with springs so that the excitation was applied in the radial direction. The excitation waveforms were sent to the data acquisition and the response waveforms were measured, digitally filtered, and logged. Similarly to Section 3, the transmission of the A_0 mode through the bend was investigated for the three excitation points located at the extrados, top, and intrados positions of the bend. Further details about the measurement setup and pipe characteristics are described in [39].

Fig. 14 presents the measured wave fields across 100 replicated transducers when the excitation source is located on the intrados, top and extrados, Fig. 14(a) to (c), respectively. The original measurements, or central replica, correspond to transducers 41–60. The amplitudes of the received waves were normalized by the maximum displacement value of the recorded signals. Some noise around 100 μs , is noticeable, caused by the crosstalk between transducers. In contrast, Fig. 14(d) to (f) show the separated wave fields for each excited location. The separation of the measured wave fields were achieved by the process described in Section 3, when using the geodesic distances $x_{r,s}^g$. First, it is observed that the crosstalk between transducers has been removed; this is a consequence of the windowing applied to the wave fields during the back-propagation step in the helical path separation algorithm. Secondly, in Fig. 14(e) and (f), the focusing effect was preserved at the central replica, and removed from higher-order replicas, confirming that the geodesics distances $x_{r,s}^g$ are robust to experimental uncertainties.

For the scattering study, plasticine was used ($\rho = 1452.3 \text{ kg/m}^3$, $mass = 0.244 \text{ kg}$, $r = 50 \text{ mm}$) and it was attached to the surface of the pipe on the extrados position as shown in Fig. 13(b). The scattered wave fields were obtained by subtracting the measured waveforms of the intact pipe bend from the waveforms in the pipe bend with plasticine. Fig. 15 shows the scattered wave field from the experimental measurements when exciting on the extrados position, the measured wavefronts (Fig. 15(a)) and the separated wavefronts (Fig. 15(b)). In Fig. 15(a) the scattered wave field from the plasticine is observed alongside the noise coming

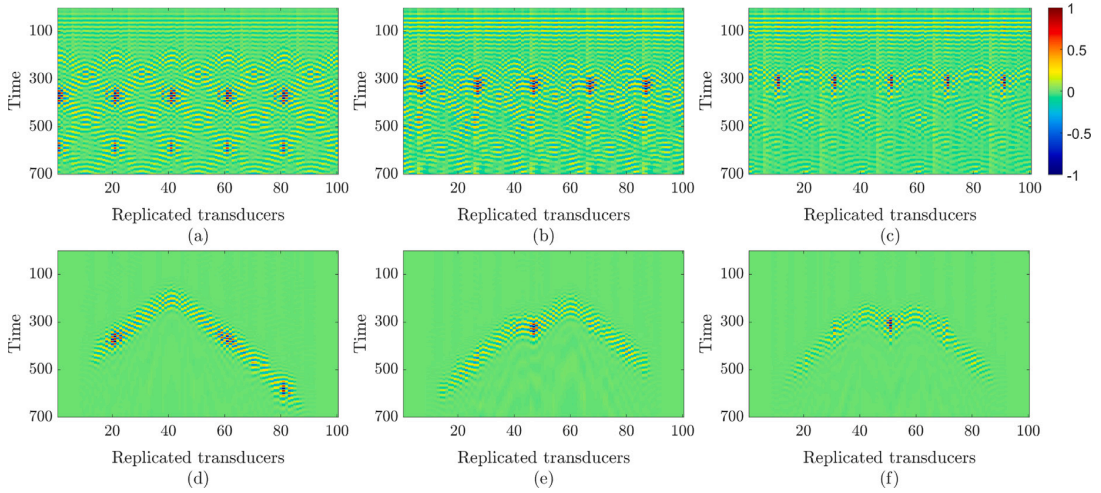


Fig. 14. Experimental wave fields. The A_0 mode was excited with a central frequency of 50 kHz. Measured wave fields replicated 5 times, when exciting on the intrados (a), top (b), and extrados (c); and the extracted wave fields after the helical path separation (d)–(f). After the helical path separation, the noise from the crosstalk is windowed and the focusing effect is preserved.

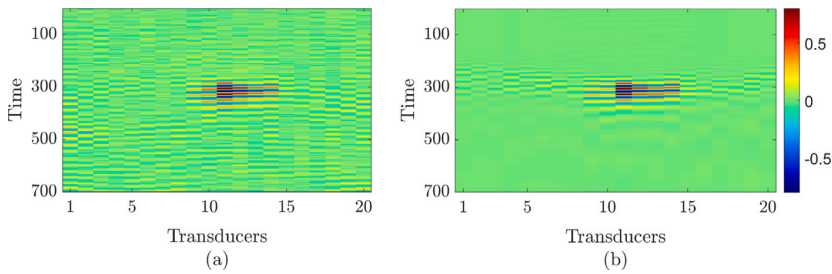


Fig. 15. Experimental scattered wave fields from the original time traces (a) and the separated time traces (b). The scattered wave field produced by the plasticine is preserved after the helical path separation, confirming that the geodesic distances $x_{g,s}^*$ are robust to experimental uncertainties.

from experimental uncertainties such as the crosstalk between transducers, coupling, and transducer mispositioning. In contrast, in Fig. 15(b), where the first wave-packets have been separated, the scattered wave field from the plasticine is preserved with a residual of 0.89; however, a cleaner image was produced from the resulting data regardless of the experimental uncertainties from Fig. 15(a).

5. Conclusion

In this paper, a new method to compute the distances traveled from the source to the receivers in a pipe bend has been introduced. The proposed shortest-path algorithm is based on the geodesic equations of a torus. Compared to the traditional ray-tracing and grid-based methods, the geodesic shortest-path algorithm is a straightforward approach for finding the particle trajectory in a bend, which only requires information about the bend geometry. Additionally, computing the geodesics can contribute to a better understanding of the guided wave propagation in the bend, estimate the arrival times to the receivers and even trace helical paths. For example, the so-called focusing effect can be seen as a consequence of the geodesics being concentrated at a specific location.

The accuracy of the geodesic trajectories was demonstrated for extracting the first arrival of FE-measured wave fields in a pipe bend specimen. Compared to the Hilbert distances, it was shown that the focusing effect and the scattered field were preserved for the separated wave field using the geodesic distances.

Moreover, the method described in Section 3 was applied to experimental test data, separating the wave fields of interest well and enabling a cleaner image from the resulting data. The helical path separation technique was robust to experimental uncertainties, such as crosstalk between transducers and coupling. However, it is necessary to study environmental variations such as temperature and fluid loading.

Finally, the shortest-path algorithm for the bend can be extended to other parametric surfaces, such as the paraboloid, cone, saddle point, etc. Therefore, the application of time-reversal based methods would be possible for more complicated geometries

rather than the conventional plate and pipe. Future work should involve the introduced shortest-path algorithm based on the geodesic equations for damage detection methods involving time-reversal and guided wave tomography.

Funding

This research was funded by the European Union's Horizon 2020 Research and Innovation Program under grant agreement no. 860104, project GW4SHM (Guided Waves for Structural Health Monitoring), and the Estonian Research Council, grant PRG737.

Declaration of competing interest

The authors declare the following financial interests/personal relationships which may be considered as potential competing interests: Madis Ratassepp reports financial support was provided by Estonian Research Council. Madis Ratassepp reports financial support was provided by European Commission.

Data availability

Data will be made available on request.

Acknowledgments

The authors would like to thank Dr. Max Neumann-Coto for his guidance and comments regarding the geodesics equations and Dr. Jing Rao for assisting with the helical path separation algorithm.

References

- [1] M. Talebi, M. Zeinoddini, M. Mo'tamedi, A. Zandi, Collapse of HSLA steel pipes under corrosion exposure and uniaxial inelastic cycling, *J. Construct. Steel Res.* 144 (2018) 253–269, <http://dx.doi.org/10.1016/j.jcsr.2018.02.003>, URL <https://www.sciencedirect.com/science/article/pii/S0143974X17311513>.
- [2] Z. Yan, L. Wang, P. Zhang, W. Sun, Z. Yang, B. Liu, J. Tian, X. Shu, Y. He, G. Liu, Failure analysis of erosion-corrosion of the bend pipe at sewage stripping units, *Eng. Fail. Anal.* 129 (2021) 105675, <http://dx.doi.org/10.1016/j.engfailanal.2021.105675>, URL <https://www.sciencedirect.com/science/article/pii/S1350630721005367>.
- [3] T.-C. Che, H.-F. Duan, P.J. Lee, Transient wave-based methods for anomaly detection in fluid pipes: A review, *Mech. Syst. Signal Process.* 160 (2021) 107874, <http://dx.doi.org/10.1016/j.ymssp.2021.107874>.
- [4] B.G.N. Muthanna, M. A., M.H. Meliani, B. Mettai, Z. B., R. Suleiman, A. Sorour, Inspection of internal erosion-corrosion of elbow pipe in the desalination station, *Eng. Fail. Anal.* 102 (2019) 293–302, <http://dx.doi.org/10.1016/j.engfailanal.2019.04.062>, URL <https://www.sciencedirect.com/science/article/pii/S1350630719302444>.
- [5] Kusmono, Khasani, Analysis of a failed pipe elbow in geothermal production facility, *Case Stud. Eng. Failure Anal.* 9 (2017) 71–77, <http://dx.doi.org/10.1016/j.csefa.2017.08.001>, URL <https://www.sciencedirect.com/science/article/pii/S2213290217300251>.
- [6] D.N. Alleyne, B. Pavlakovic, M.J.S. Lowe, P. Cawley, Rapid, long range inspection of chemical plant pipework using guided waves, in: *AIP Conference Proceedings*, AIP, 2001, <http://dx.doi.org/10.1063/1.1373757>.
- [7] P. Cawley, M. Lowe, D. Alleyne, B. Pavlakovic, P. Wilcox, Practical long range guided wave testing: Applications to pipes and rail, *Mater. Eval.* 61 (2003) 66–74.
- [8] J.L. Rose, *Ultrasonic Waves in Solid Media*, Cambridge University Press, 2003, URL https://www.ebook.de/de/product/4208838/joseph_l_rose_ultrasonic_waves_in_solid_media.html.
- [9] J.L. Rose, L. Zhang, M.J. Avioli, P.J. Mudge, A natural focusing low frequency guided wave experiment for the detection of defects beyond elbows, *J. Pressure Vessel Technol.* 127 (3) (2005) 310–316, <http://dx.doi.org/10.1115/1.1989350>.
- [10] A. Demma, P. Cawley, M. Lowe, B. Pavlakovic, The effect of bends on the propagation of guided waves in pipes, *J. Pressure Vessel Technol.* 127 (3) (2005) 328–335, <http://dx.doi.org/10.1115/1.1990211>.
- [11] T. Hayashi, K. Kawashima, Z. Sun, J.L. Rose, Guided wave propagation mechanics across a pipe elbow, *J. Pressure Vessel Technol.* 127 (3) (2005) 322–327, <http://dx.doi.org/10.1115/1.1990210>.
- [12] W. Wu, J. Wang, Effect of pipe bends on the low-frequency torsional guided wave propagation, *Arch. Acoust.* 45 (3) (2020) 385, URL <https://acoustics.ippt.gov.pl/index.php/aa/article/view/2740>.
- [13] K.E. Rudd, K.R. Leonard, J.P. Bingham, M.K. Hinders, Simulation of guided waves in complex piping geometries using the elastodynamic finite integration technique, *J. Acoust. Soc. Am.* 121 (3) (2007) 1449–1458, <http://dx.doi.org/10.1121/1.2431335>.
- [14] R.M. Sanderson, D.A. Hutchins, D.R. Billson, P.J. Mudge, The investigation of guided wave propagation around a pipe bend using an analytical modeling approach, *J. Acoust. Soc. Am.* 133 (3) (2013) 1404–1414, <http://dx.doi.org/10.1121/1.4790349>.
- [15] W. Wu, H. Dong, S. Zhang, Scattering of guided waves propagating through pipe bends based on normal mode expansion, *Sci. Rep.* 12 (1) (2022) 12488, <http://dx.doi.org/10.1038/s41598-022-16708-z>, URL <https://www.nature.com/articles/s41598-022-16708-z>.
- [16] S. Heinlein, P. Cawley, T. Vogt, Reflection of torsional T(0,1) guided waves from defects in pipe bends, *NDT E Int.* 93 (2018) 57–63, <http://dx.doi.org/10.1016/j.ndteint.2017.09.007>.
- [17] Z.-D. Xu, C. Zhu, L.-W. Shao, Damage identification of pipeline based on ultrasonic guided wave and wavelet denoising, *J. Pipeline Syst. Eng. Pract.* 12 (4) (2021) 04021051, [http://dx.doi.org/10.1061/\(ASCE\)JPS.1949-1204.0000600](http://dx.doi.org/10.1061/(ASCE)JPS.1949-1204.0000600), URL <https://ascilibrary.org/doi/abs/10.1061/%28ASCE%29PS.1949-1204.0000600>.
- [18] P. Huthwaite, Evaluation of inversion approaches for guided wave thickness mapping, *Proc. R. Soc. A* 470 (2166) (2014) 20140063, <http://dx.doi.org/10.1098/rspa.2014.0063>, URL <https://royalsocietypublishing.org/doi/10.1098/rspa.2014.0063>.
- [19] C.L. Willey, F. Simonetti, P.B. Nagy, G. Instones, Guided wave tomography of pipes with high-order helical modes, *NDT E Int.* 65 (2014) 8–21, <http://dx.doi.org/10.1016/j.ndteint.2014.03.010>, URL <http://www.sciencedirect.com/science/article/pii/S0963869514000449>.
- [20] A. Golato, F. Ahmad, S. Santhanam, M.G. Amin, Multi-helical path exploitation in sparsity-based guided-wave imaging of defects in pipes, *J. Nondestruct. Eval.* 37 (2) (2018) 27, <http://dx.doi.org/10.1007/s10921-018-0481-5>.

- [21] Y. Da, G. Dong, Y. Shang, B. Wang, D. Liu, Z. Qian, Circumferential defect detection using ultrasonic guided waves: An efficient quantitative technique for pipeline inspection, *Eng. Comput.* 37 (6) (2020) 1923–1943, <http://dx.doi.org/10.1108/EC-06-2019-0260>.
- [22] Y. Da, B. Wang, D. Liu, Z. Qian, A rapid and accurate technique with updating strategy for surface defect inspection of pipelines, *IEEE Access* 9 (2021) 16041–16052, <http://dx.doi.org/10.1109/access.2021.3051198>.
- [23] S. Livadiotis, A. Ebrahimkhanlou, S. Salamone, Monitoring internal corrosion in steel pipelines: A two-step helical guided wave approach for localization and quantification, *Struct. Health Monit.* 20 (5) (2020) 2694–2707, <http://dx.doi.org/10.1177/1475921720970139>.
- [24] Z. Wang, S. Huang, G. Shen, S. Wang, W. Zhao, High resolution tomography of pipeline using multi-helical lamb wave based on compressed sensing, *Constr. Build. Mater.* 317 (2022) 125628, <http://dx.doi.org/10.1016/j.conbuildmat.2021.125628>.
- [25] Y. Zhu, Y. Hu, F. Li, S. Abbas, W. Bao, W. Su, Internal damage localization for large-scale hollow cylinders based on helical sensor network, *Struct. Health Monit.* (2022) 1475921722112454, <http://dx.doi.org/10.1177/14759217221124503>.
- [26] D. Jansen, D. Hutchins, Lamb wave tomography, in: *IEEE Symposium on Ultrasonics*, Vol. 2, 1990, pp. 1017–1020, <http://dx.doi.org/10.1109/ULTSYM.1990.171515>.
- [27] J. Li, J.L. Rose, Natural beam focusing of non-axisymmetric guided waves in large-diameter pipes, *Ultrasonics* 44 (1) (2006) 35–45, <http://dx.doi.org/10.1016/j.ultras.2005.07.002>.
- [28] P. Huthwaite, F. Simonetti, High-resolution guided wave tomography, *Wave Motion* 50 (5) (2013) 979–993, <http://dx.doi.org/10.1016/j.wavemoti.2013.04.004>, URL <https://www.sciencedirect.com/science/article/pii/S0165212513000759>.
- [29] J. Rao, M. Ratassepp, Z. Fan, Guided wave tomography based on full waveform inversion, *IEEE Trans. Ultrasonics Ferroelectrics Frequency Control* 63 (5) (2016) 737–745, <http://dx.doi.org/10.1109/tuffc.2016.2536144>.
- [30] P. Huthwaite, M. Seher, Robust helical path separation for thickness mapping of pipes by guided wave tomography, *IEEE Trans. Ultrasonics Ferroelectrics Frequency Control* 62 (5) (2015) 927–938, <http://dx.doi.org/10.1109/tuffc.2014.006884>.
- [31] Z. Qian, C. Zhang, P. Li, B. Wang, Z. Qian, I. Kuznetsova, X. Li, A dictionary-reconstruction approach for separating helical-guided waves in cylindrical pipes, *J. Phys. D: Appl. Phys.* 56 (30) (2023) 305301, <http://dx.doi.org/10.1088/1361-6463/accaf2>.
- [32] M. Fink, Time reversal of ultrasonic fields. I. Basic principles, *IEEE Trans. Ultrason. Ferroelectr. Freq. Control* 39 (5) (1992) 555–566, <http://dx.doi.org/10.1109/58.156174>.
- [33] R. Lucena, J.D. Santos, Structural health monitoring using time reversal and cracked rod spectral element, *Mech. Syst. Signal Process.* 79 (2016) 86–98, <http://dx.doi.org/10.1016/j.ymsp.2016.02.044>.
- [34] R. Watkins, R. Jha, A modified time reversal method for Lamb wave based diagnostics of composite structures, *Mech. Syst. Signal Process.* 31 (2012) 345–354, <http://dx.doi.org/10.1016/j.ymsp.2012.03.007>.
- [35] A. Volker, T. van Zon, Guided Wave Travel Time Tomography for Bends, *AIP*, 2013, <http://dx.doi.org/10.1063/1.4789119>.
- [36] A.J. Brath, F. Simonetti, P.B. Nagy, G. Instanes, Acoustic formulation of elastic guided wave propagation and scattering in curved tubular structures, *IEEE Trans. Ultrason. Ferroelectr. Freq. Control* 61 (5) (2014) 815–829, <http://dx.doi.org/10.1109/TUFFC.2014.2973>.
- [37] A.J. Brath, F. Simonetti, P.B. Nagy, G. Instanes, Guided wave tomography of pipe bends, *IEEE Trans. Ultrasonics Ferroelectrics Frequency Control* 64 (5) (2017) 847–858, <http://dx.doi.org/10.1109/tuffc.2017.2683259>.
- [38] Y. Wang, X. Li, Elbow damage identification technique based on sparse inversion image reconstruction, *Materials* 13 (7) (2020) <http://dx.doi.org/10.3390/ma13071786>, URL <https://www.mdpi.com/1996-1944/13/7/1786>.
- [39] C.-O. Rasgado-Moreno, M. Rist, R. Land, M. Ratassepp, Acoustic forward model for guided wave propagation and scattering in a pipe bend, *Sensors* 22 (2) (2022) 486, <http://dx.doi.org/10.3390/s22020486>, URL <https://www.mdpi.com/1424-8220/22/2/486>.
- [40] N. Rawlinson, J. Hauser, M. Sambridge, in: R. Dmowska (Ed.), *Seismic Ray Tracing and Wavefront Tracking in Laterally Heterogeneous Media*, Vol. 49, Elsevier, 2008, pp. 203–273, [http://dx.doi.org/10.1016/S0065-2687\(07\)49003-3](http://dx.doi.org/10.1016/S0065-2687(07)49003-3), URL <https://www.sciencedirect.com/science/article/pii/S0065268707490033>.
- [41] N. Rawlinson, M. Sambridge, The fast marching method: An effective tool for tomographic imaging and tracking multiple phases in complex layered media, *Explor. Geophys.* 36 (4) (2005) 341–350, <http://dx.doi.org/10.1071/EG05341>.
- [42] B. O'Neill, *Elementary Differential Geometry*, second ed., Elsevier Science Publishing Co Inc, 2006, URL https://www.ebook.de/de/product/5124407/barrett_university_of_california_los_angeles_california_u_s_a_o_neill_elementary_differential_geometry_revised_2nd_edition.html.
- [43] A.N. Pressley, *Elementary Differential Geometry*, Springer, London, 2010, URL https://www.ebook.de/de/product/8787121/a_n_pressley_elementary_differential_geometry.html.
- [44] V. Rovenski, *Modeling of Curves and Surfaces with MATLAB®*, Springer, New York, 2010, <http://dx.doi.org/10.1007/978-0-387-71278-9>, URL https://www.ebook.de/de/product/8854935/vladimir_rovenski_modeling_of_curves_and_surfaces_with_matlab.html.
- [45] *MATLAB, Version 9.10.0.1739362 (R2021a)*, The MathWorks Inc., Natick, Massachusetts, 2021.
- [46] *ABAQUS/Standard User's Manual, Version 6.14*, Dassault Systèmes Simulia Corp, United States.
- [47] M. Drozd, L. Moreau, M. Castaigns, M.J.S. Lowe, P. Cawley, Efficient numerical modelling of absorbing regions for boundaries of guided waves problems, *AIP Conf. Proc.* 820 (1) (2006) 126–133, <http://dx.doi.org/10.1063/1.2184520>, URL <https://aip.scitation.org/doi/abs/10.1063/1.2184520>.
- [48] P. Huthwaite, R. Ribichini, P. Cawley, M.J. Lowe, Mode selection for corrosion detection in pipes and vessels via guided wave tomography, *IEEE Trans. Ultrason. Ferroelectr. Freq. Control* 60 (6) (2013) 1165–1177, <http://dx.doi.org/10.1109/TUFFC.2013.2679>.

Appendix 3

III.

Carlos-Omar Rasgado-Moreno, Marek Rist, Raul Land, and Madis Ratassepp.
Guided wave tomography of pipe bends based on full waveform inversion.
Ultrasonics, 148:107560, April 2025



Guided wave tomography of pipe bends based on full waveform inversion[☆]

Carlos-Omar Rasgado-Moreno^{a,*}, Marek Rist^b, Raul Land^b, Madis Ratassep^a

^a Department of Civil Engineering and Architecture, Tallinn University of Technology, Ehitajate tee 5, 19086, Tallinn, Estonia

^b Thomas Johann Seebeck Department of Electronics, Tallinn University of Technology, Ehitajate tee 5, 19086, Tallinn, Estonia

ARTICLE INFO

Keywords:

Full waveform inversion (FWI)
Guided wave tomography
Pipe bend
Hann-shaped defect
Autocalibration

ABSTRACT

Pipe bends are recognized as critical areas susceptible to wall thinning, a phenomenon instigated by abrupt changes in the fluid flow direction and velocity. Conventional monitoring techniques for bends typically depend on localized ultrasonic measurements of thickness. While these methods are effective, they can be time-consuming compared to the use of permanently installed transducers, a strategy employed in guided wave tomography (GWT). GWT provides the advantage of identifying and quantifying damage within a specified area by processing waves that are both generated and received by a set of transducers. In this study, we implement a GWT method based on full waveform inversion (FWI) for a high-resolution thickness reconstruction of a steel pipe bend. The wavefield in the bend section, made artificially anisotropic, is modeled using Thomsen parameters in the two-dimensional domain. This enhances its integration with the FWI algorithm. A numerical investigation was conducted to evaluate the efficacy of FWI in the presence of a defect as a function of its circumferential position. Additionally, an experimental evaluation was performed to reconstruct a defect artificially created on a pipe bend with a diameter (d) of 220 mm and a bend radius of $1.5d$, and a defect with a diameter of 100 mm and a depth of 47%. The results indicate that the FWI method can effectively reconstruct the thickness map of smooth defects, regardless of their location, and it is particularly effective for defects situated closer to the extrados position.

1. Introduction

Pipe bends, among other components in pipeline systems, face unique challenges due to stress from fluid direction changes, making them vulnerable to fatigue, corrosion, and cracking [1]. Fatigue results from repeated stress cycles, leading to microscopic cracks that can grow over time, potentially causing pipe failure [2]. Corrosion, the natural deterioration of the pipe material due to chemical reactions with the environment, can thin the pipe walls, reducing their pressure-withstanding capacity [3]. Cracking can occur due to both fatigue and corrosion [4], especially at high-stress areas like pipe bends. These cracks can propagate, significantly reducing the pipe's structural integrity and potentially leading to failures if they are not detected and remedied in time. Therefore, identifying and monitoring damages in pipeline features, such as bends, is key to maintaining pipeline efficiency, reducing maintenance expenses, prolonging the operational lifespan, and preventing disastrous failures [5].

Traditional non-destructive testing (NDT) methods used for pipeline inspection often face challenges due to their inherent limitations. For instance, X-rays, while their image reconstruction is quite sensitive,

can be cumbersome to implement [6]. Local thickness gauges, on the other hand, are slow when they are used to inspect large areas [7]. In-pipe robots provide detailed inspections but require the halting of plant operations [8], which can lead to significant downtime and potential economic losses.

Alternatively, ultrasonic guided wave tomography (GWT) has emerged as a powerful tool to locate and quantify damage [9,10]. In a traditional pitch-catch setup, GWT is performed by a pair of transducer arrays in direct contact with the pipe surface, as illustrated in Fig. 1(a). In Fig. 1(a), two rings of transducers are attached to the pipe surface. Each ring consists of an equal number of transducers, where one ring can emit the guided wave, while the other ring receives the transmitted signals coming from different angles.

Guided wave tomography (GWT) leverages the dispersion characteristics of wave guides, which are dependent on the product of frequency and thickness [11]. Fig. 1(b) illustrates the dispersion curves of the fundamental Lamb wave modes for an 8-mm-thick steel plate. Compared to the S_0 mode, the A_0 mode exhibits greater dispersion at lower frequencies, as highlighted by the dashed lines in Fig. 1(b). GWT

[☆] This document represents the results of the research project funded by the European Union's Horizon 2020 Research and Innovation Programme under grant agreement no. 860104, project GW4SHM (Guided Waves for Structural Health Monitoring), and the Estonian Research Council, Estonia, grant PRG737.

* Corresponding author.

E-mail addresses: carlos.rasgado@taltech.ee (C.-O. Rasgado-Moreno), madis.ratassep@taltech.ee (M. Ratassep).

<https://doi.org/10.1016/j.ultras.2024.107560>

Received 15 May 2024; Received in revised form 23 October 2024; Accepted 18 December 2024

Available online 1 January 2025

0041-624X/© 2025 Elsevier B.V. All rights are reserved, including those for text and data mining, AI training, and similar technologies.

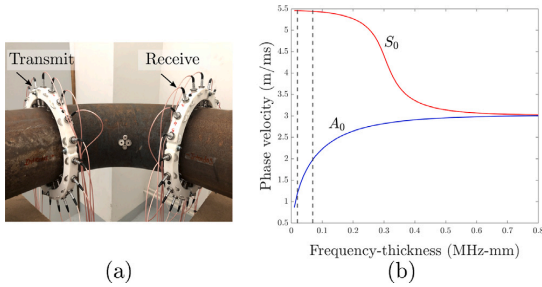


Fig. 1. A guided wave tomography setup (a), integrated by two rings of transducers, and the dispersion curves of fundamental Lamb wave modes for an 8-mm-steel plate (b). In this study we used the information of the A_0 mode contained in the dashed lines.

primarily relies on analyzing waveforms to create a thickness map for a specific section, defined by the transducer rings. As both phase and group velocities are influenced by the frequency-thickness product, any change in the wall thickness, assuming a constant frequency, will result in a variation in the phase velocity of the wavefield. Consequently, if a velocity reconstruction is generated, it can be interpolated back to thickness [12].

Hence, any thickness loss within the delimited area is iteratively reconstructed by minimizing the difference between the observed and synthetic data, making GWT suitable for structural health monitoring applications [13–15].

GWT has been applied extensively for damage characterization in both isotropic and anisotropic materials, particularly in simple structures such as plates [16,17] and straight pipes [18,19]. The preference for two-dimensional (2-D) acoustic models over their three-dimensional (3-D) counterparts in GWT is primarily due to their simplicity, lower computational demands, and compatibility with tomographic algorithms.

The process of the 2-D modeling of guided wave propagation in straight pipes involves unwrapping the pipe axially, which results in an approximation similar to guided wave propagation in plates [20]. This allows the same acoustic wave equation used for plates to be applied to model guided waves and their interaction with defects, by integrating the cyclic nature of the pipe into the model [18]. However, the propagation of guided waves in a bend section poses additional challenges compared to a straight pipe, primarily due to the anisotropy of the wavefield induced by the bend radius.

The application of GWT to pipe bends has been primarily constrained to the orthogonal parametrization of the pipe bend into a 2-D domain, coupled with travel-time-tomography-based methodologies [21–23]. For instance, Volker and van Zon [21] proposed a 2-D deformed grid representation of a pipe bend and successfully reconstructed a smooth defect numerically. Conversely, Brath et al. [24] presented an orthogonal representation of a pipe bend using a 2-D rectangular domain. In this model, the acoustic wavefield is rendered artificially inhomogeneous and elliptically anisotropic. This parametrization was subsequently implemented in [22,23] to reconstruct the maps of the remaining thickness in pipe bends affected by corrosion.

Travel-time tomography, while effective, has its limitations. It depends on the time-of-flight (TOF) measurements to build a representation of the distribution of the wave propagation speed, using a ray model as a basis. This approach tends to overlook diffraction and is limited to reconstructing defects larger than the wavelength of the guided wave. In the context of a pipe bend, the rays often bypass the bend elbow due to the focusing effect [24,25]. As a result, the accuracy of travel-time tomography in pipe bends is influenced by the circumferential position of the defect [26]. To reduce this constraint, Brath

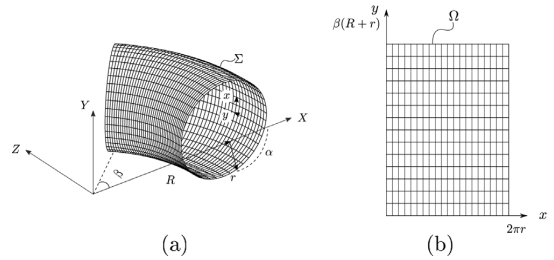


Fig. 2. A pipe bend section can be represented as a torus section (a). Then, the 3-D space domain Σ can be translated into the 2-D space domain Ω (b).

et al. [22] suggested the addition of an extra set of transducers along the bend's elbow. This enhancement increases the view angles, thereby reducing the dependency on the defect's circumferential position, at the cost of additional transducers.

To overcome the limitations of travel-time tomography, in this study we introduce a full waveform inversion (FWI) tomography method based on guided waves for corrosion mapping in pipe bends, by introducing a new acoustic forward model for a pipe bend. FWI utilizes all of the waveform information, not just specific features such as the TOF, allowing more accurate results [27–29]. We discretize the 2-D acoustic model using the finite difference (FD) method [30]. Then, the anisotropy wavefield, which is determined by the curvature of the bend, is shaped using Thomsen parameters [31]. Furthermore, we examine the impact of the circumferential position of the defect on the thickness mapping and conduct an experimental validation of the method.

This paper is organized as follows: the methods for acoustic modeling and full waveform inversion for a pipe bend are detailed in Sections 2 and 3, respectively. Section 4 introduces the numerical methods employed in this study. The proposed approach is then validated both numerically and experimentally, with the results being presented in Section 5. Finally, Section 6 draws conclusions from the study and discusses potential future work.

2. 2-D acoustic forward model of a pipe bend

2.1. Orthogonal parametrization

The implementation of GWT based on full waveform inversion requires a 2-D representation of the acoustic wavefield for a pipe bend. In this context, we can conceptualize the pipe bend section as a function of revolution or a torus section, as illustrated in Fig. 2(a). The torus section is defined within the 3-D domain Σ by the minor radius r , major radius R , azimuth longitude β , and latitude α . Subsequently, we introduce a parametrization of the torus in the 2-D space domain Ω , as proposed by [24], that is represented by the following set of equations:

$$\begin{aligned} X &= \left(R + r \cos \frac{x}{r} \right) \cos \frac{y}{R+r}, \\ Y &= r \sin \frac{x}{r}, \\ Z &= \left(R + r \cos \frac{x}{r} \right) \sin \frac{y}{R+r}. \end{aligned} \quad (1)$$

Consequently, the 2-D domain Ω can be defined as $\Omega = [0, 2\pi r] \times [0, \beta(R+r)]$, with the longest azimuth length located in the middle of the ω plane, at $(\pi r, y)$, and the shortest at the edges $(0, y)$ and $(2\pi r, y)$, respectively.

2.2. Wave equation

Given the orthogonal parametrization of the pipe bend in Eq. (1), the guided wave propagation into the 2-D domain can be modeled as

an elliptically anisotropic wavefield [24]. Consequently, the acoustic wavefield of a torus section can be represented as a vertical transversely isotropic (VTI) medium. The acoustic wavefield of a VTI medium can be described by a system of second-order partial differential equations [32]:

$$\begin{cases} \frac{1}{v^2} \frac{\partial^2 p}{\partial t^2} - (1 + 2\delta)H p - H_0 p = (1 + 2\delta)H q, \\ \frac{1}{v^2} \frac{\partial^2 q}{\partial t^2} - 2(\epsilon - \delta)H q = 2(\epsilon - \delta)H p, \end{cases} \quad (2)$$

where the differential operators H and H_0 are defined as

$$\begin{cases} H = \cos^2 \theta \frac{\partial^2}{\partial x^2} + \sin^2 \theta \frac{\partial^2}{\partial y^2} - \sin 2\theta \frac{\partial^2}{\partial x^2 \partial y^2}, \\ H_0 = \sin^2 \theta \frac{\partial^2}{\partial x^2} + \cos^2 \theta \frac{\partial^2}{\partial y^2} - \sin 2\theta \frac{\partial^2}{\partial x^2 \partial y^2}. \end{cases} \quad (3)$$

In Eq. (2), p represents the pressure field of the propagating wave, q denotes an auxiliary wave field, v is the pressure phase velocity, and ϵ and δ stand for anisotropic parameters, as defined by Thomsen [33].

To describe the elliptical anisotropy wavefield for a torus section as a VTI medium, consider the relationship between the phase velocity and the velocity along the symmetry x -axis, denoted as v_v [32]:

$$\frac{\cos^2 \bar{\theta}}{v_v^2} = \frac{1}{v^2} - (1 + 2\delta) \frac{\frac{\sin^2 \bar{\theta}}{v_v^2} \frac{1}{v^2}}{\frac{1}{v^2} - 2(\epsilon - \delta) \frac{\sin^2 \bar{\theta}}{v^2}}, \quad (4)$$

where $\bar{\theta}$ is the angle with respect to the symmetry axis. Notably, for a VTI medium, $\bar{\theta} = \pi/2$, and given the elliptical anisotropy condition, $\epsilon = \delta$ [34]. In addition, following the orthogonal representation of the bend from Eq. (1), the velocity along the symmetry x -axis v_v is determined by $v_v = \frac{1}{\rho}$, with $\rho = \frac{R+r \cos(\theta)}{(R+r)}$ [24]. Hence, Eq. (4) yields

$$\epsilon = \delta = \frac{1}{2} \left(\frac{1}{\rho^2} - 1 \right). \quad (5)$$

3. Full waveform inversion

The forward problem described in Section 2 enables the prediction of the wavefield data $\mathbf{u}(\mathbf{m}(\omega))$, as a function of the angular frequency ω , for a given emission-transmission configuration and a particular group of wavefield parameters \mathbf{m} , defined at each point (x, y) on the 2-D grid shown in Fig. 2(b). In GWT we aim to compute the parameters \mathbf{m} that allow the calculation of synthetic wavefields \mathbf{u} that closely match the experimental measurements \mathbf{d} . The residual error can be calculated as

$$\Delta \mathbf{d} = \mathbf{u}(\mathbf{m}) - \mathbf{d}(\mathbf{m}_{obs}) \quad (6)$$

(with an implicit dependency on ω), where $\mathbf{u}(\mathbf{m})$ is the wavefield calculated by Eq. (2), and $\mathbf{d}(\mathbf{m}_{obs})$ is the observed wavefield. Naturally, we aim to find \mathbf{m} such that $\Delta \mathbf{d}$ is minimized. Thus, the inverse problem is formulated to minimize the sum of squared residuals:

$$\min_{\mathbf{m}} f(\mathbf{m}) = \frac{1}{2} \Delta \mathbf{d}^T \Delta \mathbf{d}, \quad (7)$$

where $\min_{\mathbf{m}} f(\mathbf{m})$ represents the l_2 norm misfit function, and $\Delta \mathbf{d}^T$ denotes the conjugate transpose of the residual error.

In this study, the non-linear waveform inversion problem is computed with the SEISCOPE optimization toolbox [35]. SEISCOPE solves the inversion problem using the gradient method: it starts with a given initial model, and a forward-modeling step is performed to compute the residuals in Eq. (6). The parameter set \mathbf{m} is updated iteratively to derive a new set of parameters, defined as follows:

$$\mathbf{m}_{k+1} = \mathbf{m}_k - a_k \Delta m_k, \quad (8)$$

where k is the iteration step, and a is the scalar step length; it is computed through a line-search process [35]. Δm_k is the gradient

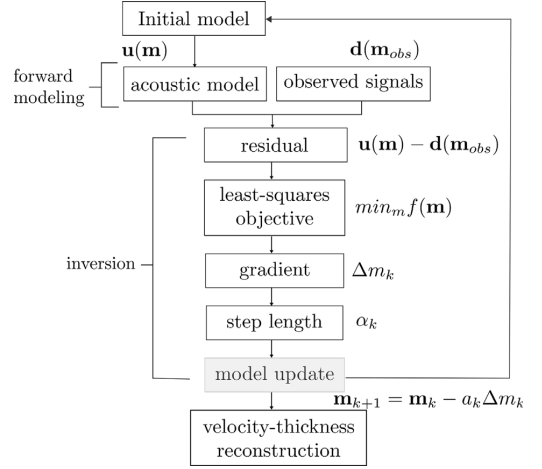


Fig. 3. Flow diagram of the full waveform inversion algorithm. The inverse problem is formulated to iteratively minimize the sum of squared residuals.

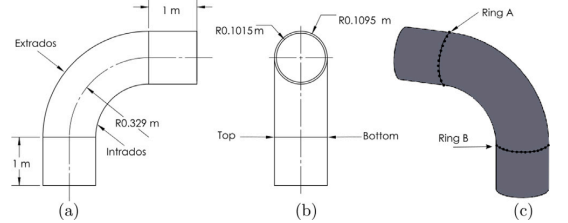


Fig. 4. Steel pipe bend geometry used in simulation and experimental validation: top view (a), front view (b), and isometric view (c).

Table 1
Mechanical properties of the steel pipe specimen.

Density ρ (kg/m ³)	Young's modulus E (GPa)	Poisson's ratio ν
7932	216.9	0.2865

of the misfit function with respect to the model parameters. Among the optimization routines that can be used to compute the gradient inside the SEISCOPE optimization toolbox, we selected the Nonlinear Conjugate Gradient algorithm [36] to solve the inversion problem due to its low computational demand [35].

The model perturbations are iteratively updated by multiplying the gradient of the objective function by the step length a , which is computed through a line-search process and simultaneously recalculated at each iteration. To illustrate the algorithm, a flow diagram is shown in Fig. 3.

4. Numerical modeling

4.1. Configuration of the problem

In this work, we considered the steel pipe bend geometry described in Fig. 4. The geometry consists of an inner radius $r_{in} = 0.1015$ m, an outer radius $r_{out} = 0.1095$ m, an azimuth longitude $\beta = \pi/2$ with a major radius $R = 0.329$ m, and two straight pipe sections at the beginning and at the end of the bend that are each 1 m long. The straight sections were only included in the elastic modeling and experimental measurements

to avoid reflections due to the edges. Likewise, the mechanical material properties are listed in Table 1.

Twenty transducers were equally distributed among each transducer ring (A-B) and located at both ends of the bend, as shown in Fig. 4(c). Further details on the bend geometry, experimental setup, and guided wave propagation in this configuration are described in [31].

4.2. Elastic modeling

3-D elastic models are often considered to provide a more accurate representation of guided wave propagation compared to 2-D models. This is because 3-D models can capture the full complexity of wave propagation in all directions [37]. Therefore, in this study we computed 3-D guided wave propagation simulations in order to compare them with experimental data. We performed simulations using the ABAQUS Explicit software [38]. The finite element model of the pipe geometry, described in Fig. 4, was built with 560 elements around its circumference, 6 elements across its thickness, and 550 elements spanning the 90-degree axial rotation, and the C3D8R eight-node brick element type was used. To avoid boundary reflections, we designated absorbing regions beyond the edges of the bend (in the straight pipe sections) [39].

We excited the A_0 mode by applying an out-of-plane force in the radial direction. The A_0 mode is considered to have a higher sensitivity to thickness variations than the S_0 mode [40]. After this, we recorded the radial displacement components on the bend's opposite side, resulting in 400 transmitted signals for each ring of transducers. The dispersion curves for an 8-mm-thick steel plate are shown in Fig. 1(b), which illustrates the phase velocity as a function of frequency. As can be seen from Fig. 1(b), the A_0 mode shows substantial dispersion at lower frequencies. Consequently, we excited a five-cycle tone burst with a central frequency of 50 kHz, modulated by a Hanning window.

4.3. Acoustic modeling

The image reconstructions for numerical and experimental analysis, later described in Section 5, are computed by considering all wave packets that have completed up to three full revolutions around the circumference. As a result, the 2-D domain consists of three identical replicas, as illustrated in Fig. 5. Each replica is discretized using $4.143 \times 4.143 \text{ mm}^2$ square elements, leading to 481×166 nodes (circumferential-azimuthal). Naturally, the emissions were located in the central replica, while the transmissions were also located in the additional replicas; this was done to include the higher-order helical wave paths in the simulation [24].

Fig. 5(a) and (b) show the distribution of Thomsen parameters along the bend and the phase velocity distribution or background velocity, respectively. The phase velocity remains constant due to the isotropic nature of the steel. However, the wavefield is artificially made anisotropic by the Thomsen parameters. The anisotropy extends from the center of the replica towards the edges, as shown in Fig. 5(a).

It should be noted that the 2-D FD model is a simplified representation of the more complex 3-D wave propagation model. This approximation can impose certain limitations on the inversion process, particularly if the data used for modeling diverge significantly from one another [41].

We followed the FD method using the mixed-grid approach for the simulations in the acoustic domain [30]. We carried out calculations using the 2-D frequency-domain engine TOY2DAC [35]. TOY2DAC uses the optimization routines from the SEISCOPE toolbox to address the minimization problem defined by Eq. (7) in the frequency domain for a given frequency. The fast Fourier transform was used to convert the results from the time domain to the frequency domain. The phase velocity was the inverted parameters at a specific frequency, and we derived the remaining thickness maps by interpolating the reconstructed velocity as a function of the frequency-thickness product using the dispersion

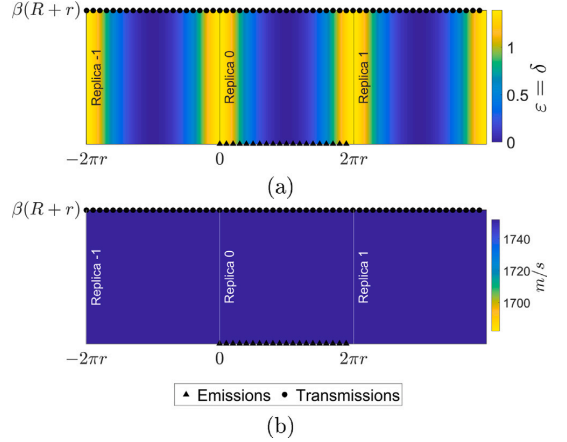


Fig. 5. Input parameters for the acoustic modeling. Thomsen parameters ϵ and δ (a) make the wavefield artificially anisotropic given the phase velocity (b) along the bend.

curve of the A_0 mode. The computations were performed on a cluster with two Intel Xeon E5-2660v2 processors and 64 GB RAM, and the calculation time for a single frequency was 5 min. Further details on the 2-D acoustic forward model that uses Thomsen parameters to map the elliptical anisotropy of the bend area, as well as its resemblance to its 3-D elastic modeling counterpart and scattering, can be found in [31].

4.4. Helical path separation

The 2-D acoustic model, as outlined in Section 2, mirrors the GW propagation of a plate. However, it does not account for the cyclic characteristic of the pipe within a specific inspection area, defined by a pair of transducer rings. To isolate the first wave packet that reaches the receivers from the elastic modeling and experimental measurements, we used the robust helical path separation algorithm, as developed in [42].

In the helical path separation algorithm, the time traces $u_{r,s}(t)$, which originate from emission s and arrive at transmission r , are duplicated m times to create $u_{r+Nm,s}(t)$. Here, N denotes the total number of sources, m the number of replicas, and Nm the increment in each receiver transducer number. Next, the replicated time traces $u_{r,s}(t)$ are time-reversed by

$$\bar{U}_{\bar{r},s}(\omega) = \text{FFT}(u_{r,s}(t)) \exp[-ik(\omega)x_{\bar{r},s}], \quad (9)$$

where $\bar{U}_{\bar{r},s}(\omega)$ is the time-reversed signal in the frequency domain, $k(\omega)$ is the wave number for each frequency ω , and $x_{\bar{r},s}$ is the traveled distance from the transmission to the emission.

Moreover, a series of band-pass filters and windows are applied to extract the first-arriving wave packet $\bar{\phi}_{\bar{r},s}(\omega)$. Then, $\bar{\phi}_{\bar{r},s}(\omega)$ is forward-propagated:

$$\bar{\phi}_{\bar{r},s}^{\text{hp}}(\omega) = \bar{\phi}_{\bar{r},s}(\omega) \exp[ik(\omega)x_{\bar{r},s}]. \quad (10)$$

Finally, the original replicated time traces $u_{r,s}(t)$ are cleaned up by minimizing the waveforms belonging to other replicas. Mathematically, this is represented as

$$u_{r,s}^{\text{hp}}(t) = u_{r,s}(t) - \bar{\phi}_{\bar{r},s}^{\text{hp}}(t), \quad (11)$$

with $u_{r,s}^{\text{hp}}(t)$ being the helical-path-separated time traces. Note that the accuracy of Eqs. (9) and (10) is dependent on the ray's traveled distance $x_{\bar{r},s}$. Hence, computing the shortest path $x_{\bar{r},s}$ is crucial for a successful implementation. Further details and this method's application to pipe bends can be found in [43].

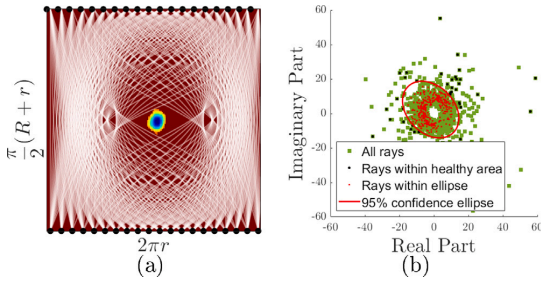


Fig. 6. All the rays used to calibrate $D_{r,s}$ (a), and calibration factors $Q_{r,s}$ plotted in the complex plane (b).

4.5. Data calibration

Given that the inversion algorithm relies on FD acoustic modeling, it is recommended to adjust the data in relation to the acoustic model, whether they are simulation data or experimental data [16]. The re-scaling is crucial to compensate for any potential discrepancies in phase and amplitude between the two models, thereby reducing the number of artifacts.

Conventionally, the calibration factor Q is computed as

$$Q_{r,s} = \frac{U_{r,s}(\omega)}{D_{r,s}(\omega)}, \quad (12)$$

where $U_{r,s}$ and $D_{r,s}$ are the data transmitted from r to s by FD modeling and the observed data in the frequency domain, respectively. In the literature, $Q_{r,s}$ is often computed with a baseline data set, with $D_{r,s}$ being the transmitted data without any flaw, or by manually selecting a ray that propagates through a domain free from any defects [17,26,41,44]. However, for practical applications, a baseline data set might not be available, or it might lead to false alarms [45].

In this work, we followed the autocalibration method for the re-scaling step [46]. Overall, the autocalibration method consists of locating the defect and using the *healthy* rays to compute the mean \bar{Q} for those rays that are in close proximity to the flaw. Briefly, $Q_{r,s}$ is constructed in three steps:

- Locating the defect.** A background velocity model should be obtained, so that we can estimate the position of the defect. This can be achieved by ray-tomography-based algorithms [46].
- Selecting healthy rays.** Then, all the ray paths $D_{r,s}^d$ in close proximity to the flaw are removed, with a distance defect-ray threshold of 1%, keeping only the healthy rays $D_{r,s}^h$ for the next step.
- Computing the confidence ellipse.** Next, a 95% confidence ellipse of the calibration factors $Q_{r,s}^h$ of the remaining ray paths $D_{r,s}^h$ is computed. Finally, the calibration factors for all the ray paths outside of the confidence ellipse are set to the mean of the rays contained in the ellipse.

Fig. 6(a) shows the velocity field of a pipe bend with an arbitrary defect located at the extrados. The ray paths are bent due to the elliptical anisotropy. In Fig. 6(b), those rays in close proximity to the flaw have been excluded to compute the mean calibration factor \bar{Q} .

5. Results and discussion

5.1. Numerical study

We conducted a numerical investigation to evaluate the efficacy of FWI in reconstructing the thickness map of a pipe bend in the presence of Hann-shaped defects at different circumferential positions.

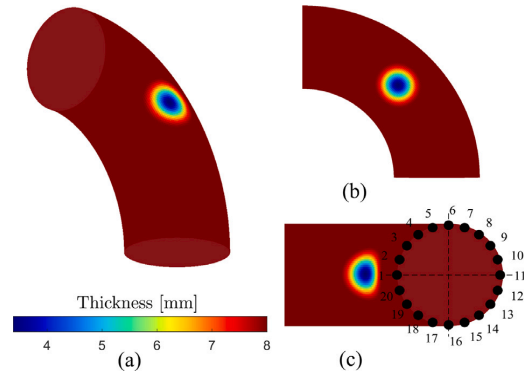


Fig. 7. Hann-shaped defect with 50% thickness reduction located at 0° (a), 90° (b), and 180° (c).

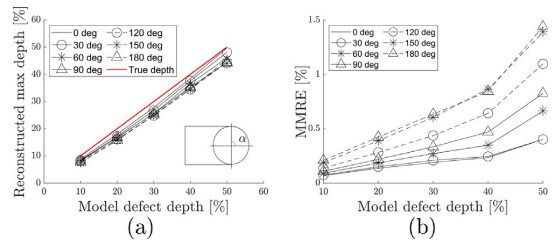


Fig. 8. Maximum thickness maps reconstructed as a function of defect depth and position around the pipe circumference (a) and relative mean error for each case (b).

The width of the defect was set to 120 mm for all the cases, while the depth of the defect was varied from 10% to 50%; it was placed at seven different circumferential positions α : 0°, 30°, 60°, 90°, 120°, 150°, and 180°, respectively. Fig. 7 shows three main locations of the defect's position: extrados (a), top (b), and intrados (c). The distribution of the transducers, for both numerical and experimental studies, is illustrated in Fig. 7(c). Further details about the Hann-shaped defect characterization are described in [31].

To quantitatively evaluate the wall-thickness loss map reconstruction, we used the *mean magnitude of relative error* (MMRE) of the residuals between the true defect T and the reconstructed Γ wall-thickness maps. The MMRE is the mean of the ratios of the absolute difference between two values to the magnitude of one of the values [47]. For a total of n ratios,

$$MMRE = \frac{1}{n} \sum_{i=1}^n \frac{|T_i - \Gamma_i|}{T_i}. \quad (13)$$

Fig. 8(a) illustrates the relationship between the reconstructed maximum depth and the nominal defect depth, varying with the defect's position around the pipe circumference. The depth is expressed as a percentage of the nominal wall thickness. Similarly, Fig. 8(b) shows how the MMRE varies with the defect's depth and position around the circumference.

Fig. 8(a) makes it clear that for each circumferential position, the maximum reconstruction depth accuracy has a linear trend. In addition, the MMRE from Fig. 8(b) shows a dependency on the circumferential position. The closer the defect is to the center of the 2-D domain, the more accurate the reconstruction. This trend is a consequence of the limited view angles [48].

Compared to GWT based on the TOF for a pipe bend [22,23], it is evident that FWI is capable of locating the defect regardless of its

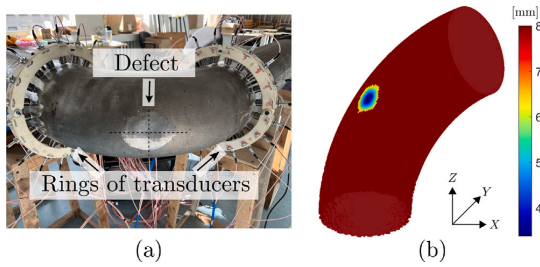


Fig. 9. Thickness reduction on a steel pipe bend (a) and its remaining thickness (b).

circumferential position. In TOF approaches, the ray paths in the bend avoid the extrados positions due to the focusing effect [25], limiting the coverage of the view angles. As a result, Brath et al. [26] proposed adding an additional array of transducers along the extrados position. In contrast, FWI takes advantage of the focusing effect, resulting in a more accurate reconstruction when the defect is located close to the extrados, as illustrated in Fig. 8(b).

In addition, since FWI does not rely on the wave paths for the inversion scheme, a conventional pair of transducers is sufficient for the monitoring process. Moreover, greater accuracy can be achieved by increasing the number of replicas or using adaptive threshold regularization [49] or Tikhonov regularization [50].

5.2. Experimental validation

We utilized an angle grinder to decrease the thickness of the pipe bend, and we aimed to create a smooth defect with a diameter of 100 mm and a thickness reduction of 47%, as shown in Fig. 9(a). The center of the defect is at $[0, \pi/2]$, which are the circumferential and azimuth coordinates, respectively. Subsequently, Creaform's ACADEMIA 50 scanner [51] was employed to measure the remaining surface of the pipe bend. The scanner uses structured white light technology, which involves projecting structured light onto an object and using cameras to capture the deformation of the light pattern. These data were then processed to generate a detailed 3-D model of the pipe bend. The remaining wall-thickness map was then interpolated to fit the elastic model of the pipe bend described in Section 4.2. The 3-D elastic model was used to generate a synthetic data set to assess the FWI reconstruction against the FWI from the experimental results. Fig. 9(b) displays the remaining thickness of the pipe bend.

For this study, we used the measurement setup shown in Fig. 9(a). The measurement setup includes two rings, each containing 20 piezoelectric transducers with a resonant frequency of 43 kHz. These transducers, produced by Doppler, Ltd., in Guangzhou, China, are placed at both ends of the bend. The setup is complemented by a multiplexer for signal excitation and a data acquisition box. The transducers, which are uniformly distributed around the circumference, are spring-loaded against the pipe to facilitate radial excitation. Further details about the instrumentation are given in [31].

We measured the transmission of A_0 from each transducer to the opposite ring, resulting in a total of 400 recorded signals per transducer ring. The excitation source, 2-D acoustic model, 3-D elastic model, and measurement response are shown in Fig. 10.

Fig. 10(a) illustrates the excited five-cycle tone burst with a central frequency of 50 kHz, along with the corresponding response from one transducer ring when it is excited at the extrados position. The 3-D elastic modeled and measured data are shown in Fig. 10(b) and (c), respectively. Both wavefields have been replicated three times in accordance with the helical path separation algorithm. For reference, the wavefield without any flaws, resulting from the 2-D acoustic forward model, is included in Fig. 10(d). This model naturally does not include

any helical paths due to the absorbing boundary conditions in the 2-D acoustic forward model [30].

In contrast, Fig. 10(e) and (f) display the extracted wavefield after computing the helical path separation for the elastic modeled and measured data, respectively. Fig. 10(e) shows minor artifacts along the extracted wavefield, which can be attributed to its interaction with the defect and the robustness of the helical path separation algorithm [42]. Further analysis of the acoustic forward model and the helical path separation for pipe bends is provided in [43].

The last row of Fig. 10 presents the frequency spectrum of the transmitted data at the extrados position ($\bar{r} = 31$) for the 2-D FD (g), 3-D elastic modeled (h), and experimental data (i). As expected, the central frequency of the 2-D transmitted data in Fig. 10(g) is 50 kHz, and the same is true for the 3-D elastic modeled data in Fig. 10(h). In contrast, the central frequency of the transmitted data in Fig. 10(i) is 45 kHz. This shift can be attributed to the transducer performance, which generates significant heat at resonance, leading to low efficiency [52]. Additionally, in Fig. 10(g)–(i), the pressure field of the initial acoustic model $U(m_0)$ and the frequency components used for the monochromatic reconstruction of the observed data $D_{r,s}(m_{obs})$ at 50 kHz or $D_{r,s}(\omega_{50})$, which are later used for the FWI algorithm to compute the misfit function, are highlighted with a triangle. Then, before performing the inversion, we re-scaled the 3-D elastic modeled and measured selected frequency components $D_{r,s}(\omega_{50})$, following the autocorrelation method described in Section 4.5. This resulted in a total of 2400 components, which include the view angles from the three replicas and the two arrays.

Fig. 11 illustrates the 2-D representation of the real thickness reduction measured with the Creaform scanner and its monochromatic reconstruction of the thickness at 50 kHz, obtained after 10, 20, and 40 iterations for the 3-D elastic modeled and measured data. In the case of the 3-D elastic modeled data, the solution exhibits a smooth evolution during the iteration process. It starts by over-sizing the defect in Fig. 11(b), getting closer to the real size in Fig. 11(c) and achieving a more detailed reconstruction of the depth towards the final iteration in Fig. 11(d).

In addition, Fig. 12 shows the norm of the gradient misfit function $\|\nabla f(m_k)\|$ [53] with respect to the model parameter m_k for the 3-D elastic modeled and measured data. The 3-D elastic modeled data initially exhibit a smaller gradient compared to the measured data. This discrepancy arises because the FE simulations represent an idealized case without experimental uncertainties. Moreover, the modeled data appear to converge after 30 iterations.

In contrast, the size of the defect appears to converge from iteration 10, as shown in Fig. 11(e), and later defines the depth towards the center of the defect in subsequent iterations. Additionally, compared to the 3-D elastic modeled data, the measured data exhibit a higher number of artifacts. These artifacts are more remarkable in the azimuthal direction, with a tilted and shallow ellipsoidal shape, showcasing a depth of up to 2 mm.

To further illustrate the construction of the thickness maps, Fig. 13 shows the axial profiles along the circumferential and azimuthal directions after 40 iterations, respectively. For simplicity, higher artifacts were removed.

For the 3-D elastic modeled data, a good agreement was observed between the size and location of the defect. Despite the presence of some artifacts, they do not degrade the quality of the interior of the defect area. The resulting MMRE was 0.4%, which was expected from the maximum thickness map study previously mentioned in Fig. 8(b).

On the other hand, the length of the defect is notably underestimated in the circumferential direction, as shown in Fig. 13(a). However, Fig. 13(b) shows a good agreement in the azimuthal direction, resulting in an MMRE of 0.7%.

The inaccuracy in the circumferential direction and strong artifacts in the azimuthal direction can be attributed to the normalization of the scattered signals using the mean of the non-scattered ones in the

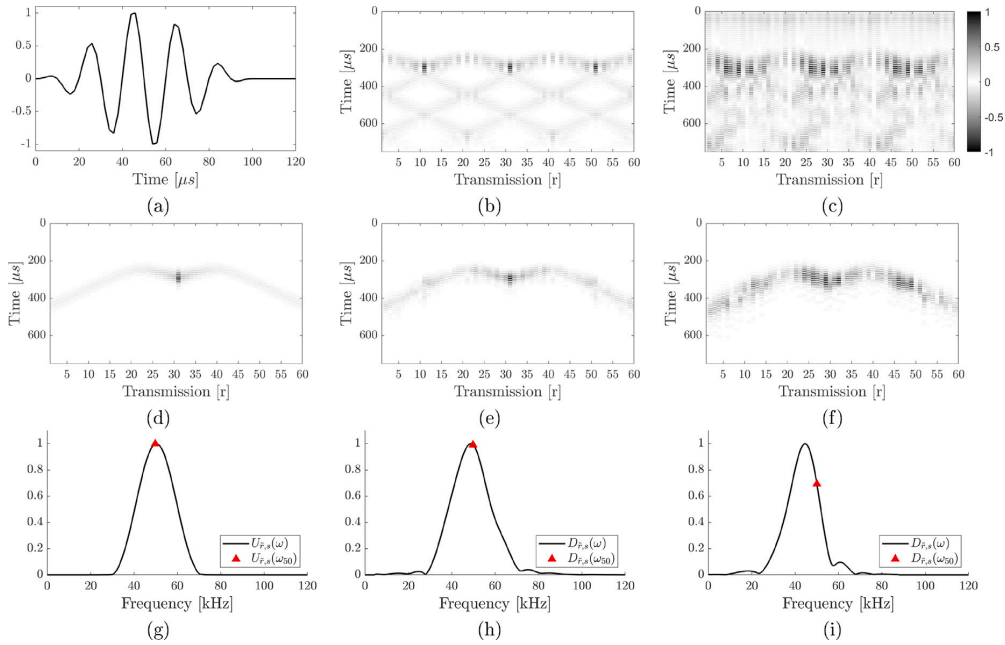


Fig. 10. Excitation source (a), the recorded wavefields when excited at position 11 for the 3-D elastic modeled data (b), and the measurements (c). 2-D acoustic wavefield without a flaw (d), the helical-path-separated wavefields for the 3-D elastic modeled data (e), and measurements (f). Frequency spectra from transmission 31 for the 2-D acoustic wavefield (g), 3-D elastic model (h), and measurements (i). The misfit function in the monochromatic FWI algorithm is computed between the highlighted triangles in (g)–(i). Amplitudes have been normalized.

autocalibration step. Note that the main goal of the re-scaling step is to address the intrinsic *non-uniqueness* of the acoustic full waveform inverse problem [54,55]. Hence, the higher the mismatch between the observed and synthesized signals, the more errors occur during the inversion [56].

Moreover, the experimental results can be affected by the manufacturing tolerances of the bend, noise, the positioning of the transducers, errors in the helical path algorithm, coupling, and the performance of the transducer.

As mentioned earlier, the spectrum of the measured data in Fig. 11(i) showed an unexpected transducer performance. To further investigate the level of experimental uncertainties in the measured data, we analyzed the TOF and amplitudes of the recorded wavefields. Fig. 14 illustrates the mismatch between the TOF and the amplitude of the synthetic data without defects and the measured signals for three emission positions: intrados (a)–(b), top (c)–(d), and extrados (e)–(f).

In Fig. 14(a), (c), and (e), we obtained the TOF by taking the difference between the peaks of the Hilbert envelope of the input and measured signal. In Fig. 14(b), (d), and (f), we computed the amplitude as the logarithm of the root mean square of each individual time trace, resulting in a smooth comparison of the amplitudes for each wavefield.

At a glance, the TOF curves of the measured data resemble the shape of the synthetic data, with a mean delay of 3 ms. The peaks of the TOF in the experimental data might be due to the positioning of the transducers and the scatter signals from the defect. In contrast, the amplitudes of the experimental wavefields are randomly distributed, and the focusing effect [20,25,31], apparent in the peaks of the amplitudes of the synthetic data, is not present in the measured data.

The random amplitude distribution could be attributed to the following:

- (a) The inhomogeneous coupling of the transducers, which are spring-loaded against the pipe, making it physically challenging to guarantee their homogeneous distribution;

- (b) The inhomogeneous transducer performance. If the transducer’s performance was homogeneous, in Fig. 14(d) and (f), we should see a boost in the amplitude of the experimental signal when it is excited in the top or extrados positions, as a consequence of the focusing effect.

In addition, it has been demonstrated that strong amplitude variations decrease the accuracy of FWI, even though the initial model is good enough to ensure that the inversion converges to the global minimum [56,57].

As a result, the experimental data suggest that the transducers used in the experimental setup have an inhomogeneous performance, meaning they have a different sensitivity for each frequency, which results in strong artifacts when performing full waveform inversion.

6. Conclusion

The main contributions of this paper are as follows: (a) exploring the numerical performance of FWI under smooth defects of varying depths and locations, and (b) experimentally validating an accurate 2-D acoustic model, made artificially anisotropic using Thomsen parameters, with the necessary pre-processing (helical path separation and autocalibration), before integrating it with a classical FWI algorithm.

The inversion process involves selecting one frequency component from the guided wave signals and interpreting the encoded information using a two-dimensional acoustic model shaped by Thomsen parameters. The numerical efficiency of the 2-D acoustic forward model enables a rapid solution of the inverse problem. Consequently, a wall-thickness loss map of the entire elbow can be generated in less than 7 min on a standard PC.

Experimental and numerical validation has been carried out on a carbon steel pipe bend with a thickness of 8 mm, a 90-degree elbow, and a 1.5d radius of curvature. For the defects examined in the numerical study, FWI generally underestimated the maximum depth,

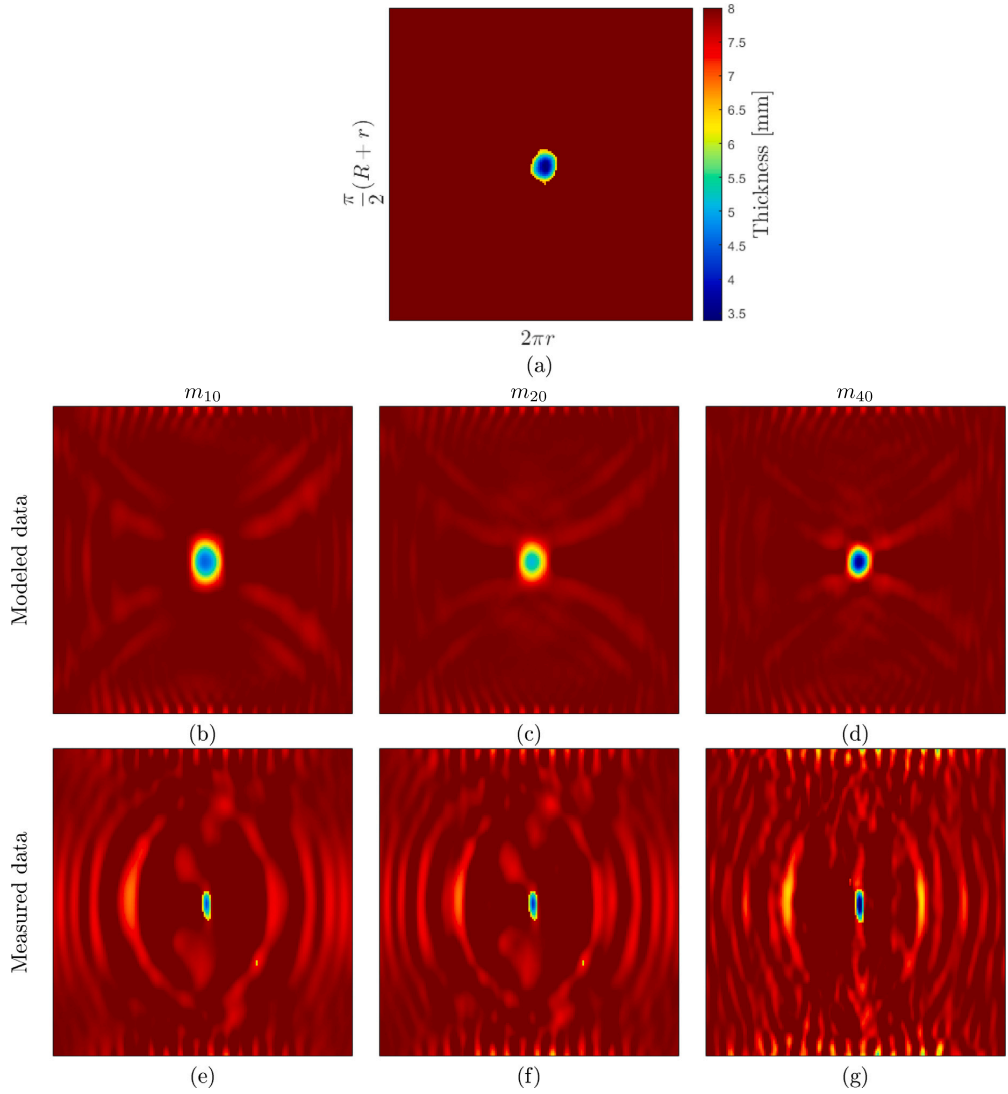


Fig. 11. Real thickness map (a). Reconstructed thickness map after 10, 20, and 40 iterations for the 3-D elastic modeled data (b)–(d) and the measured data (e)–(g).

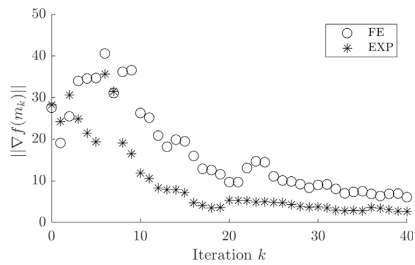


Fig. 12. The norm of the gradient misfit function with respect to the model parameter m_k for FWI reconstruction of the FE and measured data in terms of iterations.

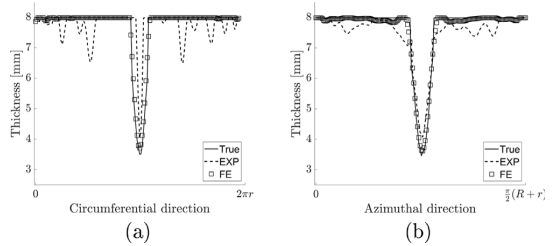


Fig. 13. Axial thickness profiles along the circumferential direction (a) and the azimuthal direction (b).

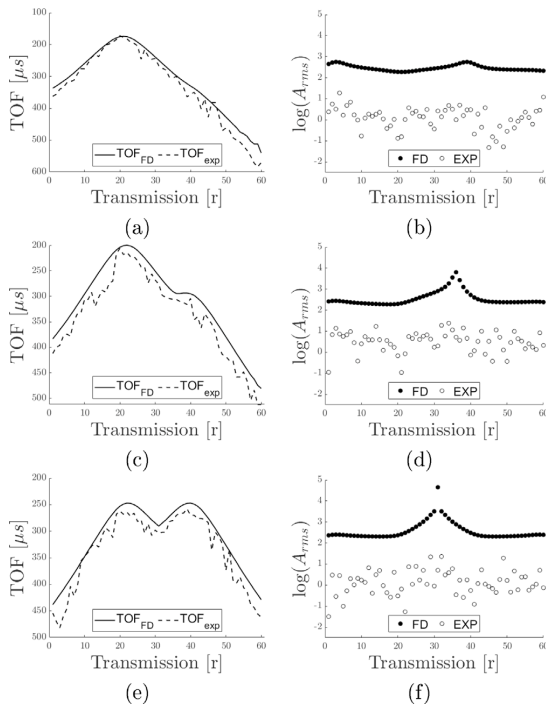


Fig. 14. Time-of-flight and logarithmic root-mean-square amplitudes from forward modeling and experimental measurements. Three crucial emission positions: intrados (a)–(b), top (c)–(d), and extrados (e)–(f).

resulting in relatively small errors ranging from 0.1% to 1.5% of the wall thickness in many cases. However, all the defects simulated were localized and had regular depth profiles, with the regions of maximum depth confined to a higher thickness loss. It has been demonstrated that the detection of thickness loss can be achieved regardless of the damage position around the bend and for defect sizes on the order of 100 mm in diameter. Compared to travel-time-based tomographic methods, FWI can map a defect independent of its circumferential location and without adding a line of transducers along the extrados.

The experimental validation was far from the real thickness map in the circumferential direction, mainly due to the strongly inhomogeneous transducer performance. In this work, we showed the impact of the amplitude mismatch between the synthetic and observed data in FWI. However, we demonstrated the robustness of the autocalibration method in anisotropic media when reconstructing the defect from elastic modeling data. The maximum reconstructed thickness resulted in an error of 0.7%, as previously reported [16].

Further research would cope with experimental uncertainties to improve the quality of the measured data using calibration methods such as reciprocity calibration or machine learning techniques. Additionally, it would consider improving the inversion scheme through threshold regularization or selecting proper values for Tikhonov regularization.

CRediT authorship contribution statement

Carlos-Omar Rasgado-Moreno: Writing – review & editing, Writing – original draft, Visualization, Validation, Software, Methodology, Investigation, Formal analysis, Data curation, Conceptualization. **Marek Rist:** Software, Methodology, Data curation. **Raul Land:** Software, Methodology. **Madis Ratassepp:** Writing – review & editing, Supervision, Resources, Project administration, Funding acquisition.

Declaration of competing interest

The authors declare the following financial interests/personal relationships which may be considered as potential competing interests: Madis Ratassepp reports financial support was provided by Estonian Research Council. Madis Ratassepp reports financial support was provided by European Commission.

Acknowledgments

The authors would like to thank Dr. Tom Druet and Dr. Arnaud Recoquilly for their guidance and comments regarding the autocalibration method.

Data availability

Data will be made available on request.

References

- [1] T. Hayashi, K. Kawashima, Z. Sun, J.L. Rose, Guided wave propagation mechanics across a pipe elbow, *Trans. ASME, J. Press. Vessel Technol.* 127 (3) (2005) 322–327, <http://dx.doi.org/10.1115/1.1990210>.
- [2] M. Talebi, M. Zeinoddini, M. Mo'tamedi, A. Zandi, Collapse of HSLA steel pipes under corrosion exposure and uniaxial inelastic cycling, *J. Constr. Steel Res.* 144 (2018) 253–269, <http://dx.doi.org/10.1016/j.jcsr.2018.02.003>, URL <https://www.sciencedirect.com/science/article/pii/S0143974X17311513>.
- [3] S. Livadiotis, A. Ebrahimkhanlou, S. Salamone, Monitoring internal corrosion in steel pipelines: A two-step helical guided wave approach for localization and quantification, *Struct. Health Monit.* 20 (5) (2020) 2694–2707, <http://dx.doi.org/10.1177/1475921720970139>.
- [4] B. Zima, R. Kedra, Detection and size estimation of crack in plate based on guided wave propagation, *Mech. Syst. Signal Process.* 142 (2020) 106788, <http://dx.doi.org/10.1016/j.ymssp.2020.106788>.
- [5] Z. Yan, L. Wang, P. Zhang, W. Sun, Z. Yang, B. Liu, J. Tian, X. Shu, Y. He, G. Liu, Failure analysis of Erosion–Corrosion of the bend pipe at sewage stripping units, *Eng. Fail. Anal.* 129 (2021) 105675, <http://dx.doi.org/10.1016/j.engfailanal.2021.105675>, URL <https://www.sciencedirect.com/science/article/pii/S1350630721005367>.
- [6] S.K. Dwivedi, M. Vishwakarma, P.A. Soni, Advances and researches on non-destructive testing: A review, *Mater. Today: Proc.* 5 (2, Part 1) (2018) 3690–3698, <http://dx.doi.org/10.1016/j.matpr.2017.11.620>, URL <https://www.sciencedirect.com/science/article/pii/S2214785317328936>.
- [7] C.A. Lebowitz, L.M. Brown, Review of progress in quantitative nondestructive evaluation, in: D.O. Thompson, D.E. Chimenti (Eds.), *Review of Progress in Quantitative Nondestructive Evaluation: Volumes 12A and 12B*, Springer US, Boston, MA, 1993, pp. 1987–1994, http://dx.doi.org/10.1007/978-1-4615-2848-7_255.
- [8] A. Verma, A. Kaiwart, N.D. Dubey, F. Naseer, S. Pradhan, A review on various types of in-pipe inspection robot, *Mater. Today: Proc.* (2021) <http://dx.doi.org/10.1016/j.matpr.2021.08.335>, URL <https://www.sciencedirect.com/science/article/pii/S2214785321057801>.
- [9] Z. Haiyan, C. Xianhua, Y. Jianbo, C. Yaping, Ultrasonic guided wave tomography of pipes, in: 2010 International Conference on Audio, Language and Image Processing, 2010, pp. 1729–1733, <http://dx.doi.org/10.1109/ICALIP.2010.5684369>.
- [10] K.R. Leonard, M.K. Hinders, Guided wave helical ultrasonic tomography of pipes, *J. Acoust. Soc. Am.* 114 (2) (2003) 767–774, <http://dx.doi.org/10.1121/1.1593068>, URL <https://asa.scitation.org/doi/10.1121/1.1593068>.
- [11] P.S. Lowe, R. Sanderson, S.K. Pedram, N.V. Boulgouris, P. Mudge, Inspection of pipelines using the first longitudinal guided wave mode, *Physics Procedia* 70 (2015) 338–342, <http://dx.doi.org/10.1016/j.phpro.2015.08.079>, URL <https://www.sciencedirect.com/science/article/pii/S1875389215008202>.
- [12] D. Jansen, D. Hutchins, Lamb wave tomography, in: *IEEE Symposium on Ultrasonics*, 1990, pp. 1017–1020, <http://dx.doi.org/10.1109/ULTSYM.1990.171515>, vol. 2.
- [13] S. Yan, B. Zhang, G. Song, J. Lin, PZT-based ultrasonic guided wave frequency dispersion characteristics of tubular structures for different interfacial boundaries, *Sensors* 18 (12) (2018) 4111, <http://dx.doi.org/10.3390/s18124111>.
- [14] Z. Song, X. Qi, Z. Liu, H. Ma, Experimental study of guided wave propagation and damage detection in large diameter pipe filled by different fluids, *NDT E Int.* 93 (2018) 78–85, <http://dx.doi.org/10.1016/j.ndteint.2017.10.002>.
- [15] S.C. Olisa, M.A. Khan, A. Starr, Review of current guided wave ultrasonic testing (GWUT) limitations and future directions, *Sensors* 21 (3) (2021) 811, <http://dx.doi.org/10.3390/s21030811>.

- [16] J. Rao, M. Ratassepp, Z. Fan, Guided wave tomography based on full waveform inversion, *IEEE Trans. Ultrason. Ferroelectr. Freq. Control* 63 (5) (2016) 737–745, <http://dx.doi.org/10.1109/tuffc.2016.2536144>.
- [17] M. Ratassepp, J. Rao, X. Yu, Z. Fan, Modeling the effect of anisotropy in ultrasonic guided wave tomography, *IEEE Trans. Ultrason. Ferroelectr. Freq. Control* (2021) <http://dx.doi.org/10.1109/TUFFC.2021.3114432>, 1–1.
- [18] C.L. Willey, F. Simonetti, P.B. Nagy, G. Instanes, Guided wave tomography of pipes with high-order helical modes, *NDT E Int.* 65 (2014) 8–21, <http://dx.doi.org/10.1016/j.ndteint.2014.03.010>, URL <http://www.sciencedirect.com/science/article/pii/S0963869514000449>.
- [19] Z. Wang, S. Huang, G. Shen, S. Wang, W. Zhao, High resolution tomography of pipeline using multi-helical lamb wave based on compressed sensing, *Constr. Build. Mater.* 317 (2022) 125628, <http://dx.doi.org/10.1016/j.conbuildmat.2021.125628>.
- [20] J. Li, J.L. Rose, Natural beam focusing of non-axisymmetric guided waves in large-diameter pipes, *Ultrasonics* 44 (1) (2006) 35–45, <http://dx.doi.org/10.1016/j.ultras.2005.07.002>.
- [21] A. Volker, T. van Zon, Guided Wave Travel Time Tomography for Bends, *AIP*, 2013, <http://dx.doi.org/10.1063/1.4789119>.
- [22] A.J. Brath, F. Simonetti, P.B. Nagy, G. Instanes, Guided wave tomography of pipe bends, *IEEE Trans. Ultrason. Ferroelectr. Freq. Control* 64 (5) (2017) 847–858, <http://dx.doi.org/10.1109/tuffc.2017.2683259>.
- [23] Y. Wang, X. Li, Elbow damage identification technique based on sparse inversion image reconstruction, *Materials* 13 (7) (2020) 1786, <http://dx.doi.org/10.3390/ma13071786>, URL <https://www.mdpi.com/1996-1944/13/7/1786>.
- [24] A.J. Brath, F. Simonetti, P.B. Nagy, G. Instanes, Acoustic formulation of elastic guided wave propagation and scattering in curved tubular structures, *IEEE Trans. Ultrason. Ferroelectr. Freq. Control* 61 (5) (2014) 815–829, <http://dx.doi.org/10.1109/TUFFC.2014.2973>.
- [25] J.L. Rose, L. Zhang, M.J. Avioli, P.J. Mudge, A natural focusing low frequency guided wave experiment for the detection of defects beyond elbows, *Trans. ASME, J. Press. Vessel Technol.* 127 (3) (2005) 310–316, <http://dx.doi.org/10.1115/1.1989350>.
- [26] A.J. Brath, F. Simonetti, P.B. Nagy, G. Instanes, Experimental validation of a fast forward model for guided wave tomography of pipe elbows, *IEEE Trans. Ultrason. Ferroelectr. Freq. Control* 64 (5) (2017) 859–871, <http://dx.doi.org/10.1109/tuffc.2017.2683264>.
- [27] R.G. Pratt, C. Shin, G.J. Hick, Gauss-Newton and full Newton methods in frequency-space seismic waveform inversion, *Geophys. J. Int.* 133 (2) (1998) 341–362, <http://dx.doi.org/10.1046/j.1365-246X.1998.00498.x>.
- [28] C. Shin, K. Yoon, K.J. Marfurt, K. Park, D. Yang, H.Y. Lim, S. Chung, S. Shin, Efficient calculation of a partial-derivative wavefield using reciprocity for seismic imaging and inversion, *Geophysics* 66 (6) (2001) 1856–1863, <http://dx.doi.org/10.1190/1.1487129>, URL <https://library.seg.org/doi/10.1190/1.1487129>.
- [29] J. Rao, M. Ratassepp, Z. Fan, Investigation of the reconstruction accuracy of guided wave tomography using full waveform inversion, *J. Sound Vib.* 400 (2017) 317–328, <http://dx.doi.org/10.1016/j.jsv.2017.04.017>, URL <https://www.sciencedirect.com/science/article/pii/S0022460X17303231>.
- [30] S. Operto, J. Virieux, A. Ribodetti, J.E. Anderson, Finite-difference frequency-domain modeling of viscoacoustic wave propagation in 2D tilted transversely isotropic (TTI) media, *Geophysics* 74 (5) (2009) T75–T95, <http://dx.doi.org/10.1190/1.3157243>.
- [31] C.-O. Rasgado-Moreno, M. Rist, R. Land, M. Ratassepp, Acoustic forward model for guided wave propagation and scattering in a pipe bend, *Sensors* 22 (2) (2022) 486, <http://dx.doi.org/10.3390/s22020486>, URL <https://www.mdpi.com/1424-8220/22/2/486>.
- [32] H. Zhou, G. Zhang, R. Bloor, An anisotropic acoustic wave equation for modeling and migration in 2D TTI media, in: *SEG Technical Program Expanded Abstracts 2006*, Society of Exploration Geophysicists, 2006, <http://dx.doi.org/10.1190/1.2369913>.
- [33] L. Thomsen, Weak elastic anisotropy, *Geophysics* 50 (10) (1986) 1954–1966, <http://dx.doi.org/10.1190/1.1442051>.
- [34] T. Alkhalifah, An acoustic wave equation for anisotropic media, *Geophysics* 65 (4) (2000) 1239–1250, <http://dx.doi.org/10.1190/1.1444815>.
- [35] L. Métivier, R. Brossier, The SEISCOPE optimization toolbox: A large-scale nonlinear optimization library based on reverse communication, *Geophysics* 81 (2) (2016) F1–F15, <http://dx.doi.org/10.1190/geo2015-0031.1>, arXiv:<https://doi.org/10.1190/geo2015-0031.1>.
- [36] Y.H. Dai, Y. Yuan, A nonlinear conjugate gradient method with a strong global convergence property, *SIAM J. Optim.* 10 (1) (1999) 177–182, <http://dx.doi.org/10.1137/S1052623497318992>, arXiv:<https://doi.org/10.1137/S1052623497318992>.
- [37] J.L. Rose, *Ultrasonic Waves in Solid Media*, Cambridge University Press, 2003, URL https://www.ebook.de/de/product/4208838/joseph_l_rose_ultrasonic_waves_in_solid_media.html.
- [38] *ABAQUS/Standard User's Manual, Version 6.14*, Dassault Systèmes Simulia Corp, United States.
- [39] M. Drozd, L. Moreau, M. Castaigns, M.J.S. Lowe, P. Cawley, Efficient numerical modelling of absorbing regions for boundaries of guided waves problems, *AIP Conf. Proc.* 820 (1) (2006) 126–133, <http://dx.doi.org/10.1063/1.2184520>, URL <https://aip.scitation.org/doi/abs/10.1063/1.2184520>.
- [40] P. Huthwaite, R. Ribichini, P. Cawley, M.J. Lowe, Mode selection for corrosion detection in pipes and vessels via guided wave tomography, *IEEE Trans. Ultrason. Ferroelectr. Freq. Control* 60 (6) (2013) 1165–1177, <http://dx.doi.org/10.1109/TUFFC.2013.2679>.
- [41] P. Huthwaite, Evaluation of inversion approaches for guided wave thickness mapping, *Proc. R. Soc. Lond. Ser. A Math. Phys. Eng. Sci.* 470 (2166) (2014) 20140063, <http://dx.doi.org/10.1098/rspa.2014.0063>, URL <https://royalsocietypublishing.org/doi/10.1098/rspa.2014.0063>.
- [42] P. Huthwaite, M. Seher, Robust helical path separation for thickness mapping of pipes by guided wave tomography, *IEEE Trans. Ultrason. Ferroelectr. Freq. Control* 62 (5) (2015) 927–938, <http://dx.doi.org/10.1109/tuffc.2014.006884>.
- [43] C.-O. Rasgado-Moreno, M. Ratassepp, Geodesic equations for guided wave helical path separation for a pipe bend, *Mech. Syst. Signal Process.* 204 (2023) 110820, <http://dx.doi.org/10.1016/j.ymssp.2023.110820>, URL <https://www.sciencedirect.com/science/article/pii/S0888327023007288>.
- [44] F. Simonetti, M. Alqaradawi, Guided ultrasonic wave tomography of a pipe bend exposed to environmental conditions: A long-term monitoring experiment, *NDT E Int.* 105 (2019) 1–10, <http://dx.doi.org/10.1016/j.ndteint.2019.04.010>, URL <http://www.sciencedirect.com/science/article/pii/S0963869519300684>.
- [45] J. Wen, C. Jiang, Y. Li, H. Chen, W. Ma, J. Wang, An auto-calibration algorithm for hybrid guided wave tomography based on full waveform inversion, *IEEE Access* 11 (2023) 62496–62509, <http://dx.doi.org/10.1109/ACCESS.2023.3287646>, URL <https://ieeexplore.ieee.org/abstract/document/10155413>.
- [46] T. Druet, J.-L. Tastet, B. Chapuis, E. Moulin, Autocalibration method for guided wave tomography with undersampled data, *Wave Motion* 89 (2019) 265–283, <http://dx.doi.org/10.1016/j.wavemoti.2019.04.002>, URL <https://www.sciencedirect.com/science/article/pii/S0165212518301781>.
- [47] M. Jørgensen, T. Halkjelsvik, K. Liestøl, When should we (not) use the mean magnitude of relative error (MMRE) as an error measure in software development effort estimation? *Inf. Softw. Technol.* 143 (2022) 106784, <http://dx.doi.org/10.1016/j.infsof.2021.106784>, URL <https://www.sciencedirect.com/science/article/pii/S0950584921002263>.
- [48] P. Huthwaite, A.A. Zwiebel, F. Simonetti, A new regularization technique for limited-view sound-speed imaging, *IEEE Trans. Ultrason. Ferroelectr. Freq. Control* 60 (3) (2013) 603–613, <http://dx.doi.org/10.1109/TUFFC.2013.2602>, URL <https://ieeexplore.ieee.org/document/6470421>.
- [49] J. Rao, M. Ratassepp, Z. Fan, Limited-view ultrasonic guided wave tomography using an adaptive regularization method, *J. Appl. Phys.* 120 (19) (2016) 194902, <http://dx.doi.org/10.1063/1.4967790>, URL <https://aip.scitation.org/doi/10.1063/1.4967790>.
- [50] A. Tikhonov, V. Arsenin, Solution of incorrectly formulated problems and the regularization method, *Sov. Math. Dokl.* 4 (1963) 1035–1038, URL <https://www.scopus.com/inward/record.uri?eid=s2.0-84975623675&partnerID=40&md5=a74b9d49416a77eab5890edd4bfcdf17>.
- [51] *Creaform, ACADEMIA 50 3D scanner*, 2019, URL <https://www.creaform3d.com>. (Accessed 09 April 2024).
- [52] X. Dong, T. Yuan, M. Hu, H. Shekhani, Y. Maida, T. Tou, K. Uchino, Driving frequency optimization of a piezoelectric transducer and the power supply development, *Rev. Sci. Instrum.* 87 (10) (2016) <http://dx.doi.org/10.1063/1.4963920>.
- [53] L. Métivier, F. Bretaudeau, R. Brossier, S. Operto, J. Virieux, Full waveform inversion and the truncated Newton method: quantitative imaging of complex subsurface structures, *Geophys. Prospect.* 62 (6) (2014) 1353–1375, <http://dx.doi.org/10.1111/1365-2478.12136>.
- [54] C. Lyu, Y. Capdeville, D. Al-Attar, L. Zhao, Intrinsic non-uniqueness of the acoustic full waveform inverse problem, *Geophys. J. Int.* 226 (2) (2021) 795–802, <http://dx.doi.org/10.1093/gji/ggab134>.
- [55] E. Hassefras, A. Volker, M. Verweij, Efficient guided wave modelling for tomographic corrosion mapping via one-way wavefield extrapolation, *Sensors* 24 (12) (2024) 3750, <http://dx.doi.org/10.3390/s24123750>, URL <https://www.mdpi.com/1424-8220/24/12/3750>.
- [56] A.J. Breders, R.G. Pratt, Full waveform tomography for lithospheric imaging: Results from a blind test in a realistic crustal model, *Geophys. J. Int.* 168 (1) (2007) 133–151, <http://dx.doi.org/10.1111/j.1365-246X.2006.03156.x>.
- [57] Z. Wang, S.C. Singh, M. Noble, True-amplitude versus trace-normalized full waveform inversion, *Geophys. J. Int.* 220 (2) (2020) 1421–1435, <http://dx.doi.org/10.1093/gji/ggz532>.

Appendix 4

IV.

Carlos-Omar Rasgado-Moreno, Panpan Xu, Marek Rist, and Madis Ratassepp. Optimising full waveform inversion with inhomogeneous transducers: Parameters and considerations for successful implementation. *NDT & E International*, 149:103265, January 2025



Contents lists available at ScienceDirect

NDT and E International

journal homepage: www.elsevier.com/locate/ndteint

Research Paper

Optimising full waveform inversion with inhomogeneous transducers: Parameters and considerations for successful implementation

Carlos-Omar Rasgado-Moreno ^{a,*}, Panpan Xu ^b, Marek Rist ^c, Madis Ratassepp ^a

^a Department of Civil Engineering and Architecture, Tallinn University of Technology, Ehitajate tee 5, 19086, Tallinn, Estonia

^b Department of Mechanical, Imperial Collage London, Exhibition Rd, South Kensington, SW7 2AZ, London, United Kingdom

^c Thomas Johann Seebeck Department of Electronics, Tallinn University of Technology, Ehitajate tee 5, 19086 Tallinn, Estonia



ARTICLE INFO

Keywords:

Autocalibration

Full waveform inversion

Tomography

Chirp

Experimental uncertainties

Guided waves

Structural health monitoring

ABSTRACT

Guided wave tomography (GWT) based full waveform inversion (FWI) is an emerging technique for structural health monitoring applications, primarily for plates and pipeline structures. Generally, FWI employs a two-dimensional (2-D) forward model to circumvent the high computational cost associated with the inversion scheme. Consequently, a re-scaling step is implemented to compensate for any potential discrepancies between the 2-D model and the observed data. Druet et al., (2019) introduced the autocalibration method, which utilises the information from the healthy rays to calibrate those rays that pass through the defect. In this method, only the phase information is re-scaled, given that phase information is the dominant factor in FWI. However, overlooking amplitude discrepancies might lead the inversion scheme to become trapped in a local minimum. In this study, we propose to include the amplitude information as well, following the autocalibration method. We use an updated autocalibration method to reconstruct a 100 mm wide defect on an 8 mm thick steel straight pipe with traditional GWT using the A_0 mode. This novel approach provides a more accurate representation of the defect and avoids becoming trapped in a local minimum, thereby improving the reliability and effectiveness of FWI. Furthermore, we offer guidance for the successful implementation of this method in the presence of inhomogeneous transducers, a common challenge in practical applications.

1. Introduction

The field of Structural Health Monitoring (SHM) has seen significant advancements in recent years, with Full Waveform Inversion (FWI) emerging as a powerful tool for subsurface and material characterisation [1,2]. FWI is an optimisation problem that aims to minimise the difference between the observed dataset and that predicted by a model, thereby providing high-resolution quantitative imaging of the structure [3].

FWI has a theoretical maximum resolution of half a wavelength [1]. It achieves a resolution of approximately 0.7 wavelengths for defects with gradual depth changes, such as thickness loss, when using acoustic modelling data, and around 1.5–2 wavelengths with elastic modelling data [4]. Additionally, FWI has been shown to be applicable to composite materials [5].

However, successful implementation of FWI is often challenged by the complexities associated with experimental uncertainties, such as temperature variations, transducer alignment, incoherent noise, inhomogeneous transducer performance, etc. [6–8]. Each experimental uncertainty can significantly affect the accuracy and efficiency of the

inversion process, particularly if the difference between the observed wavefield and the modelled wavefield used in FWI is greater than half a cycle, resulting in cycle-skipping [9].

In the realm of guided wave-based SHM, one of the primary sources of experimental uncertainty arises from transducers. Their influence is often overlooked in the model employed FWI imaging. Incorporating the transducer's impact on the experimentally measured signals into the simulation necessitates precise characterisation of the transducer performance [10]. This typically involves a series of electrical tests using specialised equipment, which can be inconvenient for industrial applications.

Contrastingly, the influence of transducer performance can be mitigated in the experimental signals through signal processing techniques. The experimental measurements can be described as follows:

$$d(t) = u(t) * h(t) + n(t), \quad (1)$$

with $u(t)$ being the modelled wavefield, $h(t)$ being the transfer function that describes the characteristics of the system and $n(t)$ being the additive noise, which is usually contributed by the random noise from

* Corresponding author.

E-mail address: carlos.rasgado@taltech.ee (C.-O. Rasgado-Moreno).

electrical system or environment [11]. * is the convolution in the time domain, which corresponds to a multiplication in the frequency domain. Naively, we could estimate the transfer function of the system $h(t)$ and then use it to compensate the experimentally measured wavefield to eliminate the influence of the transducer performance in the experimental signals. In the frequency domain, the transfer function of the system can be estimated using the Wiener filter as:

$$H(\omega) = \frac{D(\omega)U^*(\omega)}{|U(\omega)|^2 + \lambda} \quad (2)$$

with λ being a stabilisation constant to avoid boosting noise [12]. Nonetheless, this method relies on the accurate establishment of a reference model for the calculation of $U(\omega)$.

To address this limitation, Kober et al. proposed an in-situ calibration method [13], grounded on the principle of reciprocity [14]. This approach, however, requires frequency division in accordance with Eq. (2), leading to an increase in resolution in the frequency domain, at the cost of losing it in the time domain.

Furthermore, Volker and Van der Heiden [15] suggested reshaping the excitation source $S(\omega)$ to align with the desired transducer response $D(\omega)$, as opposed to measuring $H(\omega)$. The proposed method is expressed as:

$$\hat{S}(\omega) = \frac{D(\omega)S(\omega)U^*(\omega)}{|U(\omega)|^2 + \lambda}, \quad (3)$$

where $\hat{S}(\omega)$ represents the new excitation signal. However, for a conventional GWT array configuration, comprising s emissions and r transmissions, this would entail computing $s \times r$ new emissions and measuring each individual transmitted signal $s \times s \times r$ times.

The primary drawback of the aforementioned compensation techniques is the requirement of a baseline measurement for subsequent processing. This demands measuring the transfer function $H(\omega)$ from a damage-free condition; otherwise, the scattered wavefield interacting with a flaw would be incorporated into $H(\omega)$. However, the measurements from a damage-free condition are not always available in practical applications.

On the other hand, artificial intelligence (AI) in combination with optimisation-based design and control of dynamic systems [16] can significantly enhance the calibration of ultrasonic transducers by automating and optimising the process [17]. Machine learning algorithms, such as neural networks, can analyse vast amounts of transducer data to identify patterns and predict optimal calibration settings [18]. These AI models can dynamically adjust parameters to account for variations in material properties, temperature, damages and other environmental factors, ensuring consistent and accurate measurements [19–21]. Additionally, AI enables adaptive calibration, where the system continuously learns and improves its performance over time, leading to more precise and reliable ultrasonic measurements [22]. However, a major drawback of AI is the requirement for large datasets to train these models effectively, which can be resource-intensive and time-consuming to gather [17].

To overcome the limitations of compensation techniques and AI, Druet et al. [23] introduced an autocalibration method that uses the information from the healthy rays that does not pass through the defect to estimate $H(\omega)$. This approach effectively reduces the discrepancy between the observed wavefield and the synthetic model used in the inversion scheme, while eliminating the need for baseline measurements from a damage-free structure. However, traditional autocalibration primarily considers the phase information, given that the phase information dominates the inversion scheme [24]. However, overlooking amplitude discrepancies might lead the inversion scheme to become trapped in a local minimum.

Therefore in this paper, we follow the autocalibration principle to delve into the parameters and considerations necessary for optimising FWI in practical applications, considering the presence of highly inhomogeneous transducers. Our goal is to enhance the understanding of the impact of these transducer performance on FWI and provide

practical guidelines for their successful implementation. This paper is divided as follows, theory regarding FWI is described in Section 2. Then, Section 3 describes the configuration of the problem for this study, followed by the methodology in Section 4. Results are presented and discussed in Section 5 and conclusions are drawn in Section 6.

2. Theory

The propagation of Guided Waves (GW) in an isotropic plate is presumed to resemble the behaviour of an acoustic wave moving in a two-dimensional medium with a constant speed. Consequently, the frequency-domain equation for a 2-D acoustic wave in a medium with uniform density is presented [25]:

$$(\nabla^2 + K^2)u(x, y, \omega) = -s(x, y, \omega), \quad (4)$$

where $u(x, y, \omega)$ describes the pressure field of the propagating wave, $s(x, y, \omega)$ the source, ω the angular frequency, and $K(x, y, \omega) = \omega/v(\omega)$ is the wave number linked with the phase velocity $v(\omega)$. Eq. (4) represents a simplification of the intricate three-dimensional domain and is used alongside the Finite Difference (FD) technique to circumvent the high computational expense associated with Finite Element elastic wave modelling [26].

Furthermore, Eq. (4) facilitates the estimation of the wavefield data $\mathbf{u}(\mathbf{m}(\omega))$, as a function of the angular frequency ω , given a specific emission–transmission setup and a particular set of parameters, \mathbf{m} , defined at each point (x, y) . Consequently, for the inversion scheme, our objective is to identify a set of model parameters, \mathbf{m} , that enables the computation of the synthetic wavefield, \mathbf{u} , which aligns with the observed wavefield \mathbf{d} as closely as possible. We define the residual error as:

$$\Delta \mathbf{d} = \mathbf{u}(\mathbf{m}) - \mathbf{d}(\mathbf{m}), \quad (5)$$

(with an implicit dependency on ω), where $\mathbf{u}(\mathbf{m})$ is the wavefield calculated by Eq. (4), and $\mathbf{d}(\mathbf{m})$ is the observed wavefield. Our goal is to identify \mathbf{m} such that $\Delta \mathbf{d}$ is minimised. Therefore, the inverse problem is formulated to minimise the sum of squared residuals:

$$\min_{\mathbf{m}} f(\mathbf{m}) = \frac{1}{2} \Delta \mathbf{d}^T \Delta \mathbf{d}, \quad (6)$$

where $\min_{\mathbf{m}} f(\mathbf{m})$ denotes the L_2 -norm misfit function, and $\Delta \mathbf{d}^T$ represents the conjugate transpose of the residual error $\Delta \mathbf{d}$. It is crucial to note that the least-squares norm method, which is utilised in the inversion scheme, presumes a Gaussian distribution. As a result, suboptimal results are expected when there are large amplitude variations in the sample data [3].

In this research, the non-linear waveform inversion problem is solved with the Seiscope Optimisation Toolbox [27]. The Seiscope Optimisation Toolbox addresses the inversion problem using the gradient method: starting with an initial model (observed data) and, an initial forward-modelling step is executed to compute the data residuals in Eq. (5). New models are iteratively derived by updating \mathbf{m} according to

$$\mathbf{m}_{k+1} = \mathbf{m}_k - a_k \Delta m_k, \quad (7)$$

where k denotes the iteration count, a is the scalar magnitude of the model update, and Δm_k is the gradient of the misfit function in respect to the model parameters as:

$$\Delta m_k = -Q_k \nabla f(\mathbf{m}_k), \quad (8)$$

with $-Q_k$ being the inverse Hessian operator and $\nabla f(\mathbf{m}_k)$ the gradient of the objective function.

3. Configuration of the problem

For numerical modelling and experimental measurements, we considered a steel pipe specimen with an inner radius r_{in} of 0.1015 m, an outer radius r_{out} of 0.1095 m, and a length of 2 m, as shown in Fig. 1.

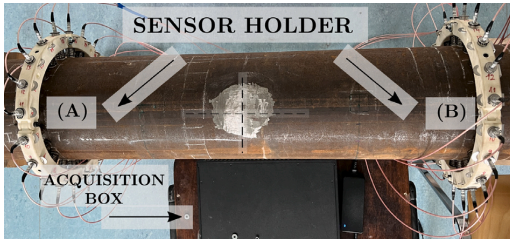


Fig. 1. Pipe specimen and experimental setup.

Table 1
Steel pipe mechanical properties.

Density ρ (kg/m ³)	Young's modulus E (GPa)	Poisson ratio ν
7932	216.9	0.2865

The material properties of the pipe are listed in Table 1.

As shown in Fig. 1, 20 transducers were mounted on the pipe using a spring-like mechanism to apply radial excitation. These transducers, produced by Doppler, Ltd., Guangzhou, China, were evenly distributed among each transducer ring (A-B). They were positioned 0.6 m from each edge of the pipe to prevent reflections with the pipe's boundaries, resulting in a separation distance of 0.8 m between them as shown in Fig. 1. A multiplexer and a data acquisition box were employed in the experiment for signal excitation and data acquisition. More information about the instrumentation can be found in [28].

All transducers in the two rings were excited sequentially, while the transducers on the opposite ring simultaneously measured the transmission of the A_0 waves. This process gathered a total of 800 time-trace signals.

A smooth defect with a radius of 100 mm and a thickness reduction of 47% was created using an angle grinder, as illustrated in Fig. 1. The defect is positioned at the centre of the pipe, hence 1 m from each pipe end and 0.4 m from each transducer ring.

Following this, we used the Creaform's ACADEMIA 50 scanner [29] to measure the remaining thickness of the pipe. The scanner employs structured white light technology, which projects structured light onto an object and uses cameras to capture the deformation of the light pattern. We processed this data to generate a detailed 3-D model of the pipe. This model was subsequently used to compare against the remaining wall-thickness map derived from the acoustic model described later in the text.

4. Methodology

4.1. Selection of transducers

To ensure uniformity in transducer performance, 40 transducers were selected from a pool of 120 based on a statistical analysis of their performance metrics. The frequency response of all 120 transducers was measured using a Digilent oscilloscope [30].

Figs. 2(a) and (b) display a histogram of the recorded resonance frequencies and the impedance resistance as a function of frequency, respectively. The resonance frequency was chosen as the maximum value from the impedance resistance curve for each transducer. Two data distributions were observed in Fig. 2(a). Thereby, we selected the distribution with the highest number of transducers. Then, we reduced the confidence interval from 95% in 5% increments until it encompassed at least 40 transducers, resulting in a 75% confidence interval, as shown in Fig. 2(b).

Moreover, in Fig. 2(b), the variance in transducer performance increases post their resonance frequency. This is attributed to the fact

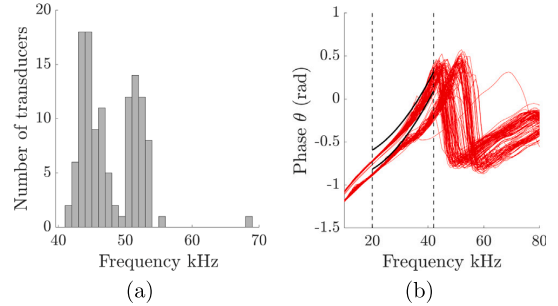


Fig. 2. Histogram of the 120 resonance frequencies (a), and impedance resistance as a function of frequency (b). In (b), the dashed lines illustrate the most reliable interval to operate the transducers among the distribution with the highest number of transducers, likewise, the solid lines contain the transducers with a 75% confidence interval.

that a piezoelectric transducer generates substantial heat at resonance, leading to decreased efficiency [31]. In Fig. 2(b), the dashed lines demarcate the interval where the transducers have the most uniform performance for operation.

4.2. Chirp excitation

In this study, we utilised a broadband chirp with a frequency range of 10 to 80 kHz to acquire data across a wide spectrum. Subsequently, deconvolution techniques were applied to extract multiple narrowband responses [32]. The use of chirp excitation not only facilitates better energy generation, leading to a higher signal-to-noise ratio, but also allows for the testing of multiple frequencies from a single measurement, thereby significantly reducing acquisition time.

For a typical chirp,

$$s_c(t) = w(t) \sin \left(2\pi f_0 t + \frac{\pi B t^2}{T} \right) \quad (9)$$

with f_0 being the starting frequency, T the duration of the chirp, B the chirp bandwidth, and $w(t)$ a unit amplitude rectangular window ranging $[t, T]$. A long-duration narrowband chirp, $s_c(t)$, is used as the actual excitation. The desired toneburst response, $r_d(t)$, corresponding to each desired toneburst excitation, $s_d(t)$, with different frequencies and durations, can be extracted in the frequency domain from the transmitted chirp response, $r_c(t)$, as follows:

$$R_d(\omega) = R_c(\omega) \frac{S_d(\omega)}{S_c(\omega)} \quad (10)$$

where the capital letters denote the Fourier transform and ω is the angular frequency. In this study, deconvolution as an inverse filter [12] was employed to circumvent the issue of division by zero in Eq. (10).

4.3. Helical path separation

The 2-D acoustic model outlined in Eq. (4) does not account for the cyclic nature of the pipe within a specific inspection area defined by a pair of transducer rings. To separate the first transmitted wavepacket from the experimental data, we employed a robust helical path separation algorithm [33].

In this algorithm, the time-traces $u_{r,s}(t)$, which are initiated from emission s and received at transmission r , are replicated m times to form $u_{r+Nm,s}(t)$. Here, N represents the total number of sources, m is the number of copies, and Nm is the increment in each receiver transducer number.

The first wavepacket $u_{r,s}^{hp}(t)$ is isolated from the original replicated time traces $u_{r,s}(t)$ by minimising the waveforms associated with other copies. This can be mathematically expressed as

$$u_{r,s}^{hp}(t) = u_{r,s}(t) - \phi_{r+Nm,s}(t), \quad (11)$$

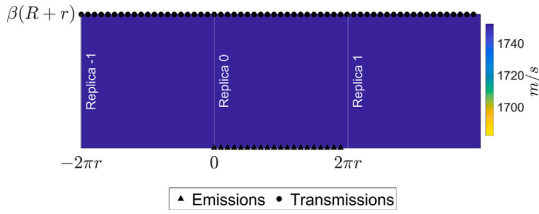


Fig. 3. 2D acoustic model used in the inversion scheme and the configuration of emissions and transmissions.

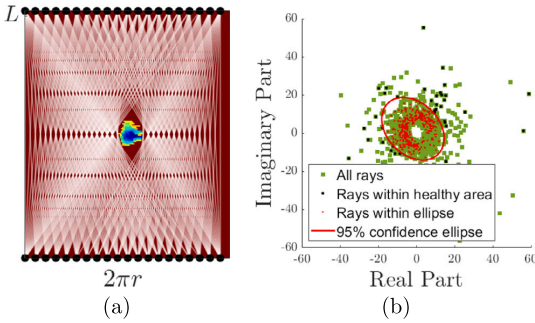


Fig. 4. All the rays used in order to calibrate $D_{r,s}$ (a), and calibration factors $Q_{r,s}$ plotted in the complex plain (b). The black dots denote the location of the transducers.

where $\phi_{\bar{r}+N_{m,s}}(t)$ is the resultant wavefield obtained by time-reversing $u_{r,s}(t)$, applying a series of band-pass filters, windows, and then forward propagating it again. The detailed procedure for helical path separation can be found in [33].

4.4. Acoustic modelling

We conducted the simulations in the acoustic domain using the FD method with the mixed-grid approach [34]. We computed the image reconstructions for 2-D modelled data and experimental measurements by taking into account all wave packets that have completed up to three full revolutions around the pipe. The 2-D domain comprised two identical replicas, as illustrated in Fig. 3. We discretised each replica using $4.143 \times 4.143 \text{ mm}^2$ square elements, resulting in 481×194 nodes (circumferential–axial). We positioned the emissions at the central replica, while the transmissions were placed in all replicas. This setup was designed to include higher-order helical wave paths.

Computations were executed using a 2-D frequency-domain engine called TOY2DAC [27] to address the minimisation problem described by Eq. (6) for a given frequency. We employed the Fast Fourier Transform to convert the results from the time-domain into the frequency-domain. The phase velocity was the parameter to be inverted at a specified frequency, and the residual thickness maps were interpolated by using the velocity–frequency–thickness dispersion curve of the A_0 mode. A high-performance computing cluster (HPC) equipped with 2 x Intel Xeon E5-2660v2 and 64 GB RAM was utilised for the computations, with the calculation time amounting to 15 s for a single frequency.

Note that the 2-D FD model serves as a simplified representation of the high-fidelity 3-D wave propagation model. This approximation can impose certain constraints on the inversion process, particularly if the data employed for modelling exhibit significant divergence from the 2-D model [35].

4.5. Autocalibration

In order to reduce any potential inconsistencies between the acoustic model and the observed data that is not from the defect, it is crucial for us to adjust the observed data in relation to the acoustic model [1]. Traditionally, the calibration factor Q is calculated as

$$Q_{r,s} = \frac{U_{r,s}(\omega)}{D_{r,s}(\omega)}, \quad (12)$$

where $U_{r,s}$ and $D_{r,s}$ represent the data transmitted from transmission r to emission s predicted by FD modelling and the observed data in the frequency domain, respectively.

In our approach, we adopt the autocalibration method proposed in [23] for the adjustment step. This method involves identifying time-traces that go through the defect and those that do not. Subsequently, the *healthy* or defect-free time-traces, which do not pass through the defect, are used to compute the mean \bar{Q}_ψ of the calibration factor. In essence, $Q_{r,s}$ is constructed in three steps:

- I. **Positioning the defect.** Initially, a background velocity model, that highlights the location of the defect, needs to be computed. This can be accomplished by ray-tomography based algorithms [23].
- II. **Identifying defect-free rays.** Subsequently, all the ray-paths $U_{r,s}^d$ close to the flaw are excluded, with a threshold distance of 1%, leaving only the healthy rays $U_{r,s}^h$ for the next step.
- III. **Determining the confidence region.** Finally, a 95% confidence ellipse is computed for determining the calibration factors $Q_{r,s}^p$ from all *healthy* ray-paths $U_{r,s}^h$. The calibration factors for all the ray paths outside of the ellipse are set to the mean \bar{Q}_ψ of the rays within the ellipse:

$$\bar{Q}_\psi = \frac{1}{P} \sum_{p=1}^P (Q_x^p + iQ_y^p), \quad (13)$$

where Q_x^p and Q_y^p denote the real and imaginary components of the calibration factor Q^p , respectively. Here, p represents the index number of the *healthy* ray paths, from which the calibration factor is calculated.

For FWI, the defect location can also be identified by directly performing Step III with a low confidence level (e.g. 65%). A smaller confidence interval is chosen because the data will diverge significantly due to the inclusion of unhealthy rays. However, Steps I and II are later needed to concentrate the data in one region by removing the unhealthy rays based on their proximity with the defect.

Note that $Q_{r,s}$ is a complex number and can be represented as $Q = ze^{i\psi}$, where ψ is the phase and z is the amplitude, defined as $z = |Q_x + iQ_y|$. However, Eq. (13) primarily includes the phase information, since \bar{Q}_ψ is the geometrical mean of the distribution of Q^p points. Consequently, \bar{Q}_ψ does not maintain the modulus mean or amplitude \bar{z} , considering that \bar{z} is the mean distance from the origin to the position Q^p . Therefore, it follows that $|\bar{Q}_\psi| \neq \bar{z}$.

Furthermore, if the amplitudes of the observed data are not calibrated, the risk of becoming trapped in a local minimum during the inversion is increased [24,36]. Therefore, it is proposed to include the amplitude information in the autocalibration method as follows:

$$\bar{Q} = \frac{1}{P^2} \sum_{p=1}^P (Q_x^p + iQ_y^p) \cdot \sum_{p=1}^P |Q_x^p + iQ_y^p| = \bar{Q}_\psi \bar{Q}_z. \quad (14)$$

Note that \bar{Q} was redefined as the product of \bar{Q}_ψ that carries the mean phase information by \bar{Q}_z that carries the mean amplitude information. Fig. 4(a) shows the velocity field of a straight pipe with an arbitrary defect located at the centre of the surface where the black dots denote the position of the transducers. The defect was located by computing a 65% confidence ellipse with all the transmitted measurements and setting $Q_{r,s} = \bar{Q}$ for those rays outside of the confidence ellipse. Then, in Fig. 4(b) those rays in close proximity with the flaw have been excluded to compute the final calibration factors $Q_{r,s}$.

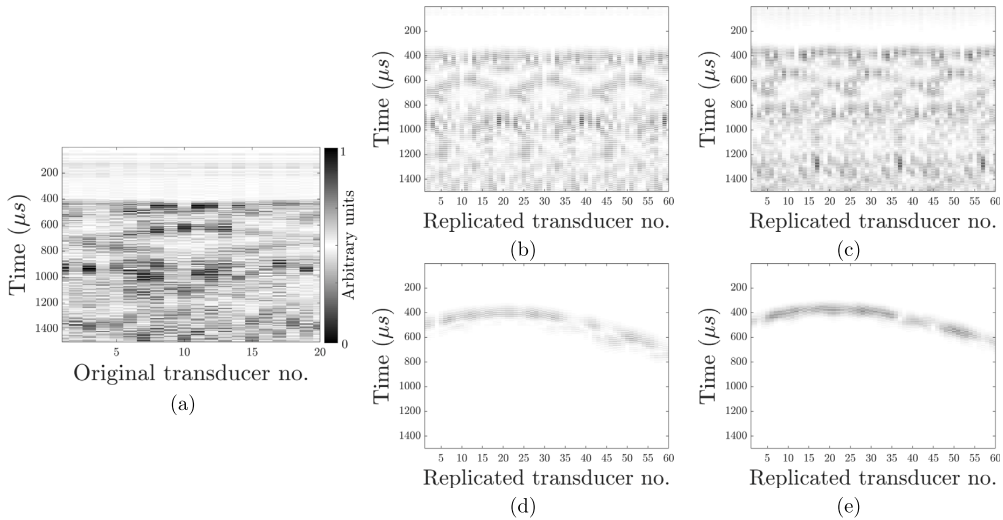


Fig. 5. Measured wavefield with a chirp excitation (a). Filtered wavefields for a Hann-shaped toneburst with central frequencies at 35 kHz (b) and 43 kHz (c), replicated 3 times, and their respective helical path separated wavefields (d) and (e).

5. Results and discussion

A broad-band chirp was excited as described in Section 4 and sent to the data acquisition system for each transducer. The transmitted chirp was measured in the opposite ring, digitally filtered, and logged, resulting in 800 time-traces. Fig. 5(a) presents the transmission of the A_0 mode from one ring across 20 transducers; signals were averaged 50 times.

We aimed to evaluate the performance of FWI at the resonant frequency of the transducers and at a lower frequency, where the transducer showed a more homogeneous response, as previously shown in Fig. 2(b). Therefore, we extracted a 5-cycle Hann-shaped toneburst with central frequencies at 30 kHz and 43 kHz, as shown in Figs. 5(b)–(c), respectively. This procedure aims to enhance the signal-to-noise ratio compared to a traditional centred frequency toneburst, since other frequencies outside the desired tone burst are filtered out.

In Figs. 5(b)–(c), the resulting wavefields were replicated three times to facilitate the extraction of the first arrived wave packets, as illustrated in Figs. 5(d)–(e). It is important to note that the difference in time-of-flight in Figs. 5(d)–(e) is determined by the phase velocity of the A_0 mode for each central frequency, specifically 1424 m/s and 1652 m/s at 30 kHz and 43 kHz, respectively. Furthermore, the Doppler ultrasonic transducers utilised in this study are optimised to predominantly excite the A_0 mode. Additionally, the robust helical path separation effectively minimises any additional modes through a series of band-pass filters [33].

Thereafter, considering the thickness loss from Fig. 6(a), we computed a monochromatic reconstruction of the thickness for acoustic modelled data at 30 kHz and experimental measurements, at 30 kHz and 43 kHz. In addition, we studied two FWI cases: (i) uncalibrated amplitudes (original autocalibration), and (ii) calibrated amplitudes (updated autocalibration), as shown in the second and third row of Fig. 6. Moreover, Fig. 7 illustrates the axial thickness profiles along the circumferential direction. For both cases, results were obtained after 40 iterations. In case (i), we re-scaled the measured data following Eq. (13), taking into account only the phase information for the autocalibration method, whereas, in case (ii) the amplitude information was also included according to Eq. (14). Computations on the HPC were performed with an average completion time of 220 s for 40 iterations.

5.1. Original autocalibration

To evaluate the impact of the mean amplitude ratio \bar{Q}_z on the thickness map reconstruction, we used the acoustic model of the defective pipe depicted in Fig. 6 to generate the data, which served as the observed data in FWI reconstruction. The FWI process was performed at 30 kHz using different amplitude ratios $\bar{Q}_z = A |\bar{Q}_\psi|$, with $A = 1, 2, 3, 4$.

Results showed that when $\bar{Q}_z > 4$, FWI gets trapped in a local minimum, resulting in thickening as illustrated in Figs. 6(b) and 7(a). For simplicity, thickness map reconstructions from $\bar{Q}_z < 4$ were excluded from the results since they were converging to the correct solution at the expense of higher artefacts.

Then, we computed FWI for the extracted experimental wavefields at 30 kHz and 43 kHz, as shown in Figs. 6(c) and (d), following the original autocalibration method described by Eq. (13), i.e., $A = 1$. At a glance, the FWI seems to have converged in the right location, since the location of the defect is visible for both cases. However, the thickness map reconstruction resulted in thickening. Thickening was expected given $\bar{Q}_z > 9$ for the experimental measurements.

The large ratio \bar{Q}_z in the experimental measurements can be attributed to the inhomogeneous response of the transducers, mainly coming from coupling conditions, positioning, aging of the transducers, etc.

5.2. Updated autocalibration

On the other hand, we computed FWI by including \bar{Q}_z in the autocalibration method, following Eq. (14). In addition, to quantitatively evaluate the wall-thickness loss maps reconstruction, we used the *mean magnitude of relative error* (MMRE) of the residuals between the true wall-thickness map T and the reconstructed \hat{T} wall-thickness maps. The MMRE is the mean of the ratios of the absolute difference between two values to the magnitude of one of the values [37]. For a total of n ratios,

$$MMRE = \frac{1}{n} \sum_{i=1}^n \frac{|T_i - \hat{T}_i|}{T_i}. \quad (15)$$

FWI reconstruction based on the acoustic model resulted in an MMRE of 0.5%. In Fig. 6(e), the lack of accuracy in the shape of the defect can be attributed to the inhomogeneous shape and depth of the defect, as shown in Fig. 6(a).

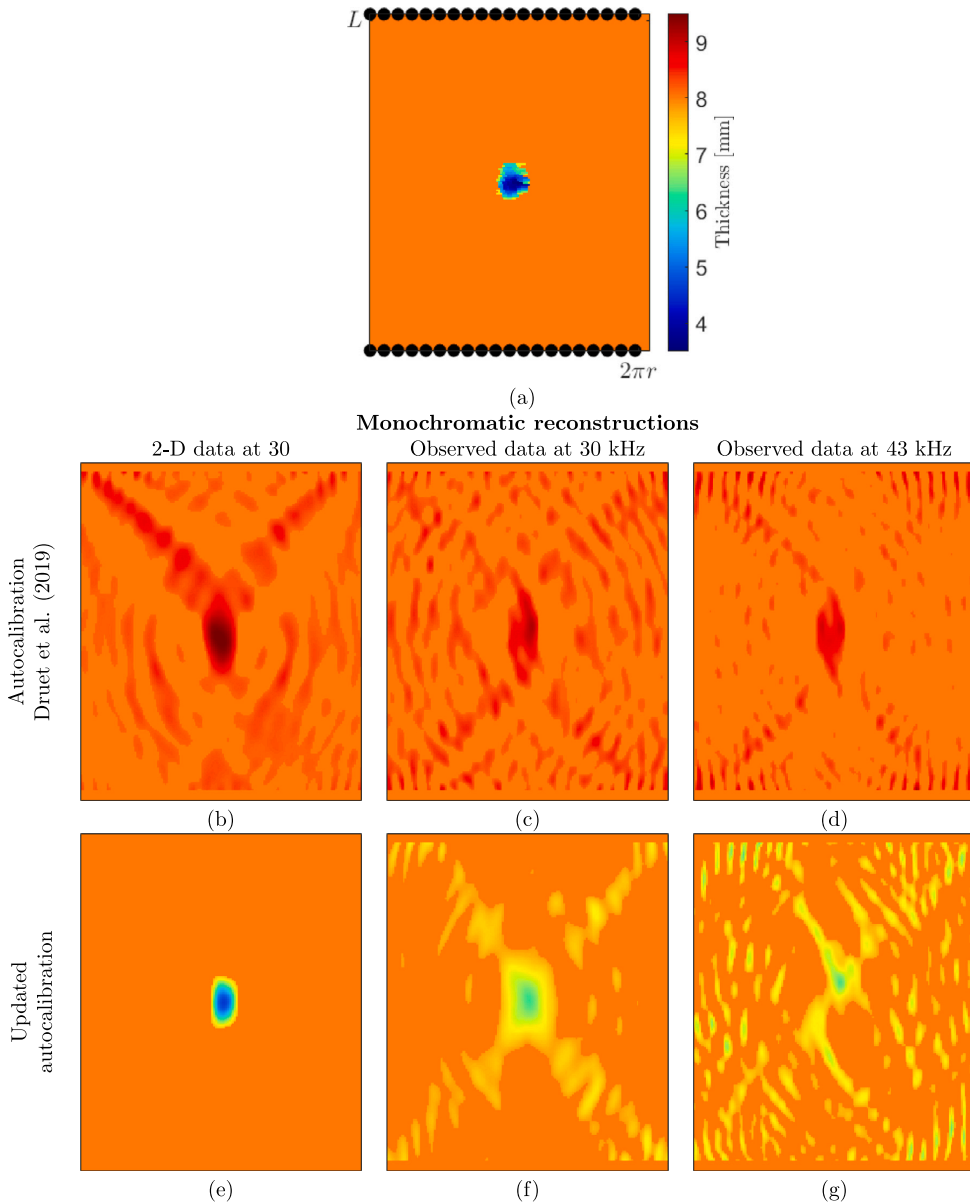


Fig. 6. Real thickness map (a). Reconstructed thickness map using the original autocalibration method introduced by [23] without amplitude calibration for the acoustic modelled data (b), and experimental data at 30 kHz (c) and 43 kHz (d). Reconstructed thickness map using the updated autocalibration method with amplitude calibration for 2-D data (e), and experimental data at 30 kHz (f) and 43 kHz (g).

Furthermore, FWI results based on the experimental data with calibrated amplitudes at 30 kHz and 43 kHz are illustrated in Figs. 6(f) and (g), respectively. Even though FWI results at 30 kHz showed the correct location of the defect with an MMRE of 0.9%, only 40% of the maximum depth was achieved as shown by the dashed line in Fig. 7(b). Note that the acoustic forward model used in the inversion scheme is an approximation of the elastic model, and a higher error was expected from the experimental data.

In contrast, the thickness map reconstruction at 43 kHz resulted in higher artefacts. In this case, the reconstructed defect appeared at the

wrong location and is almost merged with the artefacts. The MMRE was 15.66%, 17 times higher than that at 30 kHz.

It is evident that at the resonant frequency, where the response of the transducers is highly inhomogeneous, the calibration factors Q^p will differ greatly from one another, resulting in a mean calibration factor \bar{Q} that does not calibrate the data properly. This is why in Fig. 6(g), the defect appeared in the wrong location.

To further illustrate the contrast in the FWI reconstruction between the original and updated autocalibration methods, Fig. 8 presents

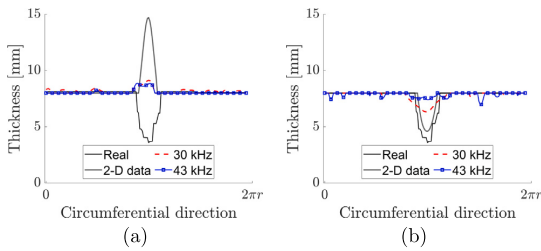


Fig. 7. Axial reconstructed thickness maps along the circumferential direction for the uncalibrated (a) and calibrated (a) amplitudes.

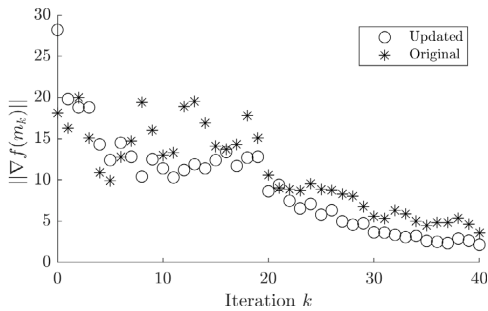


Fig. 8. Gradient of the objective function for the FWI reconstruction using the original and updated autocalibration methods for the observed data at 30 kHz.

the gradient of the objective function at each iteration for the observed data at 30 kHz, as previously shown in Fig. 6(c) and (f). Although the evolution of both gradients is similar, the gradient for the updated autocalibrated data is consistently smaller after 10 iterations. Consequently, computational times are 200 and 247 s for the updated and original autocalibrated data, respectively. Note that, although both gradients decrease after each iteration, the original autocalibrated data converged into a false thickness map reconstruction due to the non-uniqueness phenomena in FWI [38,39].

6. Conclusion

In this paper, we presented an experimental and numerical demonstration of guided wave tomography based on FWI of a straight pipe, with highly inhomogeneous transducers. The inversion process involves selecting one frequency component from the guided wave signals and interpreting the encoded information using a two-dimensional acoustic model. The numerical efficiency of the 2-D acoustic forward model enables a rapid solution of the inverse problem.

Experimental and numerical validation has been carried out on a carbon steel pipe with a thickness of 8 mm. We demonstrated that high divergence in the mean amplitude between the modelled and observed experimental data can result in the inversion scheme getting trapped in a local minimum and increasing computational time. Thereby, we proposed an updated autocalibration to re-scale the observed data.

In summary, our strategy for successful implementation of FWI on experimental signals consists of the following major steps:

1. Quality control of the input data by (i) evaluating the transducers' performance, (ii) selecting the source's central frequency, and (iii) exciting a chirp function.

2. Performing the autocalibration procedure to compensate for the discrepancy between the acoustic model data and the experimental data, thereby enhancing the accuracy of inversion.

Future research may focus on integrating machine learning methods and control theory to address experimental uncertainties and enhance imaging reconstruction. By leveraging AI and machine learning algorithms, extensive datasets can be analysed to identify patterns and predict an optimal transfer function $H(\omega)$. Additionally, control theory, especially through the application of Kalman filters, can provide real-time adjustments and noise reduction, further refining the calibration process. This combined approach promises significant advancements in the precision and reliability of ultrasonic transducer calibration and damage detection. Moreover, future research may explore the capabilities of FWI, in combination with the proposed autocalibration method, to detect and characterise a wider range of defects across various materials and structural components. Such exploration could offer further insights into the versatility and robustness of FWI when paired with baseline-free calibration methods.

Funding

This research was funded by the European Union's Horizon 2020 Research and Innovation Programme under grant agreement no. 860104, project GW4SHM (Guided Waves for Structural Health Monitoring), and the Estonian Research Council, Estonia, grant PRG737.

CRedit authorship contribution statement

Carlos-Omar Rasgado-Moreno: Writing – review & editing, Writing – original draft, Visualization, Validation, Supervision, Software, Project administration, Methodology, Investigation, Formal analysis, Data curation, Conceptualization. **Panpan Xu:** Writing – review & editing, Investigation, Formal analysis, Data curation. **Marek Rist:** Methodology, Data curation. **Madis Ratassep:** Writing – review & editing, Supervision, Funding acquisition.

Declaration of competing interest

The authors declare the following financial interests/personal relationships which may be considered as potential competing interests: Madis Ratassep reports financial support was provided by Estonian Research Council. Madis Ratassep reports financial support was provided by European Commission.

The authors would like to thank the SHM team from CEA and Jochen Moll for their insights into the experimental uncertainties. Additionally, they thank Prof. Fco. Alaffita's comments regarding the complex plane.

Data availability

Data will be made available on request.

References

- [1] Rao J, Ratassep M, Fan Z. Guided wave tomography based on full waveform inversion. *IEEE Trans Ultrason Ferroelectr Freq Control* 2016;63(5):737–45. <http://dx.doi.org/10.1109/tuffc.2016.2536144>.
- [2] Aktharuzzaman M, Anwar S, Borisov D, He J. Experimental full waveform inversion for elastic material characterization with accurate transducer modeling. *Mech Syst Signal Process* 2024;213:111320. <http://dx.doi.org/10.1016/j.ymssp.2024.111320>, URL <https://www.sciencedirect.com/science/article/pii/S0888327024002188>.
- [3] Virieux J, Operto S. An overview of full-waveform inversion in exploration geophysics. *Geophysics* 2009;74(6):WCC1–26. <http://dx.doi.org/10.1190/1.3238367>, URL <https://library.seg.org/doi/10.1190/1.3238367>.

- [4] Rao J, Ratassepp M, Fan Z. Investigation of the reconstruction accuracy of guided wave tomography using full waveform inversion. *J Sound Vib* 2017;400:317–28. <http://dx.doi.org/10.1016/j.jsv.2017.04.017>, URL <https://www.sciencedirect.com/science/article/pii/S0022460X17303231>.
- [5] Ratassepp M, Rao J, Yu X, Fan Z. Modeling the effect of anisotropy in ultrasonic guided wave tomography. *IEEE Trans Ultrason Ferroelectr Freq Control* 2021;1. <http://dx.doi.org/10.1109/TUFFC.2021.3114432>.
- [6] Rose JL. Successes and challenges in ultrasonic guided waves for NDT and SHM. e-J Nondestruct Test 2010;15(11). URL <https://www.ndt.net/search/docs.php?id=9801&msgid=0&rootID=0>.
- [7] Li J, Lu K, Hanafy S, Schuster G. Two robust imaging methodologies for challenging environments: Wave-equation dispersion inversion of surface waves and guided waves and supervirtual interferometry + tomography for far-offset refractions. *Interpretation* 2018;6(4):SM27–37. <http://dx.doi.org/10.1190/INT-2017-0229.1>.
- [8] Christidis K, Gunarathe G. Temperature compensation for ultrasound measurements and characterization of materials. *IEEE Trans Instrum Meas* 2003;52(5):1520–7. <http://dx.doi.org/10.1109/TIM.2003.817153>.
- [9] Yao G, da Silva NV, Warner M, Wu D, Yang C. Tackling cycle skipping in full-waveform inversion with intermediate data. *Geophysics* 2019;84(3):R411–27. <http://dx.doi.org/10.1190/geo2018-0096.1>.
- [10] Sohn H, Lee SJ. Lamb wave tuning curve calibration for surface-bonded piezoelectric transducers. *Smart Mater Struct* 2009;19(1):015007. <http://dx.doi.org/10.1088/0964-1726/19/1/015007>.
- [11] Honarvar F, Sheikhzadeh H, Moles M, Sinclair AN. Improving the time-resolution and signal-to-noise ratio of ultrasonic NDE signals. *Ultrasonics* 2004;41(9):755–63. <http://dx.doi.org/10.1016/j.ultras.2003.09.004>, URL <https://www.sciencedirect.com/science/article/pii/S0041624X03001860>.
- [12] Anderson BE, Douma J, Ulrich TJ, Snieder R. Improving spatio-temporal focusing and source reconstruction through deconvolution. *Wave Motion* 2015;52:151–9. <http://dx.doi.org/10.1016/j.wavemoti.2014.10.001>, URL <https://www.sciencedirect.com/science/article/pii/S016521251400136X>.
- [13] Kober J, Prevorovsky Z, Chlada M. In situ calibration of acoustic emission transducers by time reversal method. *Sensors Actuators A* 2016;240:50–6. <http://dx.doi.org/10.1016/j.sna.2016.01.033>, URL <https://www.sciencedirect.com/science/article/pii/S0924424716300334>.
- [14] Hill R, Adams NL. Reinterpretation of the reciprocity theorem for the calibration of acoustic emission transducers operating on a solid. *Acta Acust United Acust* 1979;43(5):305–12.
- [15] Volker A, Van der Heiden M. Controlled excitation of ultrasonic transducers. e-J Nondestruct Test 2008;13(11). URL <https://www.ndt.net/search/docs.php?id=6427&msgid=0&rootID=0>.
- [16] Govindan V, Jayaprakash J, Park C, Lee JR, Cangul IN. Optimization-based design and control of dynamic systems. *Babylon J Math* 2023;2023:30–5. <http://dx.doi.org/10.58496/bjm/2023/006>.
- [17] Capineri L, Bulletti A. Ultrasonic guided-waves sensors and integrated structural health monitoring systems for impact detection and localization: A review. *Sensors* 2021;21(9):2929. <http://dx.doi.org/10.3390/s21092929>, URL <https://www.mdpi.com/1424-8220/21/9/2929>.
- [18] Farrar CR. In: Worden K, editor. *Structural health monitoring: A Machine Learning Perspective*. Online-Ausg. Chichester, West Sussex, U.K: Wiley; 2013. Includes bibliographical references and index. - Electronic reproduction; Palo Alto, Calif; ebrary; 2013; Available via World Wide Web; Access may be limited to ebrary affiliated libraries.
- [19] Mardanshahi A, Nasir V, Kazemirad S, Shokrieh MM. Detection and classification of matrix cracking in laminated composites using guided wave propagation and artificial neural networks. *Compos Struct* 2020;246:112403. <http://dx.doi.org/10.1016/j.compstruct.2020.112403>, URL <https://www.sciencedirect.com/science/article/pii/S0263822319345684>.
- [20] Haywood-Alexander M, Dervilis N, Worden K, Cross EJ, Mills RS, Rogers TJ. Structured machine learning tools for modelling characteristics of guided waves. *Mech Syst Signal Process* 2021;156:107628. <http://dx.doi.org/10.1016/j.ymssp.2021.107628>, URL <https://www.sciencedirect.com/science/article/pii/S0888327021000236>.
- [21] Abbassi A, Römngens N, Tritschel FF, Penner N, Rolfes R. Evaluation of machine learning techniques for structural health monitoring using ultrasonic guided waves under varying temperature conditions. *Struct Health Monit* 2023;22(2):1308–25. <http://dx.doi.org/10.1177/14759217221107566>.
- [22] Rivera J, Carrillo M, Chacón M, Herrera G, Bojorquez G. Self-calibration and optimal response in intelligent sensors design based on artificial neural networks. *Sensors* 2007;7(8):1509–29. <http://dx.doi.org/10.3390/s7081509>, URL <https://www.mdpi.com/1424-8220/7/8/1509>.
- [23] Druet T, Tastet J-L, Chapuis B, Moulin E. Autocalibration method for guided wave tomography with undersampled data. *Wave Motion* 2019;89:265–83. <http://dx.doi.org/10.1016/j.wavemoti.2019.04.002>, URL <https://www.sciencedirect.com/science/article/pii/S0165212518301781>.
- [24] Wang Z, Singh SC, Noble M. True-amplitude versus trace-normalized full waveform inversion. *Geophys J Int* 2020;220(2):1421–35. <http://dx.doi.org/10.1093/gji/ggz532>.
- [25] Jo C-H, Shin C, Suh JH. An optimal 9-point, finite-difference, frequency-space, 2-D scalar wave extrapolator. *Geophysics* 1996;61(2):529–37. <http://dx.doi.org/10.1190/1.1443979>.
- [26] Pratt RG, Worthington MH. Inverse theory applied to multi-source cross-hole tomography. *Geophys Prospect* 1990;38(3):287–310. <http://dx.doi.org/10.1111/j.1365-2478.1990.tb01846.x>, URL <https://onlinelibrary.wiley.com/doi/abs/10.1111/j.1365-2478.1990.tb01846.x>.
- [27] Métrivier L, Brossier R. The SEISCOPE optimization toolbox: A large-scale nonlinear optimization library based on reverse communication. *Geophysics* 2016;81(2):F1–F15. <http://dx.doi.org/10.1190/geo2015-0031.1>.
- [28] Rasgado-Moreno C-O, Rist M, Land R, Ratassepp M. Acoustic forward model for guided wave propagation and scattering in a pipe bend. *Sensors* 2022;22(2):486. <http://dx.doi.org/10.3390/s22020486>, URL <https://www.mdpi.com/1424-8220/22/2/486>.
- [29] Creafom. ACADEMIA 50 3D scanner. 2019, URL <https://www.creaform3d.com>. [Accessed 09 April 2024].
- [30] Diligent. Using the oscilloscope - diligent reference. 2019, URL <https://diligent.com/reference/test-and-measurement/guides/waveforms-oscilloscope>. [Accessed 24 April 2024].
- [31] Dong X, Yuan T, Hu M, Shekhani H, Maida Y, Tou T, et al. Driving frequency optimization of a piezoelectric transducer and the power supply development. *Rev Sci Instrum* 2016;87(10). <http://dx.doi.org/10.1063/1.4963920>.
- [32] Michaels JE, Lee SJ, Croxford AJ, Wilcox PD. Chirp excitation of ultrasonic guided waves. *Ultrasonics* 2013;53(1):265–70. <http://dx.doi.org/10.1016/j.ultras.2012.06.010>, URL <https://www.sciencedirect.com/science/article/pii/S0041624X12001333>.
- [33] Huthwaite P, Seher M. Robust helical path separation for thickness mapping of pipes by guided wave tomography. *IEEE Trans Ultrason Ferroelectr Freq Control* 2015;62(5):927–38. <http://dx.doi.org/10.1109/tuffc.2014.0066884>.
- [34] Operto S, Virieux J, Ribodetti A, Anderson JE. Finite-difference frequency-domain modeling of viscoacoustic wave propagation in 2D tilted transversely isotropic (TTI) media. *Geophysics* 2009;74(5):175–95. <http://dx.doi.org/10.1190/1.3157243>.
- [35] Huthwaite P. Evaluation of inversion approaches for guided wave thickness mapping. *Proc R Soc A: Math Phys Eng Sci* 2014;470(2166):20140063. <http://dx.doi.org/10.1098/rspa.2014.0063>, URL <https://royalsocietypublishing.org/doi/10.1098/rspa.2014.0063>.
- [36] Brenders AJ, Pratt RG. Full waveform tomography for lithospheric imaging: results from a blind test in a realistic crustal model. *Geophys J Int* 2007;168(1):133–51. <http://dx.doi.org/10.1111/j.1365-246X.2006.03156.x>.
- [37] Jørgensen M, Halkjelsvik T, Liestøl K. When should we (not) use the mean magnitude of relative error (MMRE) as an error measure in software development effort estimation? *Inf Softw Technol* 2022;143:106784. <http://dx.doi.org/10.1016/j.infsof.2021.106784>, URL <https://www.sciencedirect.com/science/article/pii/S0950584921002263>.
- [38] Lyu C, Capdeville Y, Al-Attar D, Zhao L. Intrinsic non-uniqueness of the acoustic full waveform inverse problem. *Geophys J Int* 2021;226(2):795–802. <http://dx.doi.org/10.1093/gji/ggab134>.
- [39] Hassefras E, Volker A, Verweij M. Efficient guided wave modelling for tomographic corrosion mapping via one-way wavenfield extrapolation. *Sensors* 2024;24(12):3750. <http://dx.doi.org/10.3390/s24123750>, URL <https://www.mdpi.com/1424-8220/24/12/3750>.

Curriculum Vitae

Carlos-Omar Rasgado-Moreno ✉ corasgado@gmail.com 📞 +49 176 72583027

- UT Level 1 inspector and author of 4+ scientific publications in the fields of NDT and SHM.
- Strong background in signal processing and ultrasonic imaging.
- Passionate for **Project management**.

Education

PhD in Civil Engineering Tallinn University of Technology, Estonia.	2020 - 2025
MSc(R): Mechanical Engineering Durham University, United Kingdom.	2018 - 2020
BsC (Hons): Mechanical Engineering University of Veracruz, Mexico.	2013 - 2017

Work Experience

NDT Engineer October 2024 - Present
Testia GmbH

Experienced in ultrasonic inspection and automation projects for composite structures.
Developed UT inspection automation for delamination and porosity detection on flaps using NDTkit.

Skilled in writing technical documentation for Testia and customers in compliance with AIRBUS qualification processes.

Collaborated in multidisciplinary teams for NDT inspection process based on phase arrays, X-Rays and UT techniques.

Early Stage Researcher September 2020 - August 2024
Tallinn University of Technology

Experienced in developing guided wave tomography for pipelines and composite materials, with expertise in modeling ultrasonic wave propagation using Abaqus, Matlab and CIVA.

Optimized ultrasonic inspection reliability by 15% through root cause analysis and hardware debugging.

Provided technical support to entry-level members and developed a data collection pipeline for pipe inspections.

Skilled in mathematical modeling and collaboration with engineers to enhance signal acquisition instrumentation.

Skills and Interests

Coding	Matlab, Python, Fortran 90, C, R-studio, Shell-scripting.
Interests	Research and development, Acoustics, SHM, Ultrasound, Guided Waves.
Software	CIVA, Abaqus, Ansys, OpenFOAM, SolidWorks, Simulink, Seiscope toolbox.
Platforms	Linux-based systems, Windows, MS Office, HPC.
Skills	Proficiency in maths, thermodynamics, guided waves and signal processing.

Internships and Trainings

- Testia GmbH. Bremen, GER.** April 2025
UT Level 1 inspector training.
- French Alternative Energies and Atomic Energy Commission (CEA). Paris, FR.** October 2023
Internship in calibration methods for Guided Wave Tomography and CIVA software.
- SAFRAN. Paris, FR.** June 2022
Training in characterization of defects in composites.
- Imperial Collage London & Guided Ultrasonics. London, UK.** March 2022
Training in Guided Waves and localization of defects in pipes.
- Netherlands Organization for Applied Scientific Research (TNO). The Hague, NL.** April 2022
Internship in advance numerical methods for Guided Waves and Tomography.
- Shell International B.V. Online.** February 2022
Training in Corrosion Monitoring in Oil & Gas & Energy industry.

Publications

- Rasgado et al. (2022).** Acoustic Forward Model for Guided Wave Propagation and Scattering in a Pipe Bend. *Sensors* 2022, 22(2), 486.
- Rasgado and Ratassepp (2023a).** Geodesic Equations For Guided Wave Helical Path Separation for a Pipe Bend. *Mechanical Systems and Signal Processing*. Volume 204.
- Rasgado and Ratassepp (2023b).** Quantitative Imaging of Elongated Thickness Defects in Pipelines Using Ultrasonic Guided Wave Tomography. *ASME 2023 International Mechanical Engineering Congress and Exposition*. Volume 1: Acoustics, Vibration, and Phononics.
- lablonskyi et al. (2023).** Unsupervised Fouling Reconstruction in the Pipe Bend. *2023 IEEE International Ultrasonics Symposium (IUS)*.
- Rasgado et al. (2025a).** Optimising Full Waveform Inversion With Inhomogeneous Transducers: Parameters and Considerations for Successful Implementation. *NDT and E International*, 2025.
- Rasgado et al. (2025a).** Guided Wave Tomography Based on Full Waveform Inversion for Pipe Bends. *Ultrasonics*.

Awards and Funding

- First place in the bachelor's admission exam. 2013
- Outstanding student award. 2017
- MSc funded by The Mexican Council of Science and Technology (CONACyT) and the Mexican Council of Energy (SENER). 2018 - 2019
- PhD funded by The European Union's Horizon 2020 and the Estonian Research Council, grant PRG737. 2020 - 2024

Languages

- Spanish** Native.
- English** Fluent.
- French** Conversational.
- Estonian** Conversational.
- German** Basic.

Elulookirjeldus

Carlos-Omar Rasgado-Moreno ✉ corasgado@gmail.com 📞 +49 176 72583027

- UT 1. taseme inspektor ja üle 4 teadusliku publikatsiooni autor NDT ja SHM valdkondades.
- Tugev taust signaalitöötlemises ja ultraheli kujutamises.
- Kirglik **projektijuhtimise** vastu.

Haridus

Doktorikraad ehitustehnikas Tallinna Tehnikaülikool, Eesti.	2020 - 2025
Magistrikraad (MSc): Mehaanikatehnika Durhami Ülikool, Ühendkuningriik.	2018 - 2020
Bakalaureusekraad (Hons): Mehaanikatehnika Veracruz'i Ülikool, Mehhiko.	2013 - 2017

Töökogemus

NDT insener Oktoober 2024 - Praegu
Testia GmbH

Kogenud ultraheli kontrollimises ja komposiitstruktuuride automatiseerimisprojektides.
Arendanud UT kontrolli automatiseerimist delaminatsiooni ja poorsuse tuvastamiseks klapidel, kasutades NDTkit-i.

Oskuslik tehnilise dokumentatsiooni kirjutamises Testiale ja klientidele vastavalt AIRBUSi kvalifikatsiooniprotsessidele.

Teinud koostööd multidistsiplinaarsetes meeskondades NDT kontrolliprotsesside jaoks, mis põhinevad faasimassiividel, röntgenikiirgusel ja UT tehnikatel.

Algtaseme teadur September 2020 - August 2024
Tallinna Tehnikaülikool

Kogenud juhitava lainetomograafia arendamises torustike ja komposiitmaterjalide jaoks, oskustega ultrahelilainete leviku modelleerimisel Abaquse, Matlabi ja CIVA abil.

Optimeerinud ultraheli kontrolli usaldusväärsust 15% võrra juurpõhjuste analüüsi ja riistvara silumise kaudu.

Pakkunud tehnilist tuge algtaseme liikmetele ja arendanud torukontrollide jaoks andmekogumise torujuhtme.

Oskuslik matemaatilises modelleerimises ja koostöös inseneridega signaalikogumise instrumentide täiustamiseks.

Oskused ja huvid

Programmeerimine	Matlab, Python, Fortran 90, C, R-studio, Shell-skriptimine.
Huvid	Teadus- ja arendustegevus, akustika, SHM, ultraheli, juhivad lained.
Tarkvara	CIVA, Abaqus, Ansys, OpenFOAM, SolidWorks, Simulink, Seiscope tööriistakast.
Platvormid	Linux-põhised süsteemid, Windows, MS Office, HPC.
Oskused	Matemaatika, termodünaamika, juhivate lainete ja signaalitöötlemise oskus.

Praktikad ja koolitused

- Testia GmbH. Bremen, SAKSAMAA.** Aprill 2025
UT 1. taseme inspektori koolitus.
- Prantsuse Alternatiivsete Energiate ja Aatomienergia Komisjon (CEA). Pariis, PRANTSUS-MAA.** Oktoober 2023
Praktika juhitava lainetomograafia kalibreerimismeetodites ja CIVA tarkvaras.
- SAFRAN. Pariis, PRANTSUSMAA.** Juuni 2022
Koolitus komposiitmaterjalide defektide iseloomustamises.
- Imperial College London & Guided Ultrasonics. London, ÜHENDKUNINGRIIK.** Märts 2022
Koolitus juhivate lainete ja torude defektide lokaliseerimise kohta.
- Hollandi Rakendusteadusliku Uurimise Organisatsioon (TNO). Haag, HOLLAND.** Aprill 2022
Praktika edasijõudnud arvutusmeetodites juhivate lainete ja tomograafia jaoks.
- Shell International B.V. Veebis.** Veebruar 2022
Koolitus korrosiooni jälgimises nafta-, gaasi- ja energiasektoris.

Publikatsioonid

- Rasgado et al. (2022).** Acoustic Forward Model for Guided Wave Propagation and Scattering in a Pipe Bend. *Sensors* 2022, 22(2), 486.
- Rasgado and Ratassepp (2023a).** Geodesic Equations For Guided Wave Helical Path Separation for a Pipe Bend. *Mechanical Systems and Signal Processing*. Volume 204.
- Rasgado and Ratassepp (2023b).** Quantitative Imaging of Elongated Thickness Defects in Pipelines Using Ultrasonic Guided Wave Tomography. *ASME 2023 International Mechanical Engineering Congress and Exposition*. Volume 1: Acoustics, Vibration, and Phononics.
- lablonskyi et al. (2023).** Unsupervised Fouling Reconstruction in the Pipe Bend. *2023 IEEE International Ultrasonics Symposium (IUS)*.
- Rasgado et al. (2025a).** Optimising Full Waveform Inversion With Inhomogeneous Transducers: Parameters and Considerations for Successful Implementation. *NDT and E International*, 2025.
- Rasgado et al. (2025a).** Guided Wave Tomography Based on Full Waveform Inversion for Pipe Bends. *Ultrasonics*.

Auhinnad ja rahastused

- Esimene koht bakalaureuse sisseastumiseksamitel. 2013
- Silmapaistva tudengi auhind. 2017
- Magistr kraad rahastatud Mehhiko Teaduse ja Tehnoloogia Nõukogu (CONACYT) ja Mehhiko Energieanõukogu (SENER) poolt. 2018 - 2019
- Doktorikraad rahastatud Euroopa Liidu Horizon 2020 programmi ja Eesti Teadusagentuuri poolt, grant PRG737. 2020 - 2024

Keeled

- Hispaania** Emakeel.
Inglise Sujuv.
Prantsuse Vestlustase.
Eesti Vestlustase.
Saksa Algeline.

ISSN 2585-6901 (PDF)
ISBN 978-9916-80-272-4 (PDF)